TITLE PAGE

Quantitative and kinetic studies of solid $CaCO_3$, $Ca(OH)_2$ and CaO utilising vibrational spectroscopy

by

MALEBOGO ANDRIES LEGODI

A dissertation submitted in partial fulfillment of the requirements for the degree of

MASTER OF SCIENCE

in the Faculty of Science

UNIVERSITY OF PRETORIA
PRETORIA

Promoter: Prof. D. De Waal
May 2000

University of Pretoria

CONTENTS

ACKNOWLEDGEMENTS

The author wishes to express sincere gratitude to the following persons :

Prof. D. De Waal (promoter) for her assistance, supervision and informed guidance. Thank you, also, for creating such a conducive studying envirnment for me.

Prof. J. H. Potgieter and PPC for initiating the project and also for guidance.

Mrs M. Loubser for her continual assistance with the crushing and grinding processes.

Friends inside and outside the department of chemistry, UP, for their invaluable advises and support.

My family for their encouragement and moral support.

NRF and the University of Pretoria for the financial support.

Almighty GOD for giving me the health, capability and strength to complete the work.

SYNOPSIS

The decomposition of $CaCO_3$ has been studied extensively for many decades. This reaction is the backbone of lime industry. The desired product of the decomposition of $CaCO_3$ is CaO (lime), which is the integral part of many lime products. The decomposition is described by the following reaction :

$$CaCO_3 \rightarrow CaO + CO_2$$

Limestone is a term that includes calcium carbonate with varying amounts of impurities, the most of which are silica and alumina. Therefore, the analysis of the decomposition of $CaCO_3$ is the same as that of limestone, since $CaCO_3$ is the major component of limestone.The main objectives of the studies revolved around acquiring qualitative, quantitative, kinetic and mechanistic information.

The most frequently used methods of analysis have always been thermal methods (TG, DTG, DSC, etc). Due to many possible experimental conditions, reaction-influencing factors and the property of the product (lime), varying conclusions on mechanistic and kinetic properties of the decomposition of $CaCO_3$ have been drawn.

However, thermal methods are time consuming and use extremely small mass of samples. Other methods of analysis which gave excellent results (in agreement with thermal methods) were photoacoustic spectroscopy and loss-on-ignition. These methods are also prone to errors and could be umbiguous.

In the present work, Fourier-Transform infrared spectroscopy was investigated for possible application to the quantitative study of this reaction. This was done on the mixtures of $CaCO_3$ and $Ca(OH)_2$ containing 100, 85, 70, 50, 30, 15 and 0% of each component on the Brucker 113v spectrometer. A calibration curve of regression coefficient of 0.9950 was obtained.

Following these good results, the FT-IR was then applied to the decomposition of natural limestone to obtain the kinetic information of the reaction. Four different industrial sample sizes of limestone were decomposed isothermally at 900, 950 and 1000° C. The results showed that the isothermal decomposition of limestone in air atmosphere can best be described by Contracting Volume or Ginstling-Brounshtein model. The kinetic parameter values fall within the range specified in the literature (as obtained using thermal methods).

Furthermore, the quantitative FT-IR method was investigated for possible application to the determinations of the content of limestone used as an admixture to the cement blends. FT-IR quantitative analysis was performed on the cement blend samples containing gradually increasing amounts of limestone. Again, a good calibration curve with average regression coefficient of 0.9970 was obtained. A complementary study involving the weighing of the same samples before and after decomposition (for a set time at 1000° C) gave comparably good results (averaged regression coefficient of 0.9950).

OPSOMMING

Die ontbinding van $CaCO_3$ is al vir baie dekades breedvoerig bestudeer. Hierdie reaksie is die basis van die kalknywerheid. Die gewensde produk van die ontbinding van $CaCO_3$ is CaO (kalk), ‘n integral deel van baie kalkprodukte. Die ontbinding word deur die volgende vergelyking beskryf:

$$CaCO_3 \rightarrow CaO + CO_2$$

Kalksteen is ‘n term wat kalsiumkarbonaat met veranderlike hoeveelhede onsuiwerhede, hoofsaaklik silika en alumina, insluit. Gevolglik is die ontleding van die ontbinding van $CaCO_3$ soortgelyk aan die ontbinding van kalksteen, aangesien $CaCO_3$ die hoofkomponent van kalksteen is. Die hoofdoelwitte van die studies is om kwalitatiewe, kwantitatiewe, kinetiese en meganistiese data te bekom.

Termiese metodes (TG, DTG, DSC, ens) is gereeld vir ontledingsdoeleindes gebruik. Weens die wye verskeidenheid eksperimentele toestande, faktore wat reaksie beinvloed en die eienskap van die produk (kalk) is verkeie verskillende gevolgtrekkings aangaande die meganistiese en kinetiese eienskappe van die ontbinding van $CaCO_3$ bereik. Termiese metodes is egter baie tydrowend en baie klein massa monster word gebruik. Ander metodes wat goeie resultate (in ooreenstemming met termiese metodes) gelewer het, is foto-akoestiese spektroskopie en massaverlies bepalings (regressie koeffisiente van naastenby 0.9950). Hierdie metodes is tot foute geneig en kan dubblesinnig wees.

In die huidige studie is Fourier-Transform-Infrarooispektroskopie as ontledingsmetode, vir die kwantitatiewe studie van hierdie reaksie, ondersoek. Dit is uitgevoer met behulp van die Bruker 113v spektrometer met mengsels van $CaCO_3$ en $Ca(OH)_2$, wat 100, 85, 70, 50, 30, 15 en 0% van elke komponent bevat, gedoen. ‘n Kalibrasiekromme met ‘n regressie koeffisient van 0.9950 is verkry.

Na hierdie goeie resultate verkry is, is die FT-IR gebruik om die ontbinding van natuurlike kalksteen te ondersoek, met die doel om die kinetiese data van die reaksie te verkry. Vier verskillende nywerheidsmonstergroottes (kalksteen) is isotermies teen 900, 950 en 1000° C ontbind. Die resultate toon dat die isotermiese ontbinding van kalksteen in lug atmosfeer die beste deur die Volumekrimping- of Ginstling-Brounshteinmetode beskryf word. Die kinetiese parameterwaardes val binne die gebied wat deur die literatuur (soos deur termiese metodes bepaal) beskryf word.

Verder is die kwantitatiewe FT-IR metode vir moontlike ontleding van die samestelling van kalksteen wat as toevoeging tot sementmengsels gebruik word, getoets. FT-IR kwantitatiewe ontleding is op sementmengsels met toenemende hoeveelhede kalksteen uitgevoer. 'n Goeie kalibrasiekromme met 'n gemiddelde regressie koeffisient van 0.9970 is weereens verkry. 'n Onderteuningstudie wat die weeg van die monsters voor en na die ontbinding (vir 'n vasgesteelde tyd teen 1000° C) behels, het goeie resultate gelewer (gemiddelde regressie koeffisient van 0.9950).

CHAPTER 1

GENERAL INTRODUCTION

The thermal decomposition of $CaCO_3$ (main component of limestone) has been the subject of interest to researchers for many decades. The studies have been carried out under both isothermal and dynamic conditions. Many atmospheric environments have also been used in the investigation, such as CO_2, air, N_2, vacuum, O_2, etc. The factors that affect this decomposition are rate of heating (in dynamic studies), shape of sample container, ambient environment, origin of sample (which characterizes composition), sample size, impurities, etc. One of the most important factors that affect the thermal decomposition considerably is the sample size. The optimization of this factor could be important in site consideration in lime manufacturing and in terms of energy conservation as considerable quantities of material are involved [1].

The product of this decomposition process, lime (CaO), has many applications in building materials such as cement, in agriculture as soil conditioner, in the metallurgical industry, in catalysis [2,3] and in chemical precipitation of impurities in various applications (e.g. water treatment and treatment of process streams in steel manufacturing) [2]. The bulk of the lime produced through thermal decomposition of natural limestone is used in cement production.

The decomposition of limestone to lime is the most energy-demanding reaction in the clinkering process. The kinetics of the decomposition determine not only the retention time of the raw meal in the kiln, but also the extent to which the lime (CaO) reacts with other components like silicates, aluminates and iron oxide in the raw meal. The quality of the clinker formed depends on these factors[4,5].

One of the major problems in kinetic studies is the quantification of the dissociation process:

$$CaCO_3 \rightarrow CaO(s) + CO_2(g)$$

Investigations using thermogravimetry and X-Ray Diffraction (XRD) as quantitative analytical tools were done previously, but in thermogravimetric measurements only very small sample sizes were possible which was difficult to extrapolate to " real process " conditions (in which very large sample sizes are used). In XRD preferred orientation made quantification difficult [6].

Furthermore, rapid and accurate determinations of limestone in lime products would be useful for process control applications in the lime industry. The loss-on-ignition method commonly used for determining residual limestone is time consuming and prone to errors [2].

The use of limestone as an admixture allows an increase in the output of a cement factory at lower production costs. Concrete produced from a cement containing limestone as an admixture has a denser structure and consequently enhanced durability. Therefore, a fast and easy analytical method to control the addition of limestone is required for operational and quality assurance purposes. Common methods, besides the loss-on-ignition, in this case are the classical wet chemical techniques. However, they are also found to be time consuming and ambiguous.

Chapter 2 of this report will investigate the quantitative application of FT-IR spectroscopy to the rapid determination of reagent grade calcium carbonate in $CaCO_3$ / $Ca(OH)_2$ mixtures. In chapter 3, on the basis of the results obtained the investigation will be extended to the decomposition of natural limestone rocks (of industrial sizes and under the lime production conditions). Finally, in chapter 4 the quantitative FT-IR method will be applied to the determination of the content of limestone used as an admixture and that which is found in the lime products.

CHAPTER 2

RAPID DETERMINATION OF LIMESTONE IN $CaCO_3$ / $Ca(OH)_2$ MIXTURES UTILISING FT-IR SPECTROSCOPY.

2.1 INTRODUCTION

The quantitative analysis for samples of different polymorphs of $CaCO_3$ has been performed by means of infrared spectroscopy [7-10], and the infrared spectra of all three phases are well-known [11,12]. The studies of natural samples focussed on the aragonite-calcite ratio. In the investigation of synthetic polymorphs Xyla et al [7] determined aragonite content in aragonite-vaterite and aragonite-calcite mixtures and vaterite content in vaterite-calcite mixtures. For this purpose the ratio of the areas under three different bands, namely, those at 1785, 1080 and 745 cm^{-1} were used relative to the area under 876 cm^{-1} band. The latter band represents the out-of-plane bending mode of CO_3^{2-}, and is present in all three phases of $CaCO_3$. In the infrared quantitative determination of synthetic samples of aragonite in aragonite-calcite mixtures by Hakanen et al [8] the peak height of the aragonite band observed at 852 cm^{-1} was used in relation to that of the calcite band at 874 cm^{-1}. These bands both represent the out-of-plane bending mode of the carbonate ion but differ slightly in wavenumber due to the planar symmetry of the carbonate ion in calcite compared to its non-planarity in aragonite. Due to the partial overlap of these two bands the method was found to be applicable only in the range of 20 to 70% aragonite [2]. Residual limestone in a lime matrix has been examined using photoacoustic spectroscopy for limestone concentrations of between 0.5 and 5% [2].

When limestone is decomposed to lime two side reactions generally occur: $Ca(OH)_2$ is formed in the presence of water vapour and $CaCO_3$ is formed again in the presence of carbon dioxide. It is therefore vital to determine the actual amount of limestone or $CaCO_3$ present at a given time during this reaction, using a fast and accurate technique. Not only will this facilitate quality control of the product as required by the buyer, but it could also be employed as a production control tool to monitor the completeness of the conversion of limestone to lime. In this work the potential of using FT-IR spectroscopy in the determination of $CaCO_3$ in the presence of $Ca(OH)_2$ is demonstrated. It is intended as a preliminary investigation into the role of infrared spectroscopy as far as the quantitative determination of $CaCO_3$ under various industrial conditions is concerned. This latter regard has important implications on the fuel consumption during the production process and thus also its cost efficiency.

2.2 EXPERIMENTAL

KBr discs for the infrared measurements were prepared by pressing pellets containing 100 mg KBr and 1 mg of sample. The samples were made up of mixtures of reagent grade $CaCO_3$ and $Ca(OH)_2$, containing 0, 15, 30, 50, 70, 85 and 100% $CaCO_3$, respectively.

Infrared spectra were recorded as transmission spectra using a Bruker 113v FT-IR spectrometer with a resolution of 3 cm^{-1}, 32 scans and a 100 mg KBr disc as reference. The carbonate bands in the infrared were integrated between 2646 - 2423 cm^{-1}, 1833 - 782 cm^{-1} (including some combination bands), 954 - 724 cm^{-1} (CO_3^{2-} out-of-plane-bending-mode) and 930-730 cm^{-1} (CO_3^{2-} out-of-plane-bending-mode, narrower region), respectively, using standard OPUS software.

2.3 RESULTS AND DISCUSSION

Some of the representative infrared spectra in this investigation are shown in Fig. 2.1. From the infrared spectrum of 100% $CaCO_3$ it is evident that the $CaCO_3$ is present in the form of calcite (v_3 is observed at 1430, v_2 at 876, v_4 at 712 cm^{-1}, and from the lack of a sharp band around 1070 - 1080 cm^{-1}, representing the v_1-mode which is infrared inactive due to the crystal symmetry in calcite). Combination bands

are observed at 1799 cm^{-1} (2 v_2), 2510 cm^{-1} ($2v_2 + v_4$) and 2877, 2986 cm^{-1} ($2v_3$). The strong, sharp band which is characteristic of the O-H stretching vibration in $Ca(OH)_2$ occurs at 3643 cm^{-1} in the spectra of samples which contain the hydroxide. The broad band around 1400 - 1500 cm^{-1} as well as a weak band at 876 cm^{-1} in the $Ca(OH)_2$ spectrum is evident of the rapid formation of the carbonate from the hydroxide in the presence of CO_2 in air.

The results of the integration of ir spectra between 2646 - 2423 cm^{-1} (region 1), 1833 - 1782 cm^{-1} (region 2), 954 - 724 cm^{-1} (region 3 a) and 930 - 730 cm^{-1} (region 3 b) are shown in Table 2.1. Initially all the bands observed in the infrared spectrum of $CaCO_3$ were considered for integration to test its suitability for use in quantitative work. The very weak and very broad bands soon proved to be unsuitable for this purpose, and therefore the integration of bands at 2986, 2877 and 1430 cm^{-1} were not considered further. The use of the very narrow medium sized band at 712 cm^{-1} also resulted in very poor correlations and was not used in further calculations. Two integration regions are reported for the band at 876 cm^{-1} as the narrower region of the same sharp band was considered in order to determine if this could result in an improvement of the correlation coefficient. The fraction $CaCO_3$ present was calculated in each case by using the relative intensity to that in the same region of the ir spectrum of the 100% $CaCO_3$ sample. The calculated fractions are summarized in Table 2.2, and plotted with linear regression in Figures 2.2 to 2.5 for the different regions of integration. The calculated results of the linear regression are presented in Table 2.3 where the correlation coefficients for different regions of integration are compared. The integration of region 1 and region 2 for the combination bands ($2v_2 + v_4$ and 2 v_2, respectively) at 2510 cm^{-1}

(together with its shoulder at higher wavenumbers) and 1799 cm^{-1} (which appears as a shoulder on the 1430 cm^{-1} band), resulted in surprisingly good correlation coefficients, viz. 0.99246 and 0.98660. Integration of the CO_3^{2-} out-of-plane-bending-mode at 876 cm^{-1} in the region between 954 and 724 cm^{-1} resulted in a comparable correlation coefficient of 0.98495. A narrower region of the same band between 930 and 730 cm^{-1} resulted in the best correlation coefficient, 0.99500. The integration of this band is recommended in a narrow region for all purposes of quantitatively determining the calcite present in a mixture by FT-IR where no interference occurs in the same region from other species in the mixture. It certainly appears to be ideal for investigating the decomposition of limestone to lime where the formation of $Ca(OH)_2$ as a by-product cannot be excluded, especially if high humidity conditions exist at the plant during the production period.

2.4 CONCLUSION

A preliminary investigation of the quantitative determination of $CaCO_3$ in $CaCO_3$ / $Ca(OH)_2$ mixtures by means of FT-IR spectroscopy indicates that a calibration curve with an adequate correlation coefficient can be obtained by integration of the 876 cm^{-1} band in a narrow region. The results are normalised using 100% $CaCO_3$. Application of this in an industrial environment would require a standard FT-IR spectrometer with mid-infrared capabilities, hydraulic equipment for the purpose of pressing KBr pellets, and spectroscopic grade KBr. This can be of great importance for various industrial applications which require a quick and effective knowledge of the quantity of $CaCO_3$ in mixtures, particularly in the lime and cement industries. The ease and speed with which results can be obtained should make it particularly attractive to industry as both a quality and process control tool.

Table 2.1 Integrated intensities of infrared bands in $CaCO_3$ / $Ca(OH)_2$ mixtures.

% $CaCO_3$	% $Ca(OH)_2$	Region 1 2646-2423 cm^{-1}	Region 2 1833-1782 cm^{-1}	Region 3a 954-724 cm^{-1}	Region 3b 930-730 cm^{-1}
0	100	1.12903	0.10997	3.65792	2.35020
15	85	2.41215	0.56278	5.06943	4.74957
30	70	5.93430	1.15740	10.50700	10.25080
50	50	8.54141	1.42011	14.54340	13.98940
70	30	9.85431	1.77825	20.56000	21.71950
85	15	13.05510	2.52149	27.87080	25.34760
100	0	15.68970	2.55535	34.57570	31.86690

Table 2.2 Fraction $CaCO_3$ calculated from integrated intensities of infrared bands.

	Calculated $X_{carbonate}$			
% $CaCO_3$	Region 1 2646-2423 cm^{-1}	Region 2 1833-1782 cm^{-1}	Region 3a 954-724 cm^{-1}	Region 3b 930-730 cm^{-1}
0	0.07	0.04	0.11	0.07
15	0.15	0.22	0.15	0.15
30	0.38	0.45	0.30	0.32
50	0.54	0.56	0.42	0.44
70	0.63	0.70	0.59	0.68
85	0.83	0.99	0.81	0.80
100	1	1	1	1

Table 2.3 Linear regression results for the different regions of integration, where Y = A + B*X

Region	A	B	Standard deviation	Correlation coefficient
1 (2646-2423 cm^{-1})	0.05792	0.00913	0.04580	0.99246
2 (1833-1782 cm^{-1})	0.08117	0.00969	0.06509	0.98660
3a (954-724 cm^{-1})	0.03801	0.00890	0.06341	0.98495
3b (930-730 cm^{-1})	0.03095	0.00927	0.03770	0.99500

Figure 2.1 The infrared spectra of (from top to bottom) $CaCO_3$ (calcite); 70% $CaCO_3$ and 30% $Ca(OH)_2$; 50% $CaCO_3$ and 50% $Ca(OH)_2$; 30% $CaCO_3$ and 70% $Ca(OH)_2$; $Ca(OH)_2$.

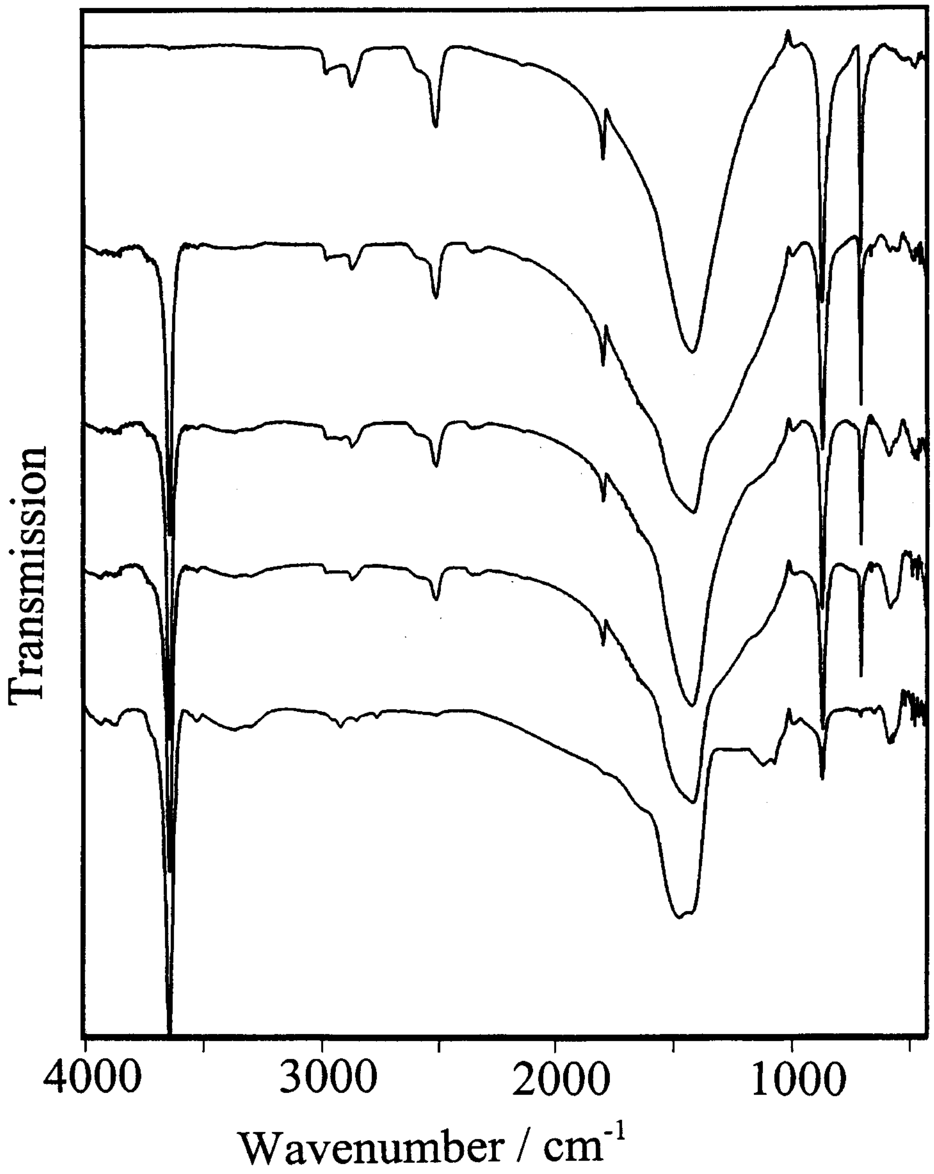

Figure 2.2 The analytical curve for $CaCO_3$ in $CaCO_3$ / $Ca(OH)_2$ mixtures obtained by integration of region 1 (2646-2423 cm^{-1}). The correlation coefficient is 0.99246.

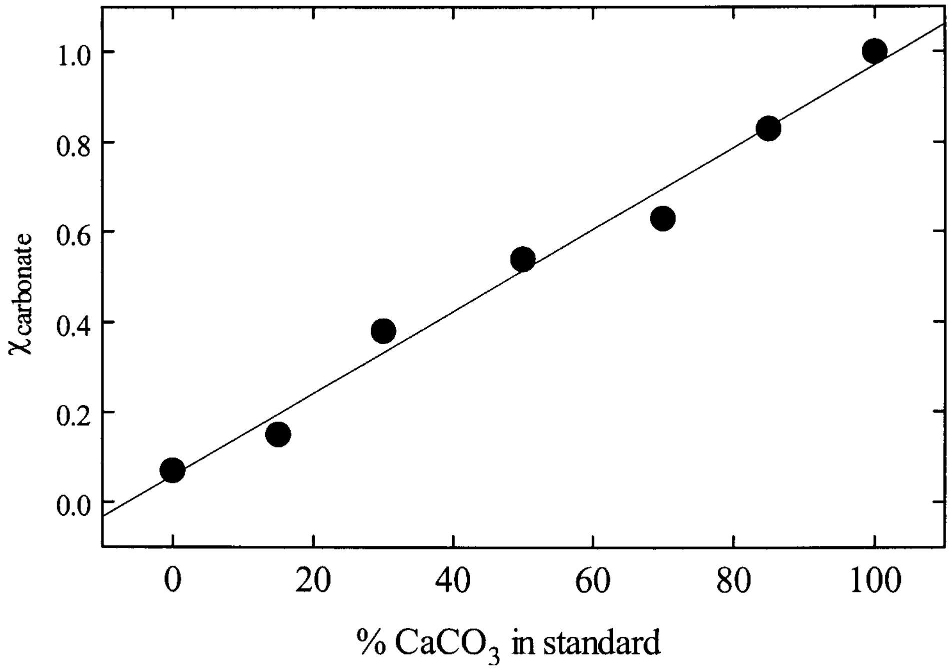

Figure 2.3 The analytical curve for $CaCO_3$ in $CaCO_3$ / $Ca(OH)_2$ mixtures obtained by integration of region 2 (1833-1782 cm^{-1}). The correlation coefficient is 0.9866.

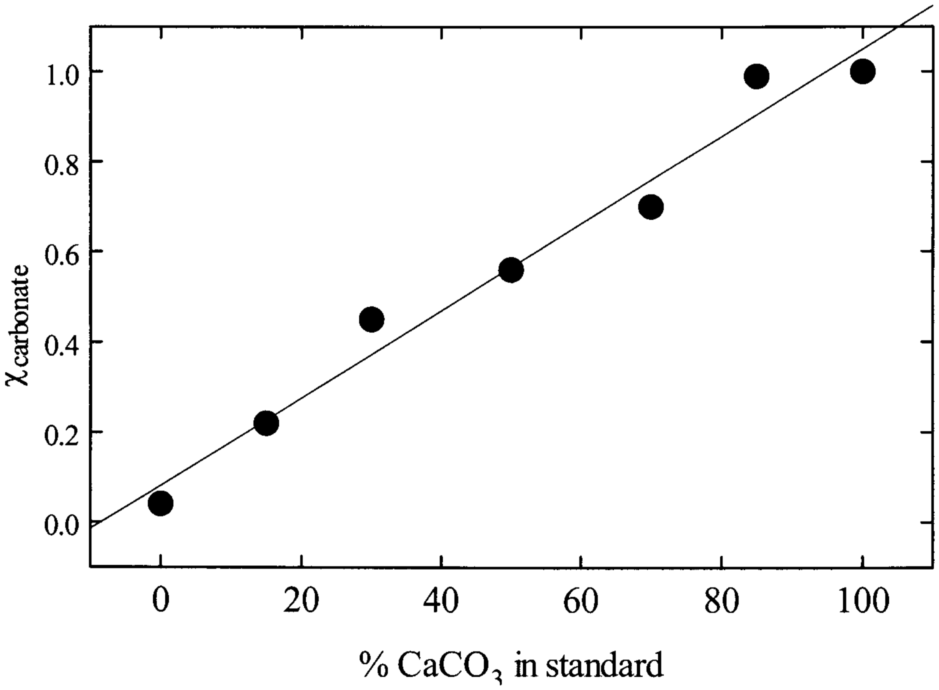

Figure 2.4 The analytical curve for $CaCO_3$ in $CaCO_3$ / $Ca(OH)_2$ mixtures obtained by integration of region 3a (954-724 cm^{-1}). The correlation coefficient is 0.98495.

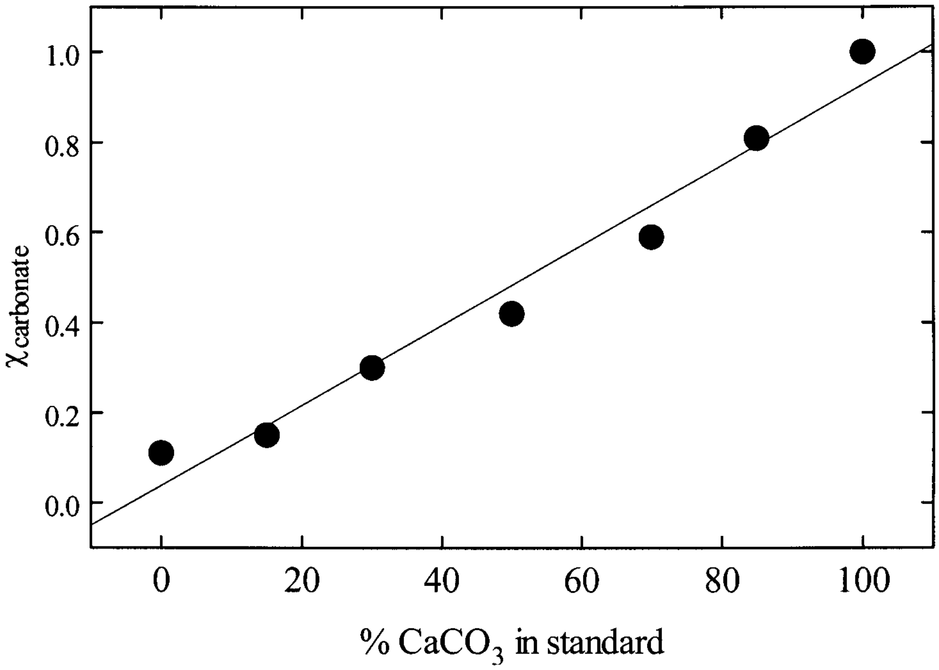

Figure 2.5 The analytical curve for $CaCO_3$ in $CaCO_3$ / $Ca(OH)_2$ mixtures obtained by integration of region 3b (930-730 cm^{-1}). The correlation coefficient is 0.99500.

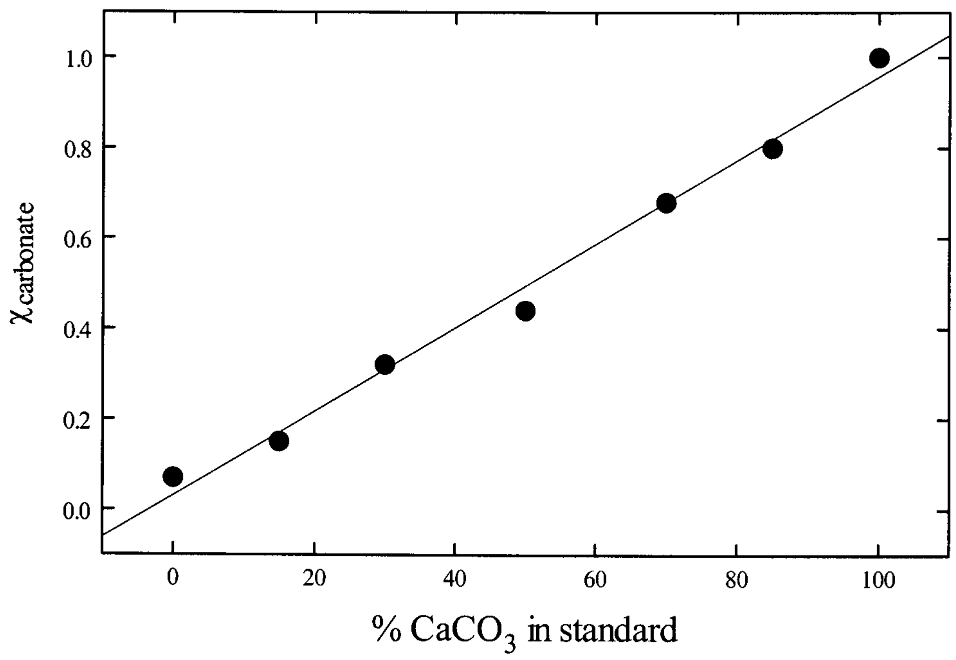

CHAPTER 3

KINETICS OF LIMESTONE DECOMPOSITION

3.1 INTRODUCTION

3.1.1 CHEMICAL PROPERTIES OF LIMESTONE

The limestone under investigation was obtained from one of the PPC quarries at Lime Acres (Northern Cape Province). Limestone is a term that includes calcium carbonate with varying amounts of impurities, the most of which are silica and alumina. The following minerals may occur in limestone: calcite (rhombohedral calcium carbonate); aragonite (orthorhombic calcium carbonate); dolomite (rhombohedral $CaMgCO_3$); vaterite (μ-$CaCO_3$) and magnesite (rhombohedral $MgCO_3$). Vaterite is unstable, converting rapidly to calcite when subjected to temperatures above 65° C [5]. Aragonite is also a metastable phase stabilised either at temperatures higher than 60° C or in the presence of ions such as Mg^{2+} [13]. Aragonite is stable at temperatures as low as 40° C, but does not occur below 40° C. All calcium carbonate polymorphs co-exist at temperatures above 40° C [7].

There are various types of limestone in use of which high-purity limestone and dolomite are the most common. High-purity limestone contains 97 - 99% $CaCO_3$ and dolomite contains 40 - 43% $MgCO_3$ with the $CaCO_3$ component 54 - 58% and 1 - 3% impurities. The additional polymorphic phases are calcium carbonate hexahydrate ($CaCO_3.6H_2O$) and monohydrate ($CaCO_3.\ H_2O$) which have higher solubility than those already mentioned above [14].

The phase transformation of $CaCO_3$ from aragonite to calcite occurs at temperatures around 513 to 616° C [15]. Transformation is irreversible, reconstructive and sluggish. It can also shift the onset of the decomposition temperature to higher values. The evolution of CO_2 in the deep part together with the chemisorbed water might be the reasons for the delay of the decomposition of $CaCO_3$ on the surface to higher temperatures.

3.1.2 THERMAL DECOMPOSITION REACTIONS OF SOLIDS.

Thermal decomposition of solids can be defined as the breakdown of one or more constituents of the reactants into simpler atomic groups upon heating. It involves destruction of the stabilizing forces of the crystal lattice of a solid reactant, leading to chemical reactions and physical reorganizations. A more restricted meaning of the definition [16] has become acceptable and is specifically applied to those processes in which bond redistribution yields a solid residue of a different chemical composition from the reactant. The thermal decomposition of a solid is therefore represented by

$$A(s) \rightarrow B(s) + C(g)$$

where A is the solid reactant and B and C are the products in either a solid state or a gaseous state [16]. Thermal analysis (Thermogravimetry (TG), differential thermal analysis (DTA) and differential scanning calorimetry (DSC)) is the most generally used and convenient technique for the quantitative study of such reactions.

Thermal analysis basically involves the recording of the weight of a substance, in an environment heated or cooled at a controlled rate, as a function of time or temperature [17]. The development and availability of reliable and accurate electronic microbalance in thermogravimetry have led to their wide application in kinetic studies of the decomposition of solids [18].

There are two alternative methods that can be used in kinetic investigation of the thermal decomposition of solids: 1) measurement of the amount of product is made while the reactant is maintained at a known constant temperature (isothermal decomposition) [19] and 2) measurements made while the sample is subjected to a controlled rising temperature (non-isothermal decomposition or dynamic method)[20]. The two methods have been widely exploited in the determination of the thermal stability and kinetic characteristics of substances. An isothermal analysis can complement an analysis using a TG diagram [21].

Factors that may influence the measurements by TG are heating rate, sample mass, pre-treatment of the sample, type of atmosphere used in the thermogravimetric analyser (e.g. N_2, Ar) and the flow rate of the gases employed in a dynamic atmosphere. The thermal decomposition of a solid is sometimes associated with physical transformations, such as melting, sublimation and recrystallization. Recrystallization of a solid may result in the production of higher temperature lattice modification, which permits increased freedom of motion of one or more lattice constituents. It may also result in the elimination of regions of local lattice distortion, e.g. dislocations, grain boundaries, etc, without change in chemical composition or, indeed, lattice configuration [22].

The chemical properties and reactivity of solids are strongly influenced by the relative immobility of the constituent ions or molecules in the lattice of the reactant phase. The reactivity of the identical chemical groups in a solid reactant may vary with their position in the solid, as the structure may contain imperfections. In regions of local distortion, the forces of the lattice stabilization may be relatively diminished with a consequent increase in the probability of reaction. This contrasts with the homogeneous behaviour of similar groups in the liquid or gaseous phase. In rate processes of solids it is often observed that there are localized regions or sites of preferred onset of reaction. Similar initiation usually occurs at a surface, leading to the development of a zone of preferred chemical transformation, which thereafter progressively advances into adjoining volumes of unreacted material. This restricted zone of the solid is called the reaction interface [16].

The occurrence of reaction is usually regarded as being exclusively restricted to the reactant-product interface, at which local conditions markedly enhance the ease of the chemical transformation. The kinetic characteristics of the overall process are determined by the velocity of the advance of this interface into unchanged reactant and the variation of its effective area with time [16].

The process by which the reaction interface is initially established is nucleation. The interface is established at a limited number of points in the reactant, usually at a surface and possibly at an imperfect ion [23]. The initially generated germ nucleus develops into a growth nucleus, which increases in size through the advance of the reactant-product interface into the bulk of the solid.

There are some general kinetic principles that have been widely used for the interpretation of the kinetic behaviour of the decomposition reactions of solids [16]:

i) The rate of reaction of a solid is proportional to the aggregate effective area of the reactant-product interface.

ii) The rate of interface advance is constant through an isotropic reactant under isothermal conditions.

iii) The temperature dependence of the rate coefficient obeys the Arrhenius equation.

The above principles are applicable only where the reactant undergoes no melting. If no melting occurs, the shape of the fraction decomposed α against time (t) curve for an isothermal reaction can be related to the geometry of formation and advance of the reaction interface [16].

3.1.3 Thermal Decomposition of Limestone.

The major component of natural limestone is $CaCO_3$ and therefore the decomposition of limestone can virtually be viewed as $CaCO_3$ decomposition [2,24,25,26]. The decomposition temperature of calcium carbonate in vacuum is controlled by two major factors, viz. ageing and extent of chemisorbed water [27]. There is a strong evidence that the reaction:

$$CaCO_3 \rightarrow CaO + CO_2$$

occurs. If the product gas removal is not rapid and complete, readsorption of CO_2 on residual oxide may establish dissociation equilibria within the pores and channels of the layer of residual phase. Thus rate of $CaCO_3$ decomposition can be controlled by heat transfer rate or CO_2 removal. Thermal conductivity is also a crucial factor in determining reaction temperature.

For chemisorbed process of $CaCO_3$ relatively high temperatures are needed for desorption. Chemisorption require energy and thus proceed at limited rate which increase with increasing temperature or pressure. Newly exposed surface leads to increase in surface area which in turn leads to increase in possibility of early decomposition of solid material, i.e. decomposition temperature decreases due to removal of water chemisorbed. Ageing and adsorption phenomena are responsible for fluctuations in temperature data [28]. Different experimental conditions e.g. sample weights, particle size, shape of crucibles, ambient atmosphere, etc., shift the onset of temperature of decomposition [29].

CaO is manufactured by heating the limestone at about 1000° C. The petrological characteristics, concentration, nature of impurities and size of the particles of limestone, etc., affect the decomposition rate and calcination temperature of the limestone. Though alkali and alkaline earth carbonates may occur in natural calcium carbonate in very low proportions they affect decomposition considerably. The blending of potassium carbonate or barium carbonate with calcium carbonate to the extent of 1% brings about the decomposition of the $CaCO_3$ decomposed at comparatively lower temperatures. The quantity of $CaCO_3$ decomposed at these lower temperatures is increased and the rate of decomposition becomes faster. The activation energy for the decomposition reaction is reduced indicating that this blending results in a reduced fuel consumption, thereby improving the economics of lime production from limestone.

Large differences in the decomposition rate occurred when $CaCO_3$ was decomposed isothermally at temperatures of 700, 800 and 900° C, largely due to particle size difference [28]. Other decomposition temperatures of $CaCO_3$ observed were 830, 700 to 795 and 600 to 950° C [30].

3.1.4 ANALYSIS OF SOLIDS BY FT-IR SPECTROSCOPY

IR spectroscopy can be employed as a major probe to obtain molecular details pertaining to their structural and mechanistic properties [31]. The vibrational bands correspond to vibrations of atoms in the molecules. A complementary technique to IR spectroscopy is Raman spectroscopy. In most cases corresponding IR and Raman present different frequency values. This behaviour is in agreement with the different phononic origins of the respective components. The magnitude of these differences is usually considered to be a valuable criterion for the evaluation of the strength of the coupling effects in the unit cell [32].

IR spectroscopy is a very convenient method, since compact yet sensitive equipment no longer requires skilled or dedicated operators. It is fast, easy and very specific (since each compound has its characteristic spectrum).

Solid samples are more susceptible to errors because of scattering and solid state anomalies. Determinations are affected by many physical and chemical factors. The physical factors are the effect of particle size, the polymorphism and orientation as well as the difference in refractive indices between the absorbing substance and the dispersion medium. However, the effects of polymorphism and orientation are negligible when infrared spectroscopy is used for analysis of inorganic samples (minerals, soils, rocks, etc.).

The most important single physical factor which influences the intensity of the absorption bands is the particle size of the sample. When the particle size is larger than the wavelength of the incident radiation, the particle will act as mirrors and thus decrease the intensity of the transmitted light. To reduce this loss of light the particle size of the sample has to be reduced to a value smaller than the wavelength of the incident radiation. The most favourable particle distribution is achieved at that grinding time when the IR band absorbances are maximum [33].

To avoid light scattering, the refractive indices of the sample particles and the embedding material have to be matched. Usually this cannot be achieved in practice, but the material should be immersed in a solid material whose refractive index is as close as possible to that for the sample under investigation. Analysis are carried out on pellets or in mulls. The pellets or mulls must be made under exactly the same conditions to avoid intensity change or shifts in band positions, because of solid state anomalies [34,35]. With the pellet technique potassium bromide (KBr) is the most often used embedding material. If carefully prepared good reproducibility can be achieved and then standard pellets can be stored in a dessicator for at least one month without any appreciable change in their characteristics.

3.1.5 Quantitative Analysis by FT-IR Spectroscopy.

For reliable quantitative analysis the following steps need to be examined: weighing, homogenisation, pellet pressing, repeated recording of IR spectrum and baseline measurements. A calibration curve of known composition needs to be constructed and the quantitative analysis of unknown samples made by interpolation. The analyte must be prepared under conditions identical to the calibration standards [36]. The most intense and narrow band which is free of overlapping is often chosen as the analytical peak. The amount of the analyte can be determined either by integration of the analyte peak or the height of it when the baseline has been drawn.

The FT-IR quantitative analysis of calcium carbonate was first carried out to determine content of three polymorphs of calcium carbonate precipitate formed by spontaneous precipitation in calcium carbonate supersaturation solutions by Xyla et al [7]. The samples were poymorphic in nature. Standard curves have been constructed from the spectra of binary mixtures of pure components. Test mixtures made of pure synthetic components gave results in excellent agreement with their true composition. The minimum content of the polymorph detected was 25%.

Hakanen and Koskokallio [8] successfully performed an infrared spectroscopy quantitative analysis on the laboratory synthesized mixtures of aragonite and calcite.

The method appeared to be applicable to a limited range of mixtures containing about 20 to 70% aragonite. The analytical peaks chosen were 852 cm^{-1} for aragonite and 874 cm^{-1} for calcite.

In 1996 Norton and McClelland [2] performed a rapid determination of limestone using photoacoustic spectroscopy using reagent grade samples. An excellent calibration curve with regression coefficient of 0.9970 was obtained for limestone concentrations ranging from 0.5 to 5%.

3.1.6 KINETIC RATE LAWS FOR THE DECOMPOSITION OF SOLIDS.

A general classification of solid state thermal decomposition is:
i) Reactions controlled by growth of nuclei and interference;
ii) Diffusion controlled reactions and
iii) Reactions where complete or partial liquefaction occurs.

The relationship between α (fraction decomposed) and t (time) are derived from the four equations that represent the rate of nucleation. Different postulates are proposed for the rate of growth of the nuclei [37]. These reactions may be subdivided into three groups which depend on the location of the maximum rate of decomposition [$(d\alpha / dt)_{max}$]:

i) α vs t relationships concerned with nuclei growth (obeyed up to $(d\alpha / dt)_{max}$);
ii)α vs t relationships concerned with both nuclei growth and interference (obeyed on both sides of $(d\alpha / dt)_{max}$);
iii)α vs t relationships concerned with nuclei interference or a decreasing reaction interference (obeyed beyond $(d\alpha / dt)_{max}$).

3.1.6.1 Power Laws

They are represented by the general equation:

$$\alpha = kt^{n}$$

and describe reactions up to a point where dα / dt is at a maximum. Mampel calculated a value for n = 4 in the initial period of decomposition in which the possibility of overlapping of the decomposition zones is taken into account [38]. The integer 'n' is defined as n =β + γ, where β is the stage in nucleation, i.e. 2 or 3. According to the dimension in which growth occurs, γ equals 1, 2 or 3.

3.1.6.2 The Exponential Law

$$\alpha = ke^{k't}$$

is obeyed up to $(d\alpha / dt)_{max}$ [39]. The explanation is based on the possibility of branching nuclei with no overlapping. The appearance of fresh nuclei seem unimportant, or can be either (a) a constant rate or (b) exponential. The growth in length of the nuclei is assumed to be at a constant rate.

3.1.6.3 Prout and Tompkins Law

It occurs in two forms [40]:

i) $\log \alpha / (1- \alpha) = kt + C$ and

ii) $\log \alpha / (1 - \alpha) = k\log t + C$

The above equations depicts the decomposition mechanism describing the appearance of branching nuclei with interference between the nuclei during growth. In this mechanism, the formation of nuclei appears to be unimportant, i.e. not rate-determining. If a uniform rate of branching occurs, equation (i) is valid. Equation (ii) is derived for a variation in the rate of branching with time.

3.1.6.4 The Erofeev equation

Erofeev proposed equations describing isothermal solid decomposition with the general form [41] :

$$1-\alpha=e^{-kt^n}$$

It holds over the range α = 0.05 ~ 0.90, with n = 2, it is said to correspond to two-dimensional growth, n = 3 implies three-dimensional growth and n = 4 can be interpreted as a two-stage nucleation. In the case of overlapping of growth nuclei with three-dimensional growth and initial random nucleation, Avrami deduced a similar equation with n = 3 [42].

3.1.6.5 Mampel Intermediate Law

It describes the system where the rate of decomposition is continually decreasing. This approach leads to the formation of an intermediate law (applying over the middle range of α-values) and takes the form:

$$1-(1-\alpha)^{\frac{1}{3}}=\left(\frac{V}{r}\right)t$$

where V / r = (velocity of advance of interference) / (radius of particle).
A more general form of this law is as follows:

$$1-(1-\alpha)^{\frac{1}{3}}=kt+b$$

where k = V / r. This equation, representing the contracting sphere model, is deduced for a process of surface nucleation, growth over the surface and then the advance of the interface towards the centre of supposed spherical particles [42,43]. When applied to two-dimensional growth, i.e. contracting area model the equation becomes [43]

$$1-(1-\alpha)^{\frac{1}{2}}=kt+b$$

3.1.6.6 The First Order Decay Law

$$1-\alpha=e^{-kt}$$

It is the special case of Erofe'ev equation with n = 1 [37]. This equation is valid at the end of the decomposition reaction and at the point $(d\alpha\ /\ dt)_{max}$. This law holds for a decomposition process dealing with relatively small particle [37].

3.1.6.7 Diffusion Controlled Reactions

For this type of reactions a phase boundary is present and the rate of diffusion through the reacting material also influences the overall decomposition rate. The one-dimensional diffusion process or parabolic law is represented by

$$\alpha^2=\left(\frac{k}{x^2}\right)t$$

where 2x is the thickness of the reacting layer. This law is more commonly expressed as [37]

$$\alpha=k_1t^{\frac{1}{2}}$$

The decomposition rate of a two-dimensional diffusion controlled reaction is given by [43,44]

$$(1-\alpha)\ln(1-\alpha)+\alpha=\left(\frac{k}{r^2}\right)t$$

where r represents the radius of the cylinder of reactant material formed as a result of the two-dimensional diffusion process.

3.1.6.8 The Jander equation.

$$[1-(1-\alpha)^{\frac{1}{3}}]^2=(\frac{k}{r^2})t$$

It is a contracting cube equation of a three-dimensional diffusion process and is a representation of the reaction of a particle as a sphere [46]. A more detailed treatment by Ginstling and Brounshtein takes the form [46,47]

$$\left(1-\frac{2}{3}\alpha\right)-(1-\alpha)^{\frac{2}{3}}=\left(\frac{k}{r^2}\right)t$$

3.1.6.9 CLASSICAL REDUCED-TIME PLOT METHOD.

This is a variation of the reduced-time plot method which involves rearranging the above kinetic equations into the form:

$$F(\alpha) = A\, t / t_{0.5}$$

where $F(\alpha)$ is kinetic function [48], A is a constant for a specific kinetic equation, α is the fraction of the product formed and $t_{0.5}$ is the half-life of the analyte. When $F(\alpha)$ is plotted against $(t / t_{0.5})$ the resulting straight line will always have the slope A.

Alternatively, a plot of α against $(t / t_{0.5})$ is made and the curve is then superimposed on the master plot. Therefore, the experimental data is said to follow the equation represented by the graph on the master plot which is closest to the superimposed experimental curve.

Basis for the classical reduced-time plot method is as follows [49]:
a). It involves plotting the experimental data against the master data in such a way as to produce a linear plot.
b). The agreement of the experimental data with the master data can then be readily assessed by deviation from the straight line.

Three broadly equivalent plotting procedures are then possible:

i) The experimental value α_e at which $(t / t_{0.5})_e$ has the same value as that in the master data $(t / t_{0.5})_m$, is plotted against the master value of α (designated α_m). In the case where the experimental data are exactly described by the kinetic expression under consideration, $\alpha_e = \alpha_m$ and the resulting plot will be a straight line through the origin with slope α_e / α_m equal to unity.

ii). Conversely, the experimental value $(t / t_{0.5})_e$ may be plotted against $(t / t_{0.5})_m$ for common values of α_e and α_m. The resulting plot should be again a straight line through the origin with slope $(t / t_{0.5})_e / (t / t_{0.5})_m$ equal to unity for absolute correlation.

iii). The experimental time t_e may be plotted against $(t / t_{0.5})_m$ for common values of α_e and α_m. For complete correlation the plot should be a straight line through the origin with slope equal to $(t / t_{0.5})_e$.

The plotting procedure used in this study is ii), mainly for confirmation of the kinetic model followed by the decomposition as predicted by the solid-state kinetic equations.

Main advantages are as follows:

i) the method applies to the complete range of decomposition $0< \alpha <1$;
ii) absolute correlation with any reaction expression is readily determined
iii) deviations from the master data are assessed by deviations from a theoretical straight line.
iv) distinction between closely similar master data is facilitated, e.g., equations describing diffusion-controlled reactions;
v) the sensitivity of normal kinetic analysis is preserved.

For more details on kinetics of solid state reactions see reference [37].

3.1.7 KINETIC PARAMETERS.

$$k = A e^{\left(\frac{-E}{RT}\right)}$$

By analogy with the application of the Arrhenius equation to homogeneous reactions in the liquid and gas phases, the coefficients A and E are referred to as the reaction frequency factor and the activation energy of a reaction, respectively.

Since there is no discrete activated state in the solid state, activation energy values need to be evaluated critically before conclusions regarding the stability of the solid reactants can be drawn from them [37]. A homogeneously distributed activated state cannot be described in solid state reactions, as the solid state reactions develop through the nucleation effect. The constant interactions through vibrations provide a means of distributing any increasing energy of an atom to its neighbours. The energy in any small region will thus have a narrow distribution. The lack of statistically defined distribution rules out the use of the Arrhenius parameters as in liquid and gaseous phase reactions.

The activation energy value (E) is usually expressed as an energy quantity per mole ($kJmol^{-1}$), since the measured slope of the Arrhenius plot (ln k vs T^{-1}) is divided by the gas constant, R ($R = 8.314\ J\ K^{-1}mol^{-1}$). There is a difficulty in assigning a meaning to the term " mole " in solid state reactions. If, however, $\Delta H = E$ and an independently measured ΔH value is available, and the ΔH value refers to the enthalpy of the reaction for a mole of reactant, then an estimation of the "mole of activated complex " can be made. The Arrhenius plots, however, can be used as indications of the relationship between the rate constants and the temperature value.

For the initial stages of the reaction ($\alpha < 0.1$), the relationship between the rate constants, k, and reaction time, t, can also be given as

$$\frac{d\alpha}{dt} = kt$$

with α the fraction decomposed [16]. Using these k-values at various temperatures and applying them to the Arrhenius equation; an activation energy value for the nucleation process of a reaction can be obtained.

3.1.8 Literature Review on Kinetic parameters

The decomposition of $CaCO_3$ has been studied extensively by means of thermal analysis methods, mostly with the aim of determining the kinetic parameters [49-57]. The produced lime has many applications in building materials such as cement, in agriculture as soil conditioner, in the metallurgical industry and also as a catalyst [3,58]. A wide range of kinetic energy and pre-exponential factor values (ranging from 109 to 1577 kJ/mol, and 10^2 to 10^{69} min^{-1}, respectively [57]) have been obtained by the workers. The variations in kinetic parameters are usually due to the differences in the conditions and environments under which the experiments were performed. The kinetics of the decomposition of $CaCO_3$ has been investigated by means of thermal analysis under N_2 [49], with various partial pressures of CO_2 [52], in vacuum [38], in a steam of oxygen [53], in air atmosphere, etc. and the results varied in each case. However, the range of the values of the kinetic parameters may overlap.

The decomposition of $CaCO_3$ under N_2 atmosphere follows a three-dimensional diffusion process according to Ginstling-Brounshtein (D_4 mechanism) [49,59]. The kinetic parameters were found to be as follows: E = 172.4 kJ/mol and A = 1.97 x 10^4 K^{-1} min^{-1}. For degradation studies carried out in air atmosphere, E-values ranging from 110 - 742 kJ/mol and pre-exponential factor values, A, varying between 1.6 x 10^2 - 3.2 x 10^{33} min^{-1}, were obtained [57]. The reaction order was found to be 0.67, which would indicate that the reaction mechanism followed the R_3 model [53].

When data, obtained under various partial pressure of CO_2 atmosphere, was analysed even greater values were obtained, namely, E = 709 - 1558 kJ/mol, A = 1.6 * 10^{32} - 7.9 * 10^{68} min^{-1} depending on sample size and heating rate [57]. There is a greater rise in partial pressure of CO_2 during the course of the decomposition when sample size and heating rates are increased and this corresponded to the lower apparent enthalpy of activation, ΔH*. The mechanism followed the R_3 kinetic equation. Criado et al. [21] found that the $CaCO_3$ decomposition under a vacuum of 10^{-4} torr followed a contracting volume kinetic equation (R_3).

Gallagher et al. [53] found that under a stream of O_2 using isothermal studies the rate depends on sample size, and on both sample size and heating rate in dynamic studies. The apparent activation energy for 1 mg sample was found to be 208 kJ/mol [53]. The apparent activation energy in air was 711.3 kJ/mol with the reaction order 0.67 which suggests a contracting volume kinetic equation (R_3).

Hills [30] demonstrated that both heat and mass transfer are important by using sample mass of approximately 1.5 g. He also showed that the slow mass transfer step is the removal of CO_2 by diffusion from a spherical $CaCO_3$-CaO interface moving towards the centre of the sphere. Decomposition of $CaCO_3$ can be defined by the following reaction:

$$CaCO_3 \rightarrow CaO + CO_2 \qquad \text{(a)}$$

The desired product, CaO, is hygroscopic and thus very unstable when exposed to the moisture. The following are subsequent reactions in the presence of moisture :

$$CaO + H_2O \rightarrow Ca(OH)_2 \qquad (b)$$

$$Ca(OH)_2 + CO_2 \rightarrow CaCO_3 + H_2O \qquad (c)$$

The rate of the reaction in a chemically inert environment has been shown to be proportional to the thermal conductivity of the atmosphere [52]. Even though the kinetic parameters from TG curves vary widely, all the curves obey the same linear compensation law and all the family of TG curves can be characterised by a single pair of ‘a’ and ‘b’ parameters [60,61]. The history of the sample has been shown to have a definite effect on the computed value of E, even though the magnitude of the effect is very small [62]. The calculation procedure also have a bearing on the great differences in the kinetic parameter values obtained [63].

When the reaction mechanism changes with temperature, the ln.ln method of analysis [37] will indicate either a progressive change in mechanism (the slope of the plot changes gradually) or an instantaneous change (the slope of the plot changes dramatically) [64]. However, the ln.ln method can only be applied in the range $0.15 < \alpha < 0.5$.

A quantitative FT-IR determination of solid $CaCO_3$ in mixtures of reagent grade $CaCO_3$ and $Ca(OH)_2$ has been shown (in chapter 2) to be at least as effective a method of determining the fraction of $CaCO_3$ present as photo-acoustic spectroscopy [2]. On the basis of these findings the study will be extended to the decomposition of natural limestone rocks in a furnace at fixed temperatures between 900 and 1000° C in air similar to the method which is used in the lime industry. The kinetics of this decomposition will be investigated using FT-IR spectroscopy as the fraction $CaCO_3$ remaining in the sample is determined. Application of the work lies in the optimisation of the decomposition process on the basis of sample size (mass).

3.2 EXPERIMENTAL

3.2.1 Sample preparation for decomposition

The starting material used was natural limestone rock obtained from the Pretoria Portland Cement quarries. It is a sample of the rock which is actually used in the lime production process. The four sizes of limestone rock are described by the weight of the individual rocks. The reason for this is that the measurement of diameter of uneven rocks proved to be highly inaccurate. It stands to reason that a higher mass represents a larger rock size. Sample A is the smallest rock size with the weight varying between 3 to 4 g. The other samples are: Sample B (5-6 g), Sample C (30 - 40 g) and Sample D (90 - 110 g).

3.2.2 Decomposition Procedure

Rocks were weighed and then heated in fireclay crucibles at 700° C for 1800s. Then the heat was rapidly increased to the decomposition temperature, T_d (always within 1200s). The starting time, $t = 0$, was noted as soon as the designated temperature was reached. Isothermal kinetic measurements for each sample size were performed at temperatures of 900, 950 and 1000° C. Samples were taken from the crucibles at different time intervals depending on the decomposition temperature as well as sample size.

For T_d = 1000° C limestone rocks of Sample B were removed from the furnace every 60s, while only 15s were required for the smallest size, Sample A. For Sample C the decomposition time intervals were 300s and for Sample D 360s. At 950° C, measurements were taken every 30, 120, 600 and 720s for Samples A, B, C and D, respectively. When temperature of decomposition was decreased to 900° C, all the rocks could not be decomposed to completion. Therefore, readings were made after approximately each 120, 240, 900 and 1200s for Samples A, B, C and D, respectively. The total time in which the sample was exposed to air during the removal from the furnace to the dessicator was approximately 20s.

3.2.3 FT- IR procedure

The samples were allowed to cool at room temperature in a desiccator and quickly ground to a powder. It took approximately 300s to grind the large samples in air and even less time for smaller ones. Mid infrared spectra were recorded as soon as possible. The KBr pellet preparations in air atmosphere lasted for no more than 300s for each sample. The approximate mass of the sample used was 2 mg, the total mass of the KBr pellet being 1 g.

When the spectra were recorded the baseline was drawn. The most intense, narrow and isolated band was chosen as the analytical peak. Therefore, the area under the analytical peak was integrated. The integration value was viewed as a reflection of the amount of analyte in the sample.

The effect of moisture in the atmosphere seemed to be negligible even after 620s in which the samples were exposed to the air before recording the spectra. This was evident when samples showed total decomposition at 1000° C even after a prolonged period of time exposed to air (in the furnace and during sample preparation for FT-IR analysis).

3.2.4 Parameters for Infrared Spectroscopy.

All spectra were recorded on a Bruker 113v Fourier Transform infrared spectrometer. Details of the experimental parameters may be found in Table 3.1. Spectra were recorded at room temperature, about 298 K. The whole instrument was evacuated down to 180 mbar to ensure the absence of any moisture in the beam path.

Table 3.1 : FT-IR spectrometer operational parameter

PARAMETERS	MID-IR (400-4000CM^{-1})
Resolution	2 cm^{-1}
No. Scan	32
Reference	1 g disc KBr
Mirror level	10 cm.min^{-1}
Baseline	64 points

3.2.5 Data Processing of kinetic studies.

The rate equations which have found application in kinetic studies of solid state decomposition reactions are given in Table 3.2 [24].

Table 3.2: The kinetic rate laws for solid state reactions.

F(α)	Equation	Rate law
D_1 (α)	$\alpha^2 = kt$	One-dimensional diffusion
D_2 (α)	$(1 - \alpha)\ln(1 - \alpha) + \alpha = kt$	Two-dimensional diffusion
D_3 (α)	$[1 - (1 - \alpha)^{1/3}]^2 = kt$	Three-dimensional diffusion
D_4 (α)	$[1 - (2\alpha / 3)] - (1 - \alpha)^{2/3} = kt$	Ginstling-Brounshtein
F_1 (α)	$1 - \alpha = \exp(-kt)$	1st order
R_2 (α)	$1 - (1 - \alpha)^{1/2} = kt$	Contracting area
R_3 (α)	$1 - (1 - \alpha)^{1/3} = kt$	Contracting volume
A_2 (α)	$(1 - \alpha)^{1/2} = kt$	Avrami-Erofe'ev with n = 2
A_3 (α)	$(1 - \alpha)^{1/3} = kt$	Avrami-Erofe'ev with n = 3
A_4 (α)	$(1 - \alpha)^{1/4} = kt$	Avrami-Erofe'ev with n = 4

The purpose of the solid state kinetic studies is to obtain information concerning the reaction mechanism, through comparison of a series of measured α-time values and the theoretical functions (Table 3.2). The $F(\alpha)$ equations have been derived from models based on the geometry of interface initiation and advance and or diffusion process occurring in the solid. The problem may be regarded as the identification of the functional relationship between the fraction decomposed (α) and time (t), $F(\alpha) = kt$, where k is the conventional rate coefficient.

The experimental (α, time) values were fitted to these $F(\alpha) = kt$ equations to obtain the equation which provided the most accurate fit to the experimental data. The linearity of the plots of $F(\alpha)$ values against time at a constant temperature was taken as a criterion for identification of the rate equation. A computer programme was used to determine the correlation coefficient and slope of the different $F(\alpha) = kt$ equations for each of the sets of the experimental data.

The classical reduced-time plot methods were used to confirm the appropriate kinetic equations for the experimental data.

3.3 RESULTS AND DISCUSSION.

3.3.1 THERMAL DECOMPOSITION REACTION.

(1) Sample A (3 - 4 g)

At 1000° C the sample decomposed completely within 120s. However, the isothermal decomposition could not reach completion when the temperature was decreased to 950° C and 900° C. The reaction reached its limiting state after 240s at 950° C and 960s at 900° C, because beyond the above-mentioned times the $CaCO_3$ content appeared to be completely random.

FIGURE 3.1: Fraction of limestone remaining at t (s) for Sample A, the 3 - 4 g sample size.

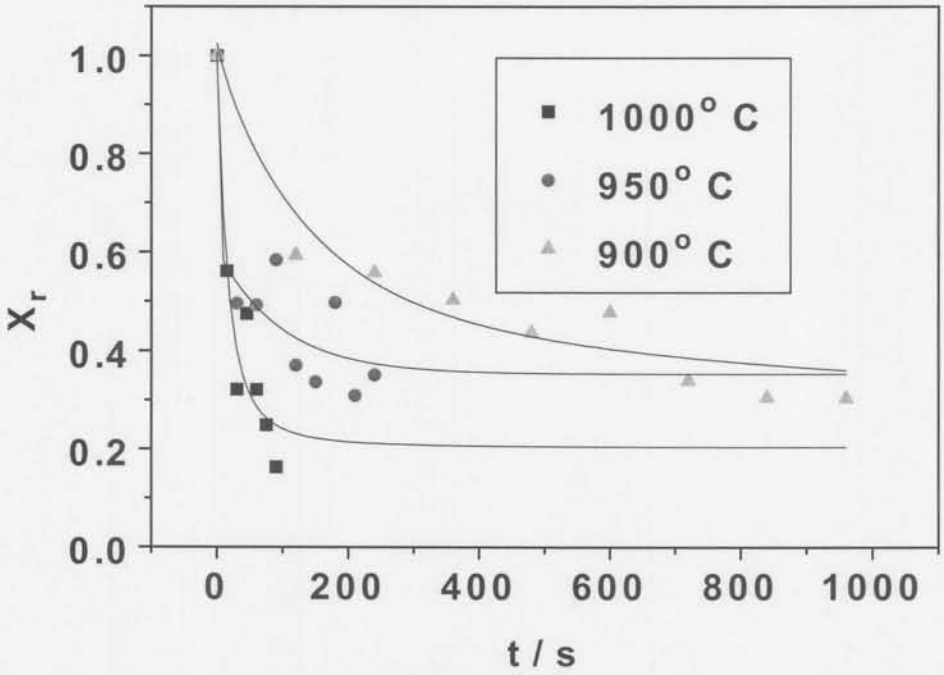

(2) Sample B (5 - 6 g)

The total decomposition at 1000° C took place after 480s. As the decomposition temperature was decreased to 950° C and 900° C, the last measurements were made after 1080s and 1680s respectively.

FIGURE 3.2: Fraction of limestone remaining at t (s) for Sample B , the 5 - 6 g sample size.

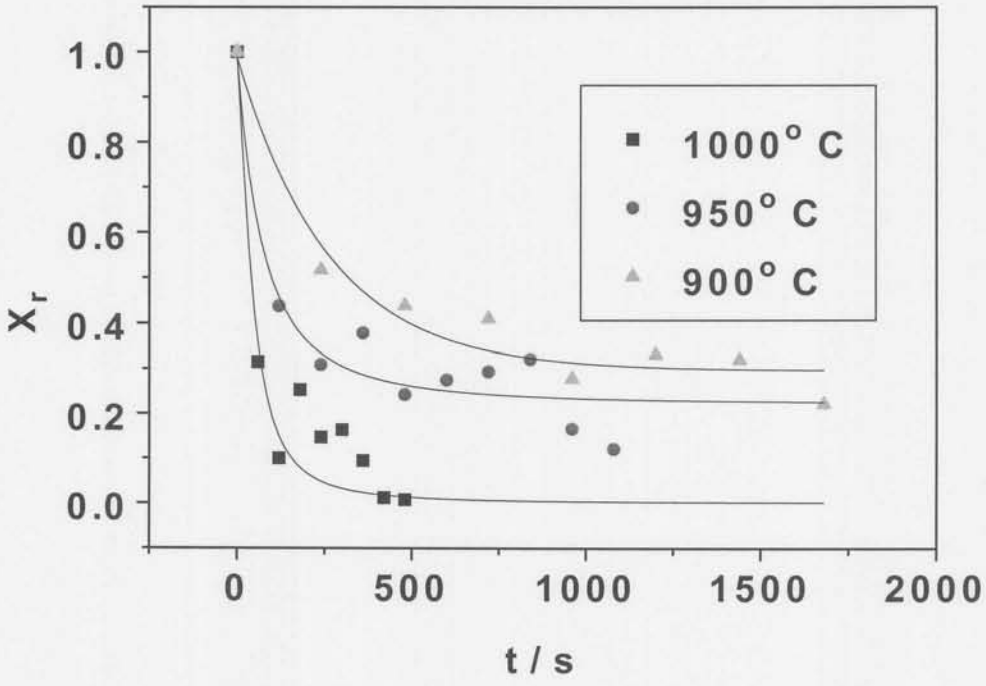

(3) Sample C (30 - 40 g)

The reaction completion was observed after 2400s at 1000° C. The last measurements were made after 5400s and 6300s at 950° C and 900° C, respectively.

FIGURE 3.3: Fraction of limestone remaining at t (s) for Sample C, 30 - 40 g sample size.

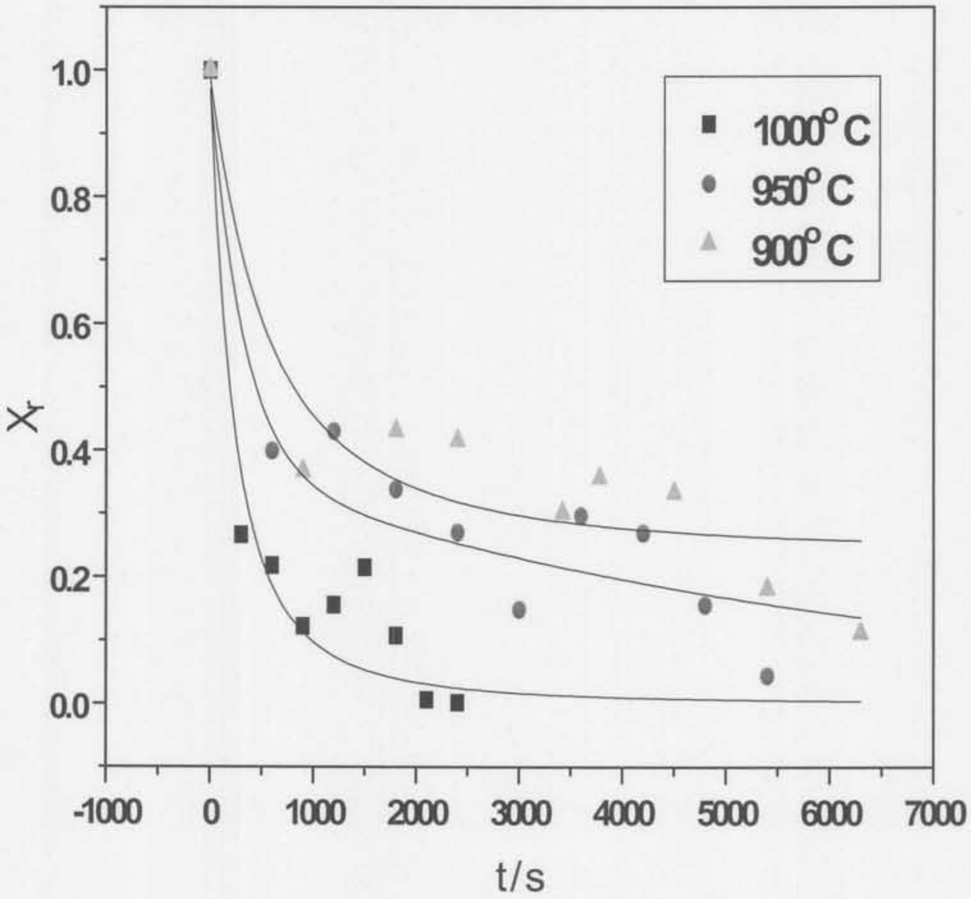

(4) Sample D (90 - 110 g)

At 1000° C the larger rock decomposed completely within 2880s. The final measurements were made after 5400s and 9600s at 950° C and 900° C, respectively.

FIGURE 3.4: Fraction of limestone remaining at t (s) for Sample D, the 90 - 110 g sample size.

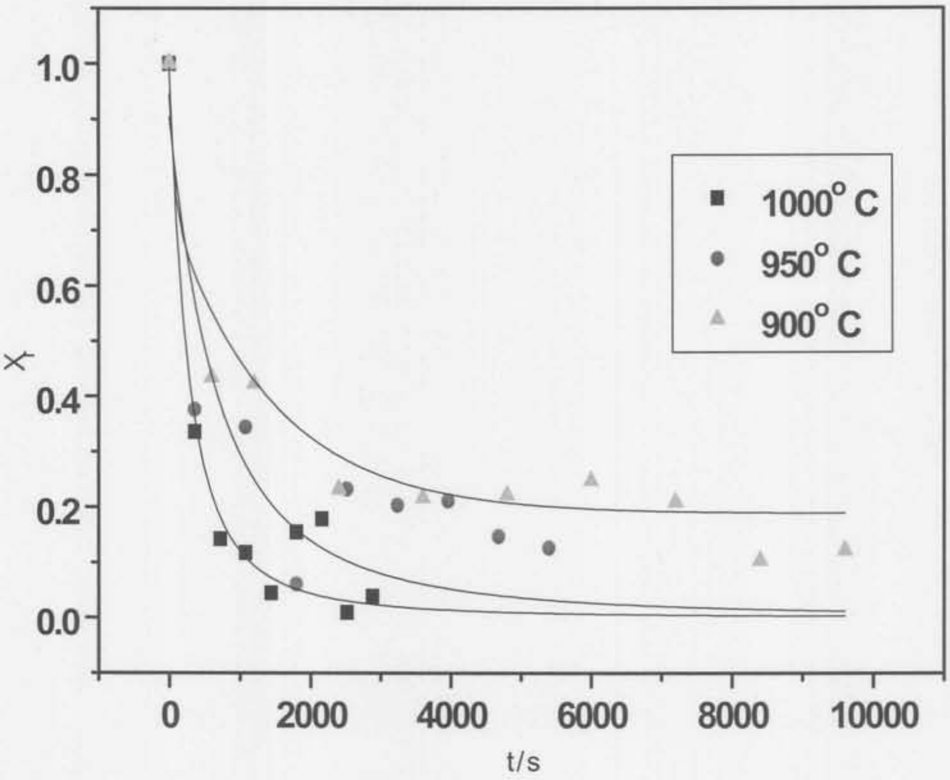

As the temperature decreased, more and more time was required for considerable decomposition to take place on each rock size. One of the rate determining factors in this reaction is the removal of CO_2 from the reaction interface. If the sample remains in the furnace for a prolonged period of time, the product, CaO, accumulation will prevent the escape of CO_2 from the interface.

Figure 3.5 shows the spectrum of the limestone studied. The absence of the fourth peak around 1080 cm^{-1} (symmetric stretching, v_1) clearly indicates that the calcium carbonate in the limestone is in the form of calcite. The typical vibrational modes of $CaCO_3$ (calcite) are observed at 1427.1 cm^{-1} (asymmetric stretching, v_{as}), 875.8 cm^{-1} (out-of-plane bending) and 712.6 cm^{-1} (in-plane bending) [65,66,67]. The band at 875.8 cm^{-1} gradually disappeared during the decomposition as $CaCO_3$ content decreased (Figure 3.6). CaO band is not observed in either Figure 3.5 or 3.6, because it is expected to absorb in the far infrared region only, just below 400 cm^{-1} [15,68].

The IR peak of $CaCO_3$ around 875.8 cm^{-1} was used for integration in order to determine the amount of reactant, $CaCO_3$, remaining in the sample. This peak is strong, narrow and well separated from the others, thus the intensity of this peak in limestone will accurately reflect the amount of carbonate in the decomposition reaction. It has been successfully used before in the quantitative determination of solid $CaCO_3$ in $Ca(OH)_2$ / $CaCO_3$ mixture by FT-IR, also as outlined in chapter 2.

Figire 3.5: The mid-IR spectrum of natural limestone.

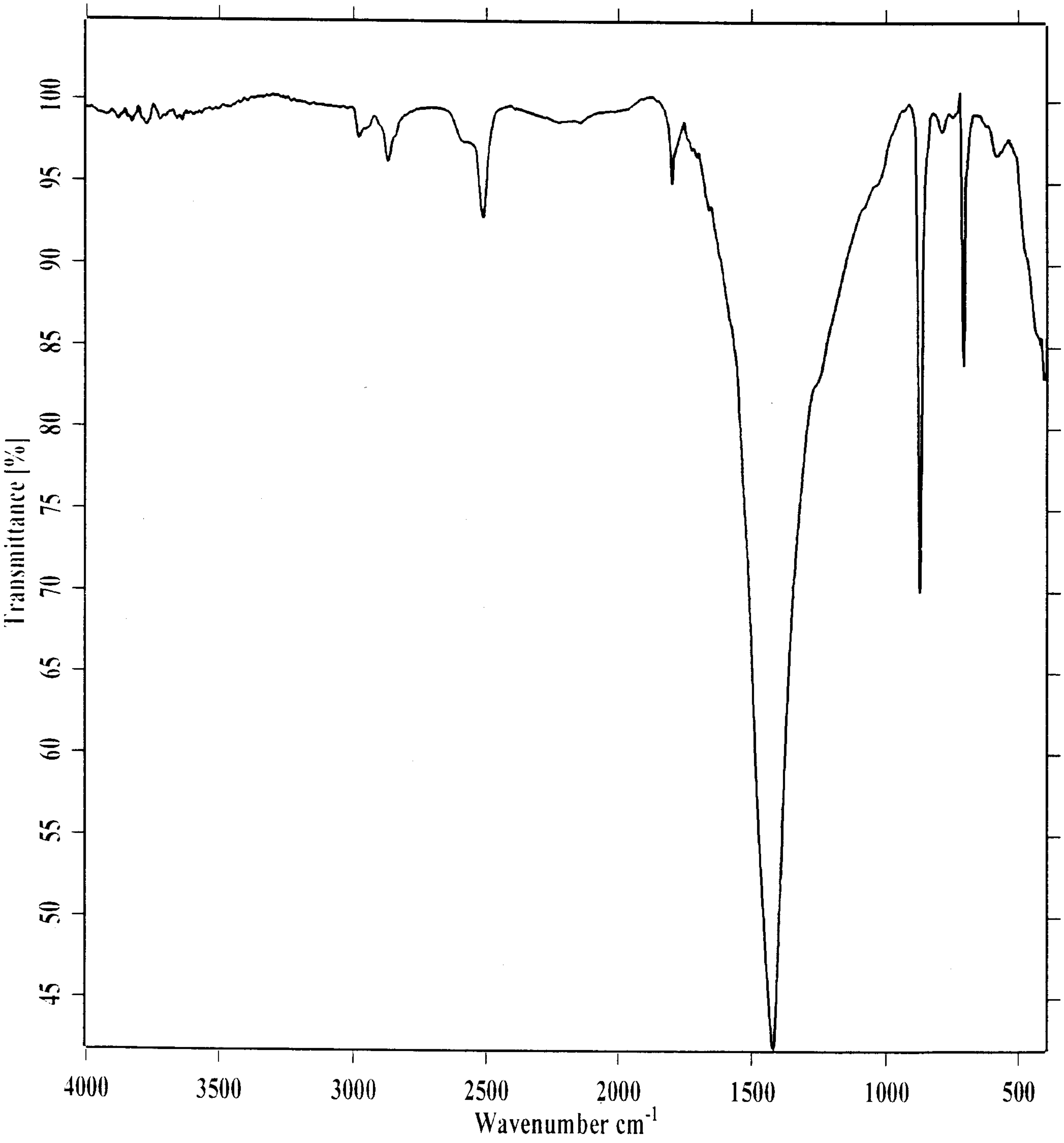

Figure 3.6: The mid-IR spectrum of natural limestone during different stages of decomposition. From top to bottom: Decomposition of Sample C at 1000° C after 45s, 40s, 35s,30s, 25s, 20s, 15s, 10s, 5s and 0s.

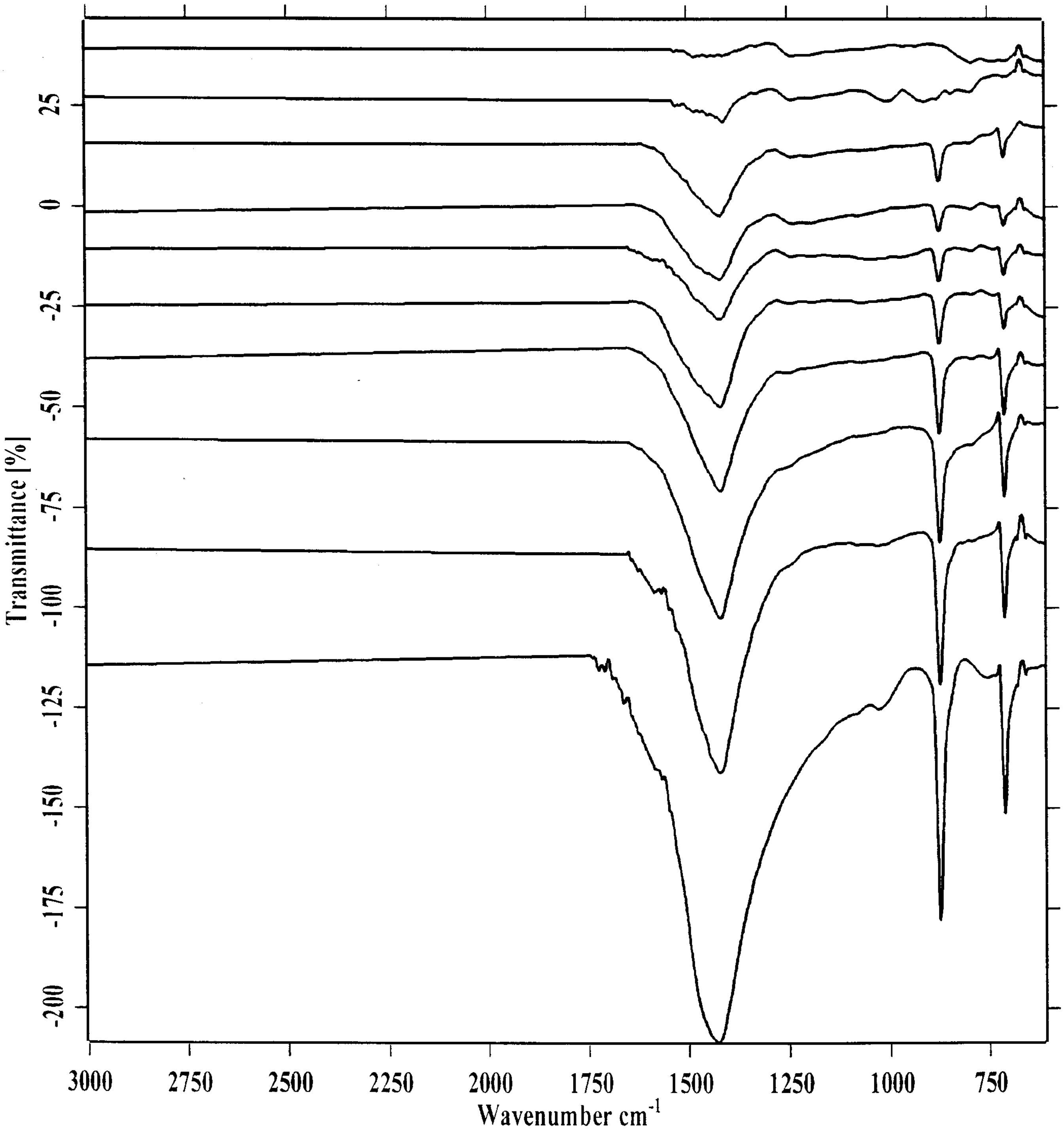

3.3.2 KINETIC STUDIES

The thermal decomposition of limestone or calcium carbonate is an endothermic process [69,70]. In solid endothermic reactions, the energy of activation is normally approximately equal to the overall enthalpy change of the reaction if the reactants and products are both in their standard state [71]. In homogeneous conditions, the order of reaction and the activation energy can be related to collisions between molecules [72].

The "per mole" part of the activation energy in solid state is still questionable. The energy, E, in solid state reaction is defined as the average excess energy a reactant molecule has to possess in order to react [73]. It can be obtained from the vibration of an atom or molecule in the lattice, which could, at a certain temperature, provide sufficient energy at a particular point for the reaction to start. This energy is considered to be related to the rapture of chemical bonds [72].

The Arrhenius parameters, activation energy and the pre-exponential term, on the other hand can be regarded as mathematical parameters describing the reaction and having empirical rather than theoretical significance. The following factors affect the apparent values of E and A: source of sample (e.g. type of limestone), size of sample (e.g. small or relatively large compact samples) and heating characteristics (isothermal or dynamic) [67,69,74,75].

The pre-exponential term in the Arrhenius equation, which is often ignored, can be used to evaluate the validity of a kinetic model for a certain decomposition reaction. Rearranging the Polanyi-Wigner equation into the appropriate form becomes:

$$\mathbf{dn / st_o\ e^{-(E/RT)}}$$

It can be directly applied to the motion of interfaces in solid decompositions [62]. "n / s" is the density per unit area of reactive molecules, d_o the period of one vibration, E the energy of activation and t_o the atomic diameter. The above equation can only be applied to irreversible reactions and it can be considered as a form of the Arrhenius equation with a better description of the pre-exponential or frequency factor.

equation with a better description of the pre-exponential or frequency factor.

The frequency factor is expected to be in the range of 10^{11} to 10^{14} when the entropy of activation is arbitrarily set to zero [71]. It was found however, that where the energy of activation exceeds the enthalpy value, the frequency factor could range from a few to 22 orders of magnitude from the values of 10^{11} to 10^{14} [25].

However, this method requires the product fraction $\alpha < 0.1$. These values are used to calculate the activation energy for the nucleation step and to determine the corrected value of the frequency factor. In this experiment all the initial α values are significantly above 0.1 for all samples at the three temperatures. Furthermore, limestone (or $CaCO_3$) decomposition is a reversible reaction [76,77]. Due to the above two reasons, rearranged Polanyi-Wigner equation (which deals with the values of the frequency factor) could not be used to confirm the kinetic model which describes the decomposition.

In attempting to determine the kinetic expression which will best describe the reaction of limestone, the ln.ln method of analysis was firstly used. The results were, however, inconclusive as the values of the slope obtained for all the sizes at different temperatures did not match any of the models of solid state reactions in the literature. One reason for this could be that the fraction of product was in most cases out of the limit specified in the literature (that is, $0.15 < \alpha < 0.5$) [49].

The experimental results were then fitted to the nine theoretical kinetic equations for solid reactions. The equation with the highest correlation coefficient was chosen to describe the decomposition [21]. Furthermore, the classical reduced time-plot methods were used to confirm the apparent theoretical kinetic equation. The plots were made in linear fashion, with the highest correlation coefficient representing the best fit.

3.3.2.1 INFRARED SPECTROSCOPIC STUDIES OF LIMESTONE (OR $CaCO_3$).

1. Qualitative and quantitative studies.

Lander [78] considered the spectra of calcium carbonate in terms of selection rules imposed by the site symmetry of the anion. Furthermore, a number of studies between the spectra of a substance and its polymorphism were carried out. Four structures were particularly common and these are calcite, aragonite, dolomite and vaterite.

Xyla and Koutsoukos [7] performed an infrared spectroscopic quantitative analysis on the calcium carbonate polymorphs produced in situ. The characteristic bands are between 650 and 1800 cm^{-1} (6 -15 microns). In a mixture of aragonite-vaterite, the aragonite content is obtained from the ratio of the areas under the peaks 1785 and 873 cm^{-1}. Note that the peak at 1785 cm^{-1} only appear in the aragonite and not in the vaterite spectrum. The standard curves of the ratio of intensities were then used to estimate the content of three calcium carbonate polymorphs. The narrow peaks allow the assumption that the respective areas under the peaks are proportional to their heights.

Gaffey [79], showed that calcite, aragonite and dolomite have at least 7 absorption bands in the 1.60 to 2.55 microns region due to vibrational processes of the carbonate ion. Positions and widths of the bands are diagnostic of mineralogy and can be used to identify these minerals (calcite, aragonite and dolomite). Broad double bands near 1.2 microns in calcite and dolomite spectra indicate the presence of Fe^{2+}. The shape and position of the Fe^{2+} band can aid in distinguishing between calcite and dolomite. In calcite spectrum it occurs at longer wavelengths and shows more pronounced doubling than the Fe^{2+} band in dolomite spectrum.

2. Vibrational analysis

The determination of the global irreducible representations of carbonate ion in calcite crystal lattice, as determined using the method described by Fateley, Dollish and co-workers [80], is outlined in Table 3.3.

TABLE 3.3: Global irreducible representation of carbonate ion.

Atom	**A_{1g}**	**A_{2g}**	**E_g**	**A_{1u}**	**A_{2u}**	**E_u**
Ca	0	0	0	1	1	2
C	0	1	1	0	1	1
Oxy	1	2	3	1	2	3
Acoustic	0	0	0	0	-1	-1
Tot. ($CaCO_3$)	1	3	4	2	3	5

$$\Gamma^{CaCO3}_{global} = A_{1g}\,(R) + 2A_{1u}\,(0) + 3A_{2g}\,(0) + 3A_{2u}\,(IR) + 4E_g\,(R) + 5E_u(IR)$$

Active modes = A_{1g} (R) + $4E_g$ (R) + $3A_{2u}$ (IR) + $5E_u$ (IR)
Inactive modes = $3A_{2g}$ + $2A_{1u}$
Acoustic modes = A_{2u} + E_u

It was found that 5 modes were Raman-active, 8 IR-active and 5 inactive.

The global irreducible representations of calcite can be divided into the intramolecular, translational, librational (rotational) irreducible representations of CO_3^{2-} and translational irreducible representations of calcium ion.

Determination of translational irreducible representation due to Ca atoms.

Table 3.4: Correlation between site symmetry (S_6) and factor group (D_{3d}).

Degrees of fre.	No. Trans. Comp.	Site Symm.	Factor Grp.	Tot. Deger.
F^Y	t^Y	S_6	D_{3d}	$a_\xi = a_{Au} + a_E$ u
2	1(T_z)	A_u	A_{1u} A_{2u}	1 = 1 + 0 1 = 1 + 0
4	2 (T_x , T_z)	E_u	E_u	2 = 0 + 2

Therefore, the translational irreducible representation for calcite due to Ca atoms,

$\Gamma^{Ca}_{transl.} = A_{1u}$ (0) + A_{2u} (IR) + $2E_u$ (IR)

INTRAMOLECULAR IRREDUCIBLE REPRESENTATION OF CARBONATE.

Table 3.5: Correlation between molecular symmetry (D_{3h}), site symmetry (D_3) and factor group (D_{3d}).

			Mol. symm.	Site symm.	Factor grp	Tot. Degeneracy
F^Y	vib	γvib	D_{3h}	D_3	D_{3d}	$a_\xi = a_{A1'} + a_{E'} + a_{A2''}$
2	2	1	A_1'	A_1	A_{1g} A_{1u}	1 = 1 + 0 + 0 1 = 1 + 0 + 0
8	4	2	E_1'	E	E_g E_u	2 = 0 + 2 + 0 2 = 0 + 2 + 0
2	2	1	A_2''	A_2	A_{2g} A_{2u}	1 = 0 + 0 + 1 1 = 0 + 0 + 1

Therefore, the intramolecular irreducible representation for carbonate ion,

$\Gamma^{CO3}_{intramol.} = A_{1g}$ (R) + A_{1u}(0) + $2E_g$(R) + $2E_u$(IR) + A_{2g} (0) + A_{2u}(IR).

Determination of translational irreducible representation for calcite due to CO_3^{2-}

TABLE 3.4: Correlation between site symmetry (D_3) and factor group (D_{3d})

		Site symm.	Factor grp.	Total Degeneracy
F^Y	t^Y	D_3	D_{3d}	$a_\xi = a_{A2} + a_E$
2	1(T_z)	A_2	A_{2g}	1 = 1 + 0
			A_{2u}	1 = 1 + 0
4	2(T_x,T_y)	E	E_g	1 = 0 + 1
			E_u	1 = 0 + 1

Therefore, the translational irreducible representation for calcite due to CO_3^{2-},

$\Gamma^{CO3}_{transl.} = A_{2g}(0) + A_{2u}(IR) + E_g(R) + E_u(IR)$.

Determination of librational irreducible representation for calcite due to CO_3^{2-}.

Table 3.5: Correlation between site symmetry (D_3) and factor group (D_{3d}).

		Site symm.	Factor grp.	Total Degeneracy
F^Y	t^Y	D_3	D_{3d}	$a_\xi = a_{A2} + a_E$
2	1(R_z)	A_2	A_{2g}	1 = 1 + 0
			A_{2u}	1 = 1 + 0
4	2(R_x,R_y)	E	E_g	1 = 0 + 1
			E_u	1 = 0 + 1

Therefore, the librational irreducible representations for calcite due to CO_3^{2-},

$\Gamma^{CaCO3}_{lib.} = A_{2g}(0) + A_{2u}(IR) + E_g(R) + E_u(IR)$

Both the translational and librational modes of calcite due to CO_3^{2-} occur at much lower frequencies than the ones used here and are very weak. Therefore, they are mostly not detectable, and thus not a factor in this study.

Table 3.6: Summary for translational, librational and intramolecular irreducible representations for calcite.

Atom	A_{1g}	A_{1u}	A_{2g}	A_{2u}	E_g	E_u
Ca, transl.	0	1	0	1	0	2
CO_3,transl.	0	0	1	1	1	1
CO_3,librat.	0	0	1	1	1	1
CO_3,intramol	1	1	1	1	2	2
Acoustic	0	0	0	-1	0	-1
Glob($CaCO_3$)	1	2	3	3	4	5

Γ^{CaCO3}_{global} =A_{1g} (R) + 2A_{1u} (0) + 3A_{2g} (0) + 3A_{2u} (IR) + 4E_g (R) + 5E_u(IR)

Active modes = A_{1g} (R) + 4E_g (R) + 3A_{2u} (IR) + 5E_u (IR)
Inactive modes = 3A_{2g} + 2A_{1u}
Acoustic modes = A_{2u} + E_u
These are the modes of calcite reported by Fately et al [80].

Since the translational and librational modes are weak and not detectable, four of the active modes (2A_{2g} + 2E_u) given above will not appear on the FT-IR spectrum. Thus, actually, four FT-IR modes are detectable for carbonate ion.

3.3.2.2 Apparent Kinetic Models

(1). Sample A (3 - 4 g)

At 1000° C isothermal decomposition results fitted the Two-dimensional diffusion (D_2) method with correlation coefficient of 0.9264. The next best fit was found to be One-dimensional diffusion (D_1) model with an average correlation coefficient of 0.9221. The correlation coefficient for D_4 and R_3 models were 0.9216 and 0.9112, respectively.

However, the results obtained at 950° C and 900° C with correlation coefficient (R) of 0.8669 and 0.9417, respectively, for D_4 model were highest. The next best method was the R_3 model with correlation coefficients of 0.8247 and 0.9095 at 950° C and 900° C, respectively. The correlation coefficients for other theoretical kinetic models were much lower. Reduced-time plot methods at 1000° C for R_3, D_1, D_2 and D_4 were 0.99996, 0.99995, 0.99993 and 0.99992, respectively. Clearly, reduced-time plots cannot distinguish between the above four models. Therefore, the decomposition of Sample A at 1000° C can be described by either R_3, D_1, D_2 or D_2.

FIGURE 3.5: The obedience of sample A results to the following kinetic equations

(a). Contracting Volume.

(b). Three-dimensional diffusion according to Ginstling-Brounshtein.

(a).

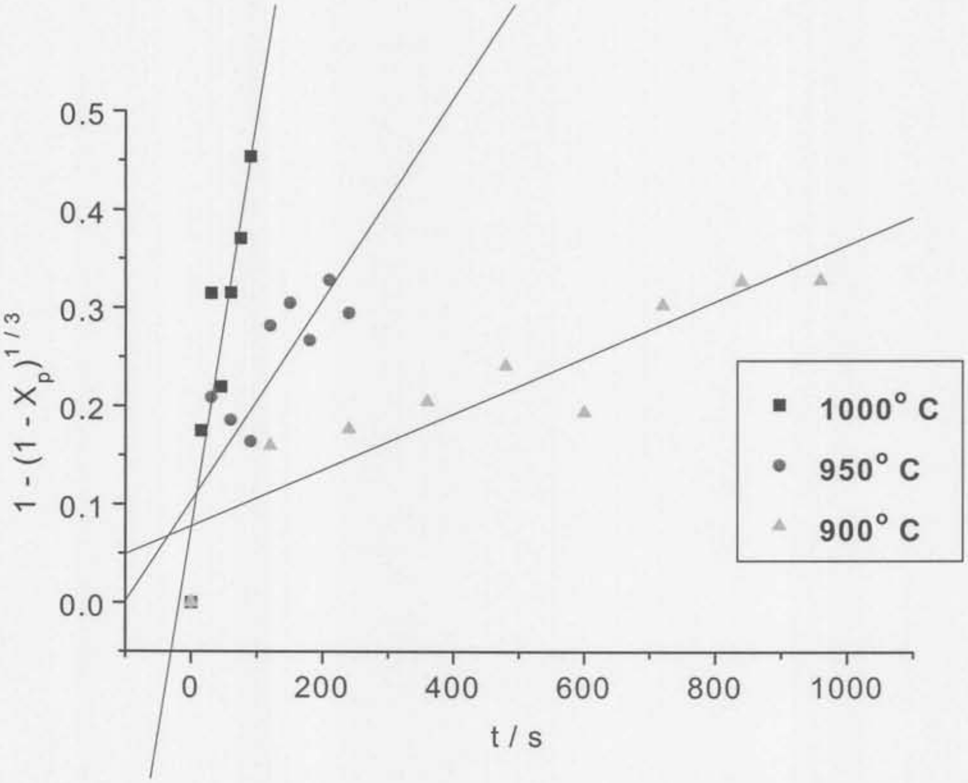

(b).

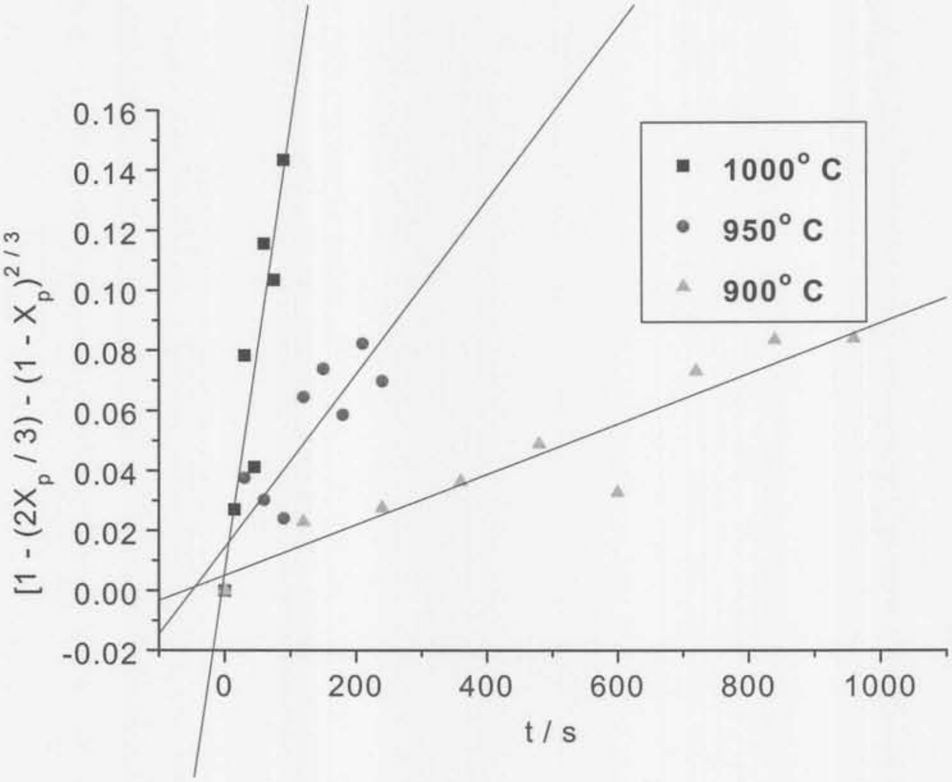
0.16
0.14
0.12
0.10
0.08
0.06
0.04
0.02
0.00
-0.02
$[1 - (2X_p / 3) - (1 - X_p)^{2/3}$
0
200
400
600
800
1000
t / s
■ 1000° C
● 950° C
▲ 900° C

(2). Sample B (5 - 6 g).

The thermal decomposition results at 1000° C fitted the Ginstling-Brounshtein model (D_4) with correlation coefficient of 0.8943. The next best fit was found to be the contracting volume (R_3) model with correlation coefficient of 0.8834. At 950° C the best fit was obtained with the Ginstling-Brounshtein model showing a correlation coefficient of 0.8661. Other models which were also very close were (D_3) three-dimensional diffusion according to Jander (R = 0.8624), (D_2) two-dimensional diffusion (R = 0.8374), (D_1) one-dimensional diffusion (R = 0.8456), (F_1) 1st order (R = 0.8520) and (R_3) contracting volume (R = 0.8273). The use of classical reduced-time plot method could not confirm the superiority of any of the above methods. The correlation coefficients (R-values) from the reduced-time plot methods were very close, ranging from 0.9997 to 0.9998. This suggests that the reaction kinetics is independent of the kinetic model.

The results obtained at 900° C fitted the following models (with correlation coefficients in brackets): D_4 (0.9537), D_1 (0.9504), D_2 (0.9108), F_1 (0.8971), R_2 (0.8946), D_3 (0.8686) and R_3 (0.8421). The classical reduced-time plots proved the following to be superior: D_2 (0.99996), F_1 (0.99995), D_4 (0.99993) and R_3 (0.99992). The coefficients for other models being much lower. Clearly the above four kinetic models cannot be distinguished from each other using the reduced-time plot methods. Therefore, the decomposition kinetics at 900° C can be described by any one of the above four models, namely, D_2; F_1; D_4 and R_3.

FIGURE 3.6: The obedience of Sample B results to the following kinetic results:

(a). Contracting Volume.

(b). Three-dimensional diffusion according to Ginstling-Brounshtein (a).

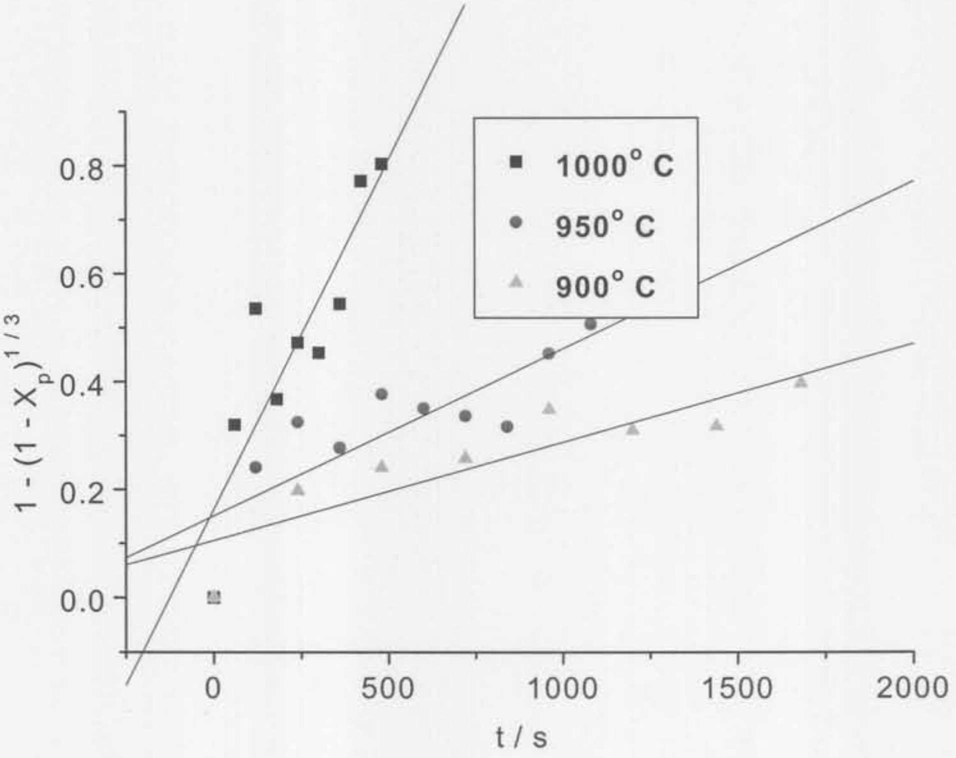
■ 1000° C
● 950° C
▲ 900° C
1 - (1 - X_p)^1/3
0.8
0.6
0.4
0.2
0.0
0
500
1000
1500
2000
t / s

(b).

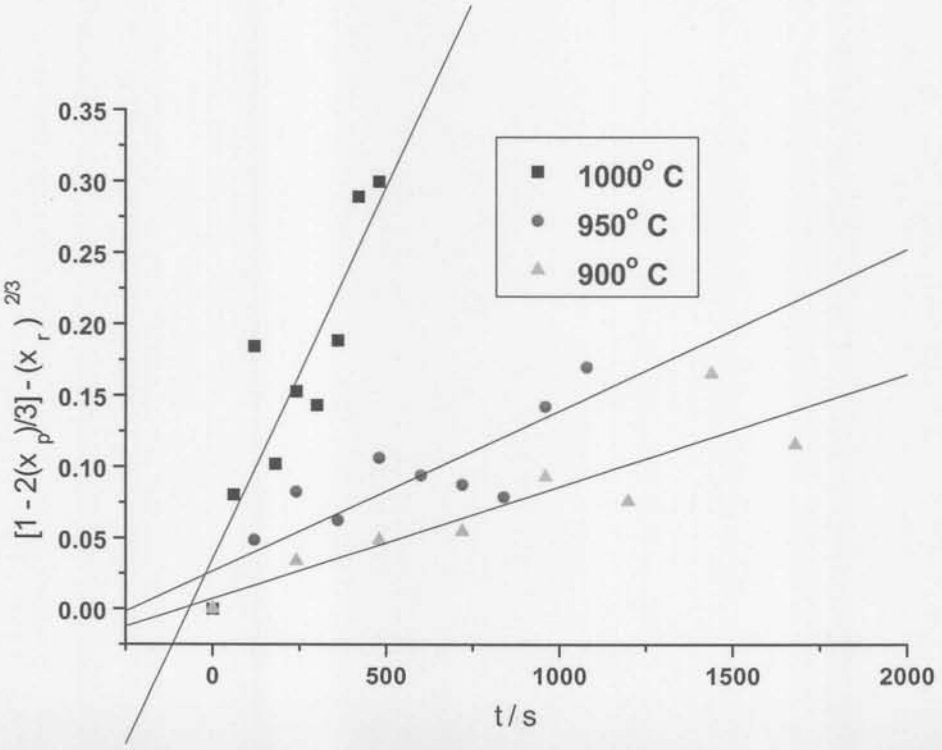
■ 1000° C
● 950° C
▲ 900° C
[1 - 2(x_p)/3] - (x_r)^2/3
0.35
0.30
0.25
0.20
0.15
0.10
0.05
0.00
0
500
1000
1500
2000
t / s

(3). Sample C (30 - 40 g)

The experimental results for decomposition at 1000° C fitted the following models best: D_4 (0.9010) and R_3 (0.8912). At 950°C the results fitted four models closely: D_1 (0.8794), D_2 (0.8743), D_4(0.8644) and R_3 (0.8626). The reduced-time plots confirmed the following models: D_1 (0.9998), R_3 (0.9996) and D_4 (0.9996). The correlation coefficient for D_2 was much lower, 0.9945.

The results at 900° C complied closely with the following models as their correlation coefficients indicate: D_4 (0.8975), R_3 (0.8828), D_3 (0.8828), D_2 (0.9022), D_1 (0.8990) and F_1 (0.8951). Using the reduced-time plots, the following models showed higher R values: R_3 (0.99991), D_4 (0.99988), D_1 (0.99961) and D_2 (0.99958).

FIGURE 3.7: The obedience of Sample C results to the following kinetic results:

(a). Contracting Volume.

(b). Three-dimensional diffusion according to Ginstling-Brounshtein

(a).

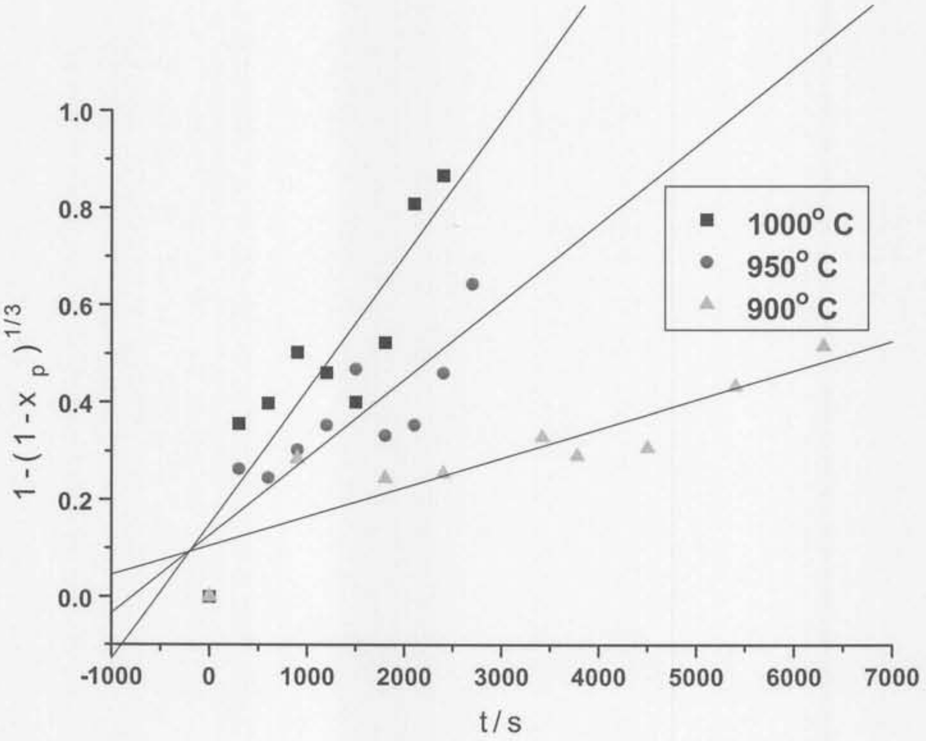

(b)

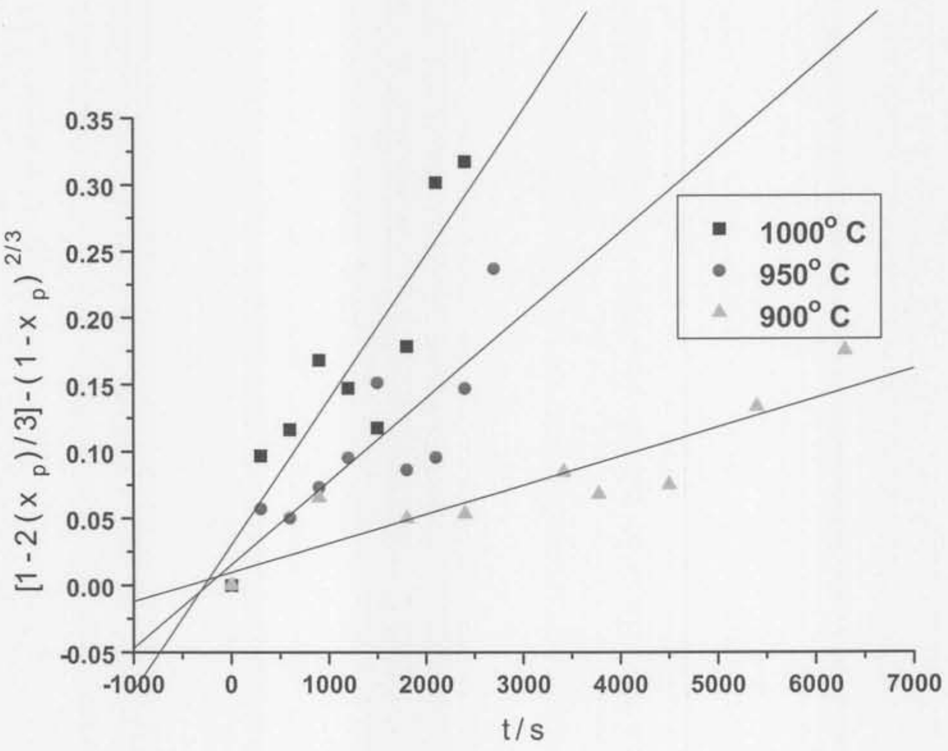

(4). Sample D (90 - 110 g)

The isothermal decomposition results at 1000° C gave the highest correlation coefficients (R) for the following models: R_3 (0.79098) and D_4 (0.78499). Notably these R values are quite low. At 950° C, the highest correlation coefficients were obtained for D_4 (0.9464) and R_3 (0.8315). The R values for other models were much lower.

The results obtained at 900° C gave the highest R values for the following models : D_4 (0.9013), A_3 (0.9011), D_3 (0.9103), A_2 (0.8996), D_2 (0.8915), D_1 (0.8575) and R_3 (0.8399). The reduced-time plots showed the highest R values for A_3 (0.99996), D_3 (0.99968), D_4 (0.9996) and R_3 (0.99959). This suggests that the reaction kinetics at 900°C can be explained in terms of A_3, D_3, D_4 and R_3.

FIGURE 3.8: The obedience of Sample D results to the following kinetic results:

(a). Contracting Volume.

(b). Three-dimensional diffusion according to Ginstling-Brounshtein

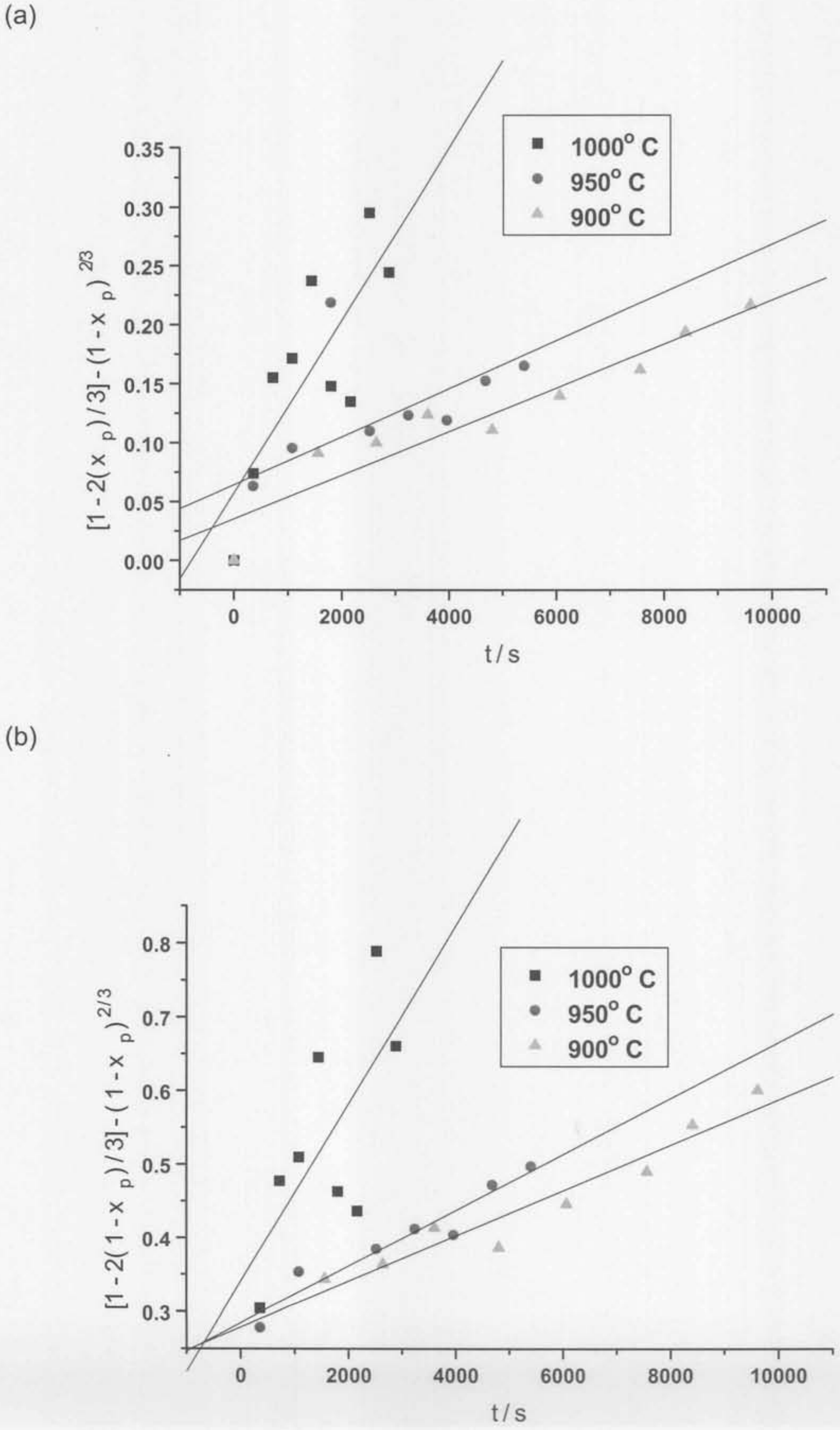

For all the rock sizes at each of the three isothermal decomposition temperatures, D_4 and R_3 appear most frequently as the kinetic models giving the best fit for the experimental results. The thermal decomposition of limestone ($CaCO_3$) has been studied extensively. The most common and well documented theoretical kinetic models describing this decomposition under different experimental conditions and atmospheres including air are D_4 and R_3 [16,17,18,20,23,61]. On these grounds, the above two models have been chosen to describe the isothermal decomposition of limestone at the three temperatures (900° C, 950° C and 1000° C).The reduced-time plots for all the rock sizes at three temperatures of decomposition are given in Appendix C.

3.3.3 <u>The Rate Constants</u>

The rate constant values with corresponding correlation coefficients for linear regression are given in Table 3.9. Both D_4 and R_3 kinetic models have been used to calculate the values for the rate constants, k, at the three temperatures for all the rock sizes.

Table 3.9: Values of the rate constants, k, for the decomposition reaction of limestone rocks.

Sample size	T (°C)	D_4		R_3	
		k(s^{-1})	R	k(s^{-1})	R
A (3 - 4 g)	1000	$1.48*10^{-3}$	0.9216	$4.17*10^{-3}$	0.9112
	950	$3.10*10^{-4}$	0.8474	$3.10*10^{-4}$	0.8247
	900	$8.00*10^{-5}$	0.9440	$2.80*10^{-4}$	0.9095
B (5 - 6 g)	1000	$5.20*10^{-4}$	0.8943	$1.30*10^{-3}$	0.8834
	950	$1.10*10^{-4}$	0.8661	$3.10*10^{-4}$	0.8273
	900	$6.00*10^{-5}$	0.9301	$1.80*10^{-4}$	0.8783
C (30 - 40 g)	1000	$1.10*10^{-4}$	0.9010	$2.80*10^{-4}$	0.8912
	950	$6.00*10^{-5}$	0.8644	$1.60*10^{-4}$	0.8626
	900	$2.00*10^{-5}$	0.8975	$6.00*10^{-5}$	0.8828
D (90 - 110g)	1000	$7.00*10^{-5}$	0.7973	$1.80*10^{-4}$	0.7910
	950	$3.00*10^{-5}$	0.9430	$8.00*10^{-5}$	0.8747
	900	$1.00*10^{-5}$	0.9013	$4.00*10^{-5}$	0.8864

The rate constants from both models, D_4 and R_3, for all the rock sizes at the different temperatures are of the same order of magnitude and indeed very close. Highest values are obtained at 1000° C and the lowest values at 900° C. This shows that the decomposition reaction increases with temperature.

In addition, there is a notable trend of increase in the rate constants as the sample size decreases. This suggests that the rate of decomposition is higher for smaller rocks than for larger ones. The surface area produced by the decomposition of smaller particles will be greater than that from decomposition of larger particles. The smaller rocks have much longer time in which to sinter, particularly at lower temperatures where samples remain in the heat for a prolonged period of time. The reaction at the lowest temperature (900° C) could not reach completion (even when the time in the furnace was extended). The reason could be that the product (lime) restricts the CO_2 diffusion or removal away from the reaction interface. Thus increasing the chance of the reverse reaction, between lime (CaO) and carbon dioxide (CO_2), to form $CaCO_3$ in the absence of moisture, to take place.

3.3.4 Arrhenius Equation Parameters

Assuming, reasonably so, that the Arrhenius equation:

$$\ln k = -E / (RT) + \ln A$$

can be applied over temperature range 900° C to 1000° C, E and A can then be determined. The results obtained for E and A from the plot of the ln k versus 1 / T in the present experiment are summarized in Table 3.10. It is interesting to note that the E and A values obtained for both kinetic expressions are of the same magnitude. Considering that experimental errors are involved, the activation energy and frequency factor values are virtually the same. Measurements show a greater tendency towards experimental errors due to the lengthy exposure to air during the grinding and the pellet preparation stages. Nevertheless, these values are well within the literature range for TG degradation studies carried out in air atmosphere ($E = 110 - 742$ kJ / mol and $A = 1.6 * 10^2 - 3.2 * 10^{33}$ min^{-1}) [57].

Table 3.10: The Arrhenius plot results for the two proposed models showing a comparison of the values of E and A for the decomposition of limestone (where A is the frequency factor and E the activation energy).

Sample size	D4			R3		
	E(kJ/mol)	A	R	E(kJ/mol)	A	R
A	362	$1.00*10^{12}$	0.9979	335	$2.29*10^{11}$	0.9989
B	267	$3.79*10^{7}$	0.9634	244	$1.14*10^{7}$	0.9617
C	213	$6.24*10^{4}$	0.9899	192	$2.26*10^{4}$	0.9911
D	242	$6.20*10^{5}$	0.9987	187	$7.92*10^{3}$	0.9977

3.4 CONCLUSION

The agreement of FT-IR results to those found using thermal methods demonstrates the potential of FT-IR spectroscopy as a useful tool in the study of solid-state reactions, most specifically for qualitative; quantitative and kinetic studies. The technique has shown that the rate of limestone decomposition increases with temperature (between 900 and 1000° C) and also with decrease in sample size. The kinetic results of limestone in air can be satisfactorily interpreted in terms of either the Contracting Volume equation (R_3): $1 - (X_r)^{1/3} = kt$ or Three-dimensional diffusion equation according to Ginstling-Brounshtein (D_4): $1 - (2 / 3)(1 - {}_{or}) - (X_r)^{2/3} = kt$. The type of samples used in this study had non-accessible internal surface area (i.e. very low particle porosity). Furthermore, initial rate of the reactions have been extremely fast. Based on these two above facts it can be assumed to follow most closely the Contracting Volume equation (R_3) [63,69,74]. However, the values of the regression coefficients support the Ginstling-Brounshtein equation.

CHAPTER 4

DETERMINATION OF THE AMOUNT OF LIMESTONE ADDITIONS TO CEMENT BLEND BY FT-IR SPECTROSCOPY

4.1 INTRODUCTION.

Cements in South Africa were classified and sold according to the contents of their constituents prior to 1996. The specification [81,82] used then accordingly prescribed the minimum and maximum levels as well as the types of mineral admixtures that could be blended with OPC (Ordinary Portland Cement). However, since the beginning of 1997 the South African cement industry adopted the European norms for cement [83], which classified it in terms of strength development and performance into certain classes. Under these specification it became possible to also use limestone as a mineral admixture or extender to Portland cements and not only masonry cement.

The addition of limestone instead of the extenders like fly ash and ground granulated blastfurnace slag (GGBS) has several important advantages for cement manufacturers. Firstly, it allowed an increase in the output of a cement factory at little additional cost and also the option to lower production costs. Furthermore, due to the packing effect [84] of the fine limestone particle, concrete produced from such a cement has a denser structure and consequently enhanced durability.

Although limestone containing Portland cement ultimately has to comply with the strength development criteria at different ages as is set out in the SABS EN 197 specifications, an analytical method to control the limestone additions is required from an operational and quality assurance point of view. Classical wet chemical techniques presented one such a procedure [85], which is based on the titration of carbon dioxide from the sample by treating it with a strong mineral acid. The amount of carbon dioxide detected can be measured in several ways and the added amount of limestone calculated by applying the ideal gas law and stoichiometric relationships. XRD measurements can also be applied [86] to calculate the amount of $CaCO_3$ in cement. However, this approach suffers from several drawbacks. Firstly, there is no guarantee that the total amount of carbon dioxide is in fact released, i.e that the reaction between the limestone and the acid is complete. Furthermore, should the Portland cement blend contain another mineral addition , like GGBS for example, there is a real possibility that additional gaseous species (H_2S) could be formed in the acid treatment step, that could lead to erroneous values for the calculated limestone addition. In the same way the presence of even small amounts of $MgCO_3$, which often occurs in limestone used for cement production, will introduce errors in the figure of the limestone content calculated from the volume of carbon dioxide released.

A simple loss-on-ignition at high temperature procedure [87] is also not completely full-proof. One has to bear in mind that the LOI value obtained will contain a contribution from the decomposition of the gypsum component, the Portland cement blend as well, which will have to be compensated for to achieve reasonably precise results. As is the case with the previous method mentioned above, GGBS additions will complicate matters further if the slag contains sulphides (as is often the case) which can be oxidised to sulphates. It should therefore be obvious that there is a need for a fast, easy method with which to measure limestone additions to Portland cement blends unambiguously and accurately.

The investigation described in this work involves the use of FT-IR spectroscopy as quantitative tool to achieving the above objectives. Furthermore, measurement using mass balance are made as the validation of the results obtained from the FT-IR technique. If the FT-IR and the mass balance techniques gives corresponding results, then the results would be acceptable.

4.2 EXPERIMENTAL

4.2.1 FT-IR MEASUREMENTS

Nine samples (basic cement and admixtures) with different percentages of added limestone were obtained from PPC Cleveland. The added amounts of limestone were 0%, 3%, 6%, 9%, 12%, 15%, 20%, 25% and 100%, the latter sample being the pure limestone. Samples were prepared for FT-IR quantitative analysis as KBr pellets. An approximate mass of 2 mg of each sample was added to 100 mg of KBr, the total mass of pellet therefore being approximately 102 mg.

Spectra were recorded in the mid infrared region (400 - 4000 cm^{-1}) in an evacuated chamber of a Bruker 113v FT-IR spectrometer. A resolution of 2 cm^{-1} was used and spectra were accumulated over 32 scans. To set a calibration curve the amount of limestone in each cement sample was determined by using the ratio I / I_o. Here “I” represents the integrated intensity of the out-of-plane vibration in $CaCO_3$ (894 - 865 cm^{-1}). This peak has been used before in the quantitative determination of $CaCO_3$ in $CaCO_3$ / $Ca(OH)_2$ mixtures (in chapter 2) as well as in the kinetic study of the decomposition of $CaCO_3$ to CaO [9, and chapter 3]. A peak remaining fairly constant in intensity throughout the samples was used to obtain the “I_o" value, by integrating the region 574 - 487 cm^{-1}. Five equivalent runs and integrations of each of the nine samples were made on the FT-IR spectrometer. For the calibration curve the ratio I / I_o was plotted against percentage limestone for all 45 sample results and for the nine averaged results.

4.2.2 MASS BALANCE MEASUREMENTS.

Ten empty porcelain crucibles were heated at 1000° C in a furnace for 1800s and then cooled in a dessicator. For each cement mixture with different percentage of limestone an accurately weighed sample (basic cement and limestone admixture) with an approximate mass of 2 g each was placed in the cooled porcelain crucibles.

The total mass (sample before decomposition plus the crucible) was measured as W_1. The samples in the crucibles were then heated in the furnace at 1000° C for 1800s. After removal from the furnace the crucibles and samples were cooled in a dessicator. The total mass (crucible plus sample) was determined again to give W_2. The percentage mass loss was then calculated as $[(W_1 - W_2) / (\text{sample mass})] * 100\%$. In order to obtain a calibration curve a graph of % mass loss vs. % limestone in the sample was plotted.

4.3 RESULTS AND DISCUSSION.

4.3.1 FT-IR MEASUREMENTS

When the FT-IR for the pure cement sample (with no limestone additions) was recorded the spectrum showed a relatively broad band, which was narrower than the rest at around 442 cm^{-1}. This band remained fairly constant, and was chosen as the analytical characteristic peak for cement. The analytical band for limestone used in this chapter is similar to that in the previous chapters and occurs around 875.8 cm^{-1}. Therefore, the two analytical bands were integrated to determine the relative amounts of the cement and limestone occurring in the sample.

Table 4.1 shows the values of the intensity ratios for multiple runs of different concentrations of $CaCO_3$ occurring in the cement blends. The linear plots (I / I_o against %$CaCO_3$) of these results are given in Figure 4.1 (which includes the 100% $CaCO_3$) and Figure 4.2 (without the 100% $CaCO_3$).

In Table 4.2 the averaged intensity (from five equivalent determinations of each sample) ratios for all cement blends are shown. The corresponding linear plots are shown in figures 4.3 and 4.4 for the results including 100% $CaCO_3$ sample and those without 100% $CaCO_3$ sample, respectively.

The information below outlines the integration ranges used to obtain results for both cement and limestone. It further, explains the symbols used in the tables and figures.

Slurry integration range = 574 - 487 cm^{-1}.
Slurry integration value, I_o = 15.4235.
Limestone integration range = 894 - 865 cm^{-1}.
Limestone integration value = I_n,
where 'n' is a natural number.

Table 4.1: Values of I / I_0 obtained by integration of the 894 - 865 cm^{-1} (I) and the 574 - 487 cm^{-1} (I_0) regions of the infrared spectra of cement blends containing various percentages of $CaCO_3$.

%$CaCO_3$	I / I_0	%$CaCO_3$	I / I_0	%$CaCO_3$	I / I_0
0	0.05759	9	0.13083	20	0.22690
0	0.05226	9	0.15035	20	0.23466
0	0.05703	9	0.13357	20	0.22188
0	0.06200	9	0.11999	20	0.21453
0	0.05981	9	0.13260	20	0.24169
3	0.08013	12	0.13960	25	0.28290
3	0.08682	12	0.12050	25	0.26693
3	0.07152	12	0.17124	25	0.24069
3	0.07253	12	0.16671	25	0.24601
3	0.09916	12	0.15097	25	0.24710
6	0.10790	15	0.16972	100	0.67180
6	0.11124	15	0.18228	100	0.75738
6	0.12305	15	0.18287	100	0.77413
6	0.12230	15	0.14738	100	0.75589
6	0.10311	15	0.17690	100	0.76713

Figure 4.1: The mid-IR spectrum of all the cement blends. From top to bottom: 100%, 25%, 20%, 15%, 12%, 9%, 6%, 3% and 0% limestone sample.

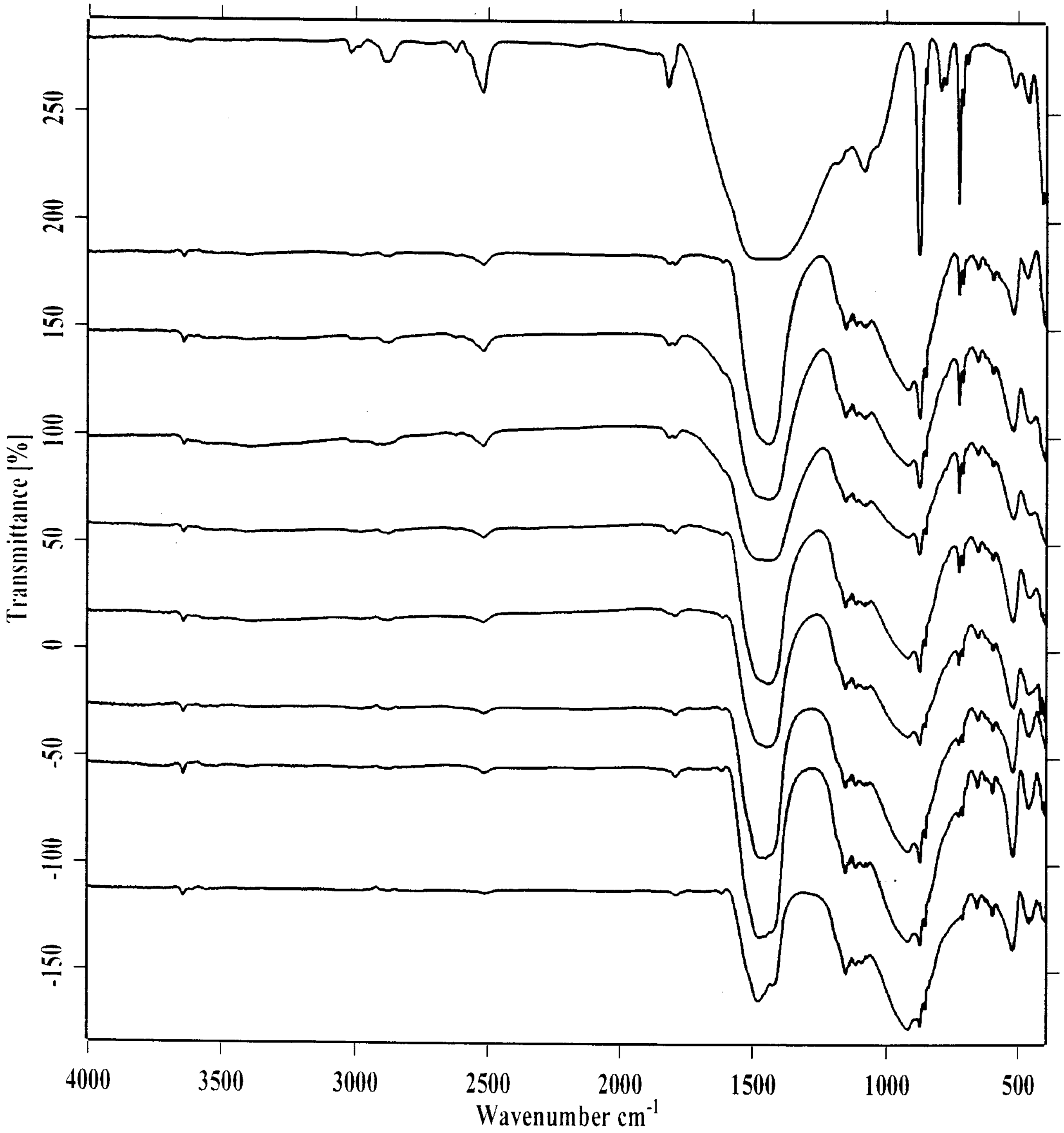

TABLE 4.2: Averaged intensity ratios for each representative percentage sample of $CaCO_3$ in cement blends.

% $CaCO_3$	**Averaged I / I_0**
0	0.05774
3	0.08203
6	0.11352
9	0.13347
12	0.14980
15	0.17183
20	0.22793
25	0.25673
100	0.74527

The mid-infrared spectra of all samples between 675 and 1075 cm^{-1} are shown in Figure 4.1. The spectra show characteristic vibrational modes for $CaCO_3$ at 875.8 cm^{-1} (out-of-plane bending) and 713 cm^{-1} (in-plane bending). The band at 875.8 cm^{-1} has been used successfully in quantifying the amount of $CaCO_3$ in $CaCO_3$ / $Ca(OH)_2$ mixtures by mid-infrared spectroscopy [see chapter 2]. The change in the intensity of this narrow and isolated peak was also utilised in the kinetic study of the decomposition of $CaCO_3$ to CaO by FT-IR [see chapter 3].

The intensity of the band clearly increased with limestone concentration in the cement blends. Integration of the infrared region from 894 to 865 cm^{-1} resulted in I-values used in the calculations. The cement blend characteristic band remained fairly constant throughout the samples. This band was used for normalisation by integrating the region 574 - 487 cm^{-1} to obtain I_0. In Table 4.1 the calculated I / I_0 values are shown for 5 runs of each representative sample.

These values are plotted as %$CaCO_3$ vs. I / I_0 to obtain the calibration curve in Fig 4.2. The average values for each sample has been determined and is shown in Table 4.2. These values are also plotted as %$CaCO_3$ vs. I / I_0 to give the calibration curve as is shown in Figure 4.4.

Figure 4.2: Plot of I / I_0 against %$CaCO_3$ for multiple results.

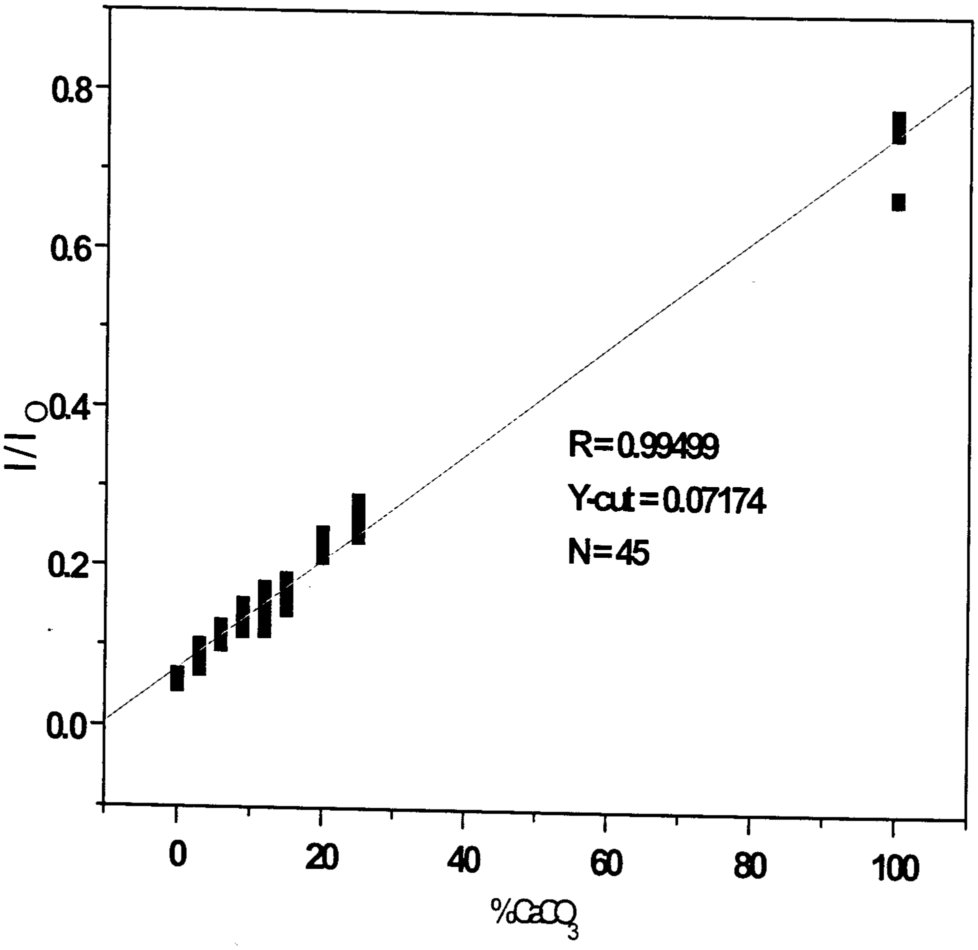

Figure 4.3: Plot of I / I_0 against %$CaCO_3$ for multiple results excluding the 100 % $CaCO_3$ result.

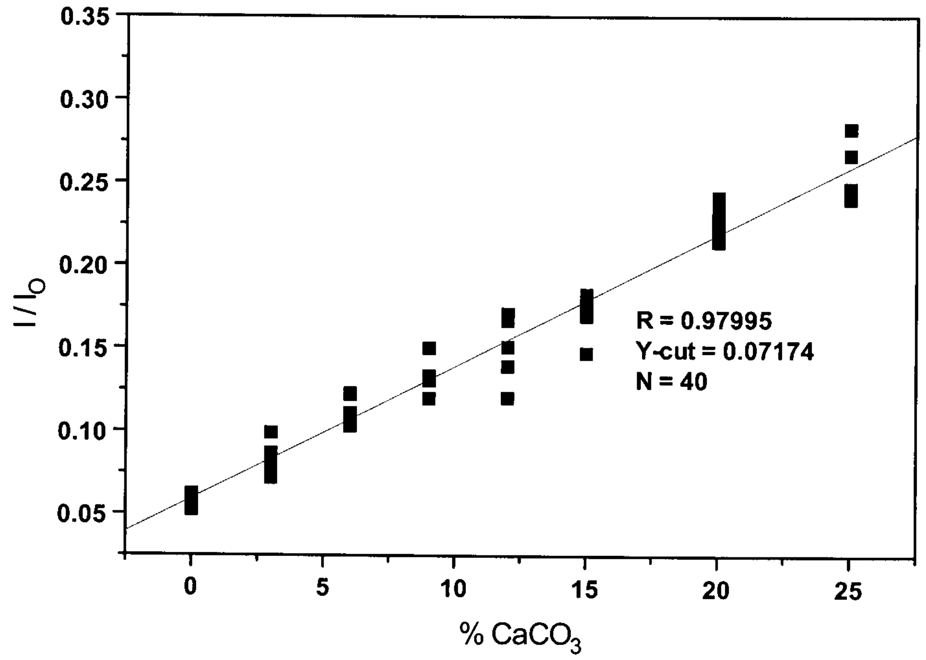

Figure 4.4: Plot of I / I_0 against % $CaCO_3$ for averaged results.

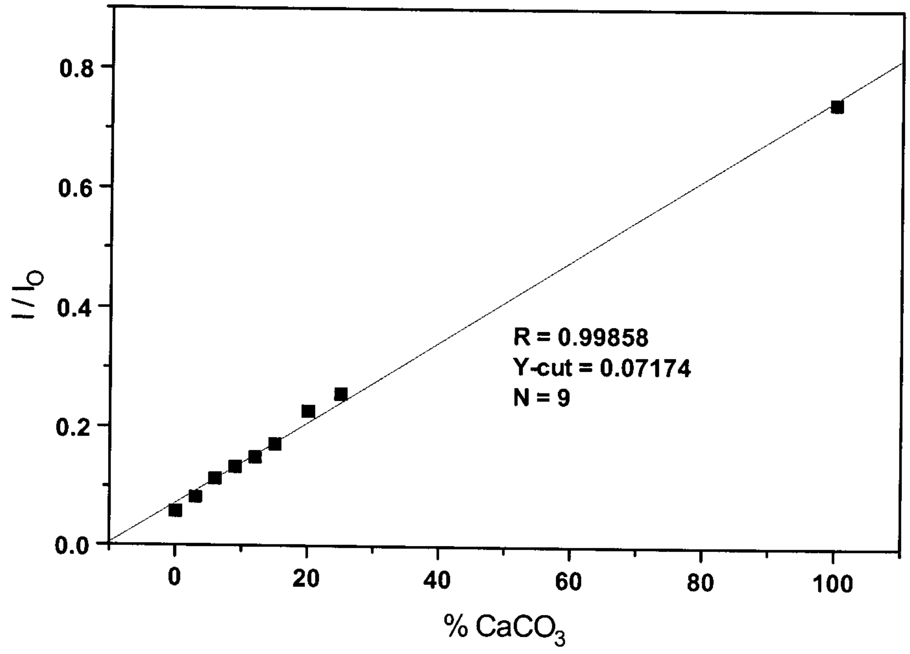

Figure 4.5: Plot of I / I_0 against % CaCO $_3$for averaged results excluding the 100% $CaCO_3$ result.

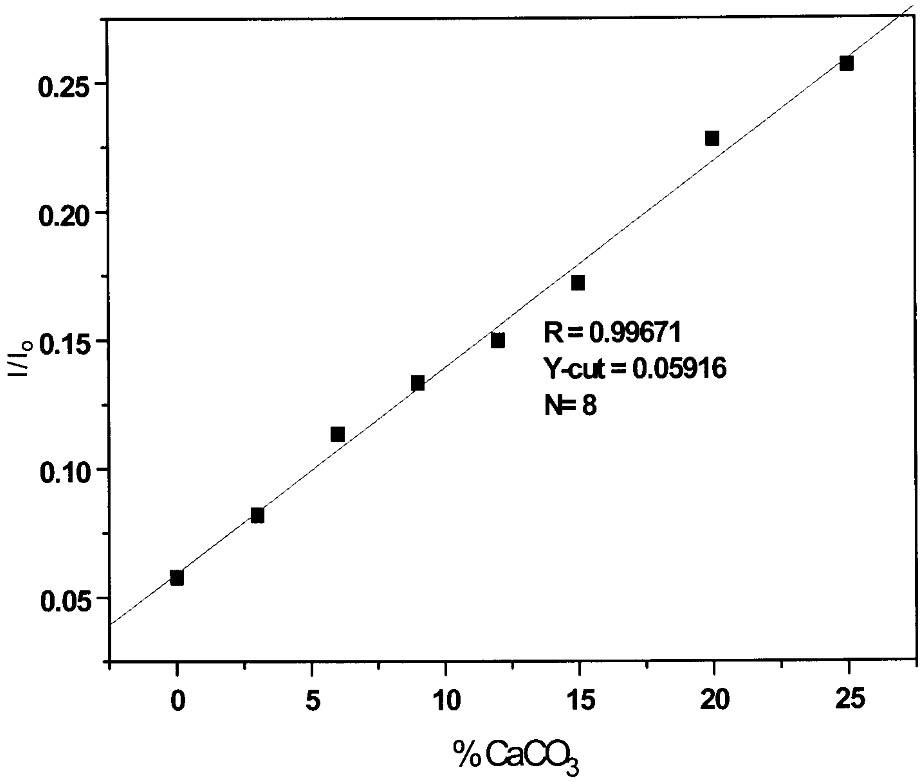

4.3.2 Mass Balance Measurements.

In Table 4.3 the mass loss of $CaCO_3$ upon heating at 1000° C is summarized. The results from Table 4.3 are plotted in Figure 4.6 and 4.7.

The following information explains symbols used in the tables and figures that follow.

W_1 = exact mass of sample and the crucible before heating.
W_2 = exact mass of sample and the crucible after heating.
Δm = mass of sample lost during heating.

TABLE 4.3: Values of %Δm for the corresponding %$CaCO_3$ in the sample.

%$CaCO_3$	Crucible (g)	W_1 (g)	W_2 (g)	Δm (g)	%Δm
0	14.64	16.64	16.45	0.19	9.50
3	19.19	21.20	21.00	0.20	9.95
6	56.50	58.51	58.25	0.26	12.94
9	53.60	55.59	55.31	0.28	14.07
12	56.11	58.11	57.84	0.27	13.50
15	60.18	62.18	61.86	0.32	16.00
20	54.68	56.69	56.29	0.40	19.90
25	54.15	56.15	55.77	0.38	19.00
100	53.16	55.16	54.22	0.94	47.00

Figure 4.6: Plot of %Δm versus %$CaCO_3$.

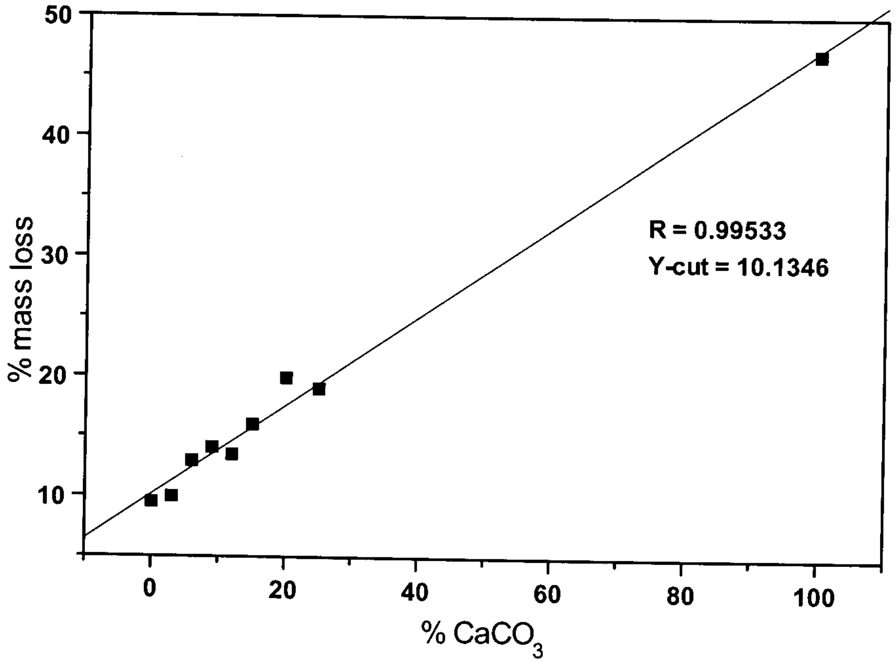

Figure 4.7: Plot of %dm versus %$CaCO_3$ excluding 100% $CaCO_3$ sample.

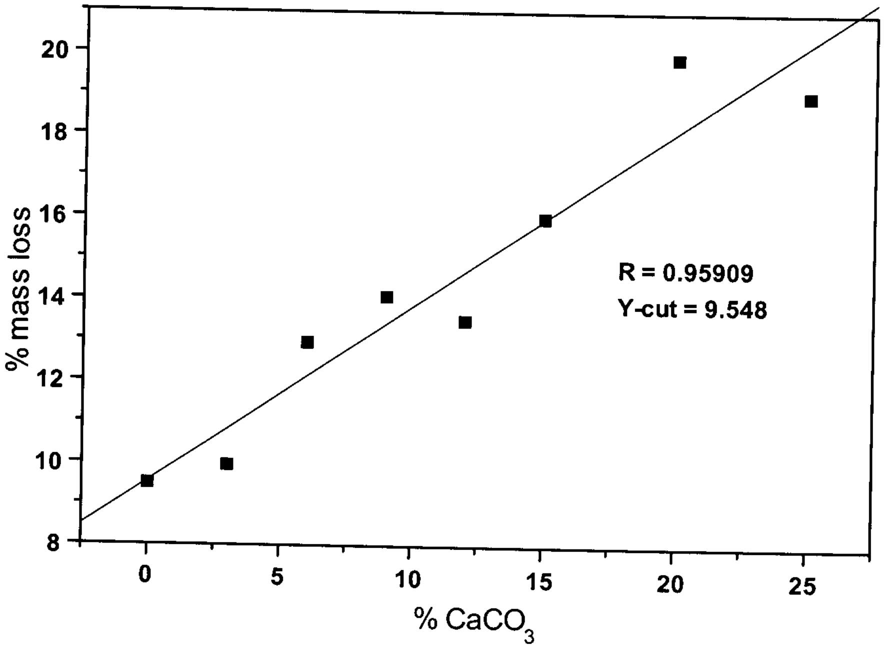

The figures and corresponding calibration curve obtained showed that the mass loss is greater for slurry samples that contained higher limestone percentages. The correlation coefficients from calibration curve were quite good, 0.99533 (including 100% sample) and 0.95909 (excluding 100% sample). These values compare well with those obtained using the FT-IR spectroscopy, 0.99499 (including the 100% sample) and 0.97995 (excluding the 100% sample) for multiple results. The results obtained from the mass balance measurements give a clear confirmation of validity of the FT-IR results.

4.4 CONCLUSION

A quantitative determination of limestone can be performed quickly and accurately by simple mid-infrared measurement with samples in the form of KBr pellets.
Higher regression coefficients could be obtained by averaging intensity measurements for each representative sample before setting the regression curve. Although samples to be analysed using this method only included %$CaCO_3$ between 0 and 25%, it was useful to include a 100% limestone sample in the regression analysis as higher values could be obtained for the regression coefficient in this manner. The amounts of limestone added to the cement slurry correspond to the amounts added to commercial cement products and therefore cover the range of interest in this particular case.

The excellent values of the regression coefficient obtained when the 100% limestone sample is included in the analysis demonstrates that this technique can also safely be applied to samples containing $CaCO_3$ percentages of more than 25%. The parameters of the experiment can be adjusted to suit the need of the analysis.
The infrared active out-of-plane mode of the carbonate ion is a sharp band and has been shown, once again, to be very suitable for use in the quantitative analysis of $CaCO_3$ by means of mid-infrared spectroscopy.

The correlation coefficients obtained using mass balance measurements are virtually the same as those obtained using FT-IR spectroscopy and thus confirm their validity. This clearly proves the potential of FT-IR spectroscopy as a quantitative tool in the study of limestone.

CHAPTER 5

GENERAL CONCLUSION

The present work consist of three interconnected parts: a) the investigation of the possible application of FT-IR to quantitative analysis of solid state reactions (calcium carbonate in $CaCO_3$ / $Ca(OH)_2$ mixures), b) kinetic studies of limestone decomposition and c) the rapid determination of the limestone content in cement blends. When the calibration curve for the quantitative analysis of $CaCO_3$ in $CaCO_3$ / $Ca(OH)_2$ mixtures was drawn, the correlation coefficient was 0.9950. This value is the same as that obtained using loss-on-ignition method (0.9950). The results obtained demonstrate the potential of FT-IR spectroscopy as a tool in the study of solid-state reactions, particularly the quantitative and kinetic studies.

When the decomposition (at 1000° C, 950° C and 900° C) of different sizes of limestone rocks in air was investigated the rate constants increased with temperature and a decrease in sample size. The highest correlation coefficients were obtained for D_4 and R_3 model, respectively. Therefore, this reaction can be satisfactorily interpreted in terms of either the contracting volume equation (R_3): $1 - (X_r)^{1/3} = kt$ or the three-dimensional diffusion equation according to the Ginstling-Brounshtein (D_4): $1 - (2X_p / 3) - (Xr)^{2/3} = kt$. The E values correspond with those in the literature for thermal methods.

The results from the rapid determination of limestone in cement blends using FT-IR yielded straight line graphs of correlation coefficients ranging from 0.9950 to 0.9986. These values further confirm that FT-IR is the most effective, easy, unambiguous and rapid method of determining the limestone content in cement mixtures. This implies that the content of limestone can be determined successfully in any product (e.g. admixture, cement, etc) containing limestone. Therefore, FT-IR can be used for quality assurance in limestone containing products.

APPENDIX A

FT-IR SPECTROSCOPY

FT-IR stands for Fourier Transform Infrared. Vibrations in molecules or in solid lattice are excited by the absorption of photons (infrared spectroscopy) or by the scattering of photons (Raman spectroscopy), electrons (electron loss spectroscopy) or neutrons (inelastic neutron scattering). In case the vibration is excited by the interaction of the bond with a wave field, as with photons and electrons, the excitation is subject to strict selection rules. Collision, on the other hand, excite all vibrational modes.

Infrared spectroscopy is the most common form of vibrational spectroscopy and the radiation falls into three categories as is indicated in Table A1 below.

Table A1: Classification of infrared radiation.

Region	Wavelength(μm-1)	Energy(meV)	Wavelength (cm-1)	Detection
Infrared	1000 - 1	1.2 - 1240	10 - 1000	-
Far IR	1000 - 50	1.2 - 25	10 - 200	lat. Vib
Mid-IR	50 - 2.5	25 - 496	200 - 4000	mol.Vib
Near-IR	2.5 - 1	496 - 1240	4000 - 10000	overtones

HISTORY

The first report of the systematic use of infrared radiation is due to Coblentz [88] in 1905 who investigated water in minerals. Investigations of hydroxyl groups and adsorbed molecules on oxides were made by Terenin and co-workers [89] in Russia in the forties. This work was done in the near infrared region, which offers the advantage that glass is transparent for the radiation in this region and the construction of cells is easy. Commercial infrared instruments became available in the mid 1940's.

THEORY OF MOLECULAR VIBRATIONS

Molecules possess discrete levels of rotational and vibrational energy. Transitions between vibrational levels occur by absorption of photons with frequencies 'v' in the mid-infrared range (Table A1). For small deviations of the constituent atoms from their equilibrium positions, the potential energy V(r) can be approximated by that of the harmonic oscillator:

$$V(r) = \frac{1}{2} k (r - r_{eq})^2 \qquad (1)$$

where V (r) is the interatomic potential

r is the distance between the vibrating atoms

r_{eq} is the equilibrium distance between atoms

k is the force constant of the vibrating bond.

The corresponding vibrational energy levels are equidistant (see figure A1).

$$E_n = (n + \frac{1}{2})hv \qquad (2)$$

$$v = \frac{1}{2} pi(k/u)^{1/2} \qquad (3)$$

$$1/u = 1/m_1 + 1/m_2 \text{ or } u = (m_1 m_2)/(m_1+m_2) \qquad (4)$$

in which

E_n is the energy of the n^{th} vibrational level

n is an integer

h is Planck's constant

v is the frequency of the vibration

k is the force constant of the bond

u is the reduced mass

m is the mass of the vibrating atoms

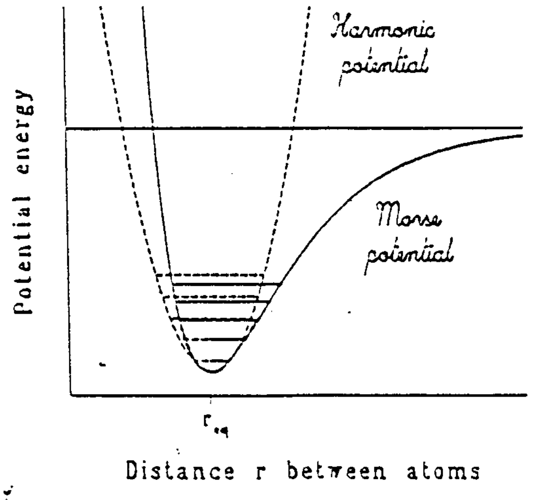

Figure A1: The harmonic potential and the Morse potential, together with vibrational energy levels. The harmonic potential is an acceptable approximation for molecular separations close to the equilibrium distance and vibrations up to the first excited level, but fails for higher excitations. The Morse potential is more realistic. Note that the separation between the vibrational levels decreases with increasing quantum number, implying, for example, that the second overtone occurs at a frequency slightly less than twice that of the fundamental vibration.

For more information see [90].

Thus, vibrational frequency increases with bond strength and decreasing mass of the vibrating atoms. Allowed transitions in the harmonic approximation are those for which the vibrational quantum number changes by one unit. Overtones, i.e. absorption of light at a whole number times the fundamental frequency, would not be possible. A selection rule for the absorption of a photon is that the dipole moment of the molecule must change during the vibration. This distinguishes infrared from Raman spectroscopy where the selection rule requires that the molecular polarizability changes during vibration.

The harmonic approximation is only valid for small deviations of atoms from their equilibrium positions. The most obvious shortcoming of the harmonic potential is that the bond between two atoms cannot break. A physically more realistic potential is the Morse potential (Figure A1):

$$V(r) = D(1 - e^{-a(r - req)})^2 - D$$

in which

V (r) is interatomic potential
r is the distance between the vibrating atoms
r_{eq} is the equilibrium distance between atoms
D is the dissociation energy of the vibrating bond
a is the parameter which controls the steepness of the potential well.

In this potential the energy levels are no longer equally spaced and overtones, i.e. vibrational transitions with n >1, become allowed. The overtone of gaseous CO at 4260 cm^{-1} (slightly less than 2 * 2143 = 4286 cm^{-1}) is an example. For small deviations of r from equilibrium, however, the Morse potential is successfully approximated by a parabola and for the interpretation of IR spectra the harmonic oscillator description is usually sufficient.

The simple harmonic oscillator analogy of a vibrating molecule has some important implications: (i) knowing the frequency, one can immediately calculate the force constant of the bond. Take note that the latter corresponds to the curvature of the interatomic potential and not to its depth, the bond energy. However, as the depth and curvature of the potential usually change hand in hand, it is often permissible to take the infrared frequency as an indicator for the strength of the bond. (ii) Isotopic substitution can be used in the assignment of frequencies to bonds in absorbed species, because frequency shifts due to isotopic substitution (of for example D for H in absorbed ethylene, or OD for OH in methanol) can be predicted directly. See Table A2 for an example.

Table A2 : C-O stretching frequency of different isotopic combinations:

Molecule	**ν (cm^{-1})**
$^{12}C^{16}O$	2143
$^{13}C^{16}O$	2096
$^{12}C^{18}O$	2091
$^{13}C^{18}O$	2042

The number of different vibrations that a molecule possesses, follows from the following considerations: A molecule consisting of N atoms has 3N degrees of freedom. Three of these are translational degrees of freedom and three are rotations of molecule along the three principal axes of inertia. Linear molecules have only two rotational degrees of freedom, as no energy change is involved in the rotation along the main axis. Thus, the number of fundamental vibrations is 3N-6 for a non-linear and 3N-5 for linear molecules. In addition , there are overtones and combinations of fundamental vibrations. However, not all vibrations are visible.

Figure A2: Normal modes of vibration of planar XY_3 molecules [91].

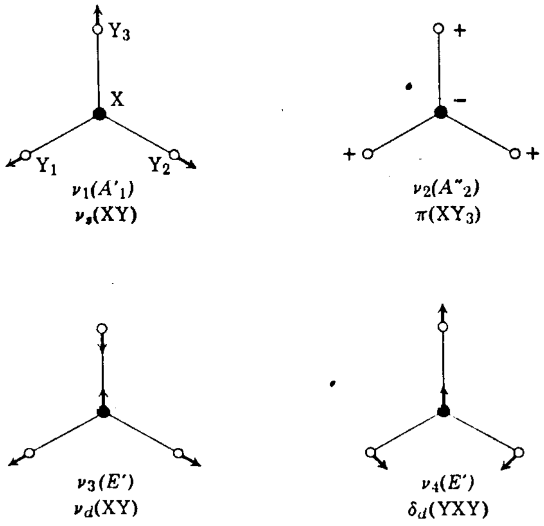

$\nu_1(A'_1)$
$\nu_s(XY)$

$\nu_2(A''_2)$
$\pi(XY_3)$

$\nu_3(E')$
$\nu_d(XY)$

$\nu_4(E')$
$\delta_d(YXY)$

There are four types of vibrations, as illustrated in Figure A2, each with a characteristic symbol:

- Stretching vibrations (symbol v_s), change of the bond length.
- Bending vibrations in one plane (symbol δ_d), changing bond angles but bond lengths remaining unaltered (in larger molecules further divided into rocking, twisting and wagging vibrations)
- Bending vibrations out of plane (symbol y), in which one atom oscillates through a plane defined by at least three neighbouring atoms.
- Torsion vibrations (symbol τ) changing the angle between two planes through atoms.

Generally, the frequencies of these vibrations decrease in the order $\nu > \delta > \gamma > \tau$. Furthermore, vibrations are divided into symmetric and asymmetric vibrations (V_s and V_{as}). For more details see textbooks on infrared spectroscopy [45,92-94].

Absorption of an infrared photon occurs only if a dipole moment changes during the vibration. Therefore , not all vibrations can be observed. It is not necessary that the molecule possess a permanent dipole. It is sufficient if a dipole moment changes during the vibration. The intensity of the infrared band is proportional to the change in dipole moment. This statement explains why species with polar bonds, e.g. CO, NO and OH exhibit strong IR bands , whereas covalent bonds, e.g. C-C or N=N absorb infrared light only weakly and molecules such as H_2 and N_2 are not infrared active at all. However, the magnitude of dipole moments during the vibration are not known.

Figure A3 : Fundamental vibrations of several molecules [90].

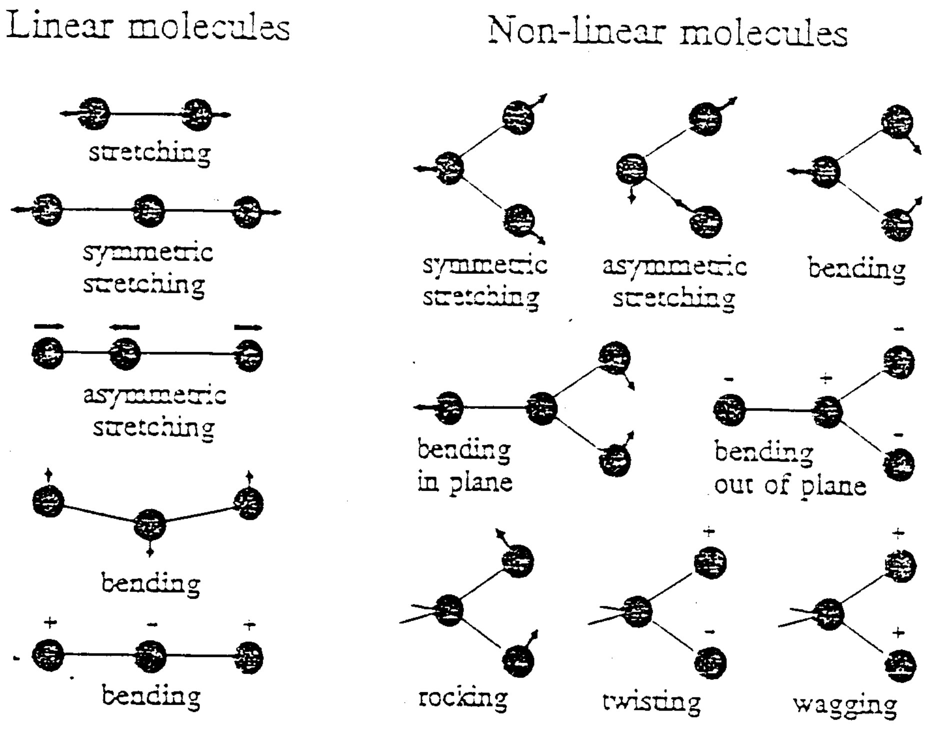

The group frequency concept states that functional groups in molecules may be treated as independent oscillators irrespective of the larger structure to which they belong. For example, C=C bond of the -CH=CH_2 group varies no more than 1651 cm^{-1} in propylene, where it is bound to methyl group, to 1632 cm^{-1} when it is bound to the much heavier CH_2Br group in CH_2Br-CH=CH_2 [94]. As a consequence, infrared frequencies are characteristic of certain bonds in molecules. The following classification of characteristic stretching frequencies are useful for interpreting vibrational spectra.

The infrared region between 4000 and 200 cm^{-1} can roughly be divided into four main regions:

- X-H stretch region (4000 - 200 cm^{-1}), where strong contributions from OH, NH CH and SH stretching vibrations are observed.
-Triple bond region (2500 - 2000 cm^{-1}), where contributions from gas phase CO (2143 cm^{-1}) and linearly adsorbed CO (2000 - 2200 cm^{-1}) are seen.
- Double bond region (2000 - 1500 cm^{-1}), where in catalytic studies bridge bonded CO , as well as carbonyl groups in adsorbed molecules (around 1700 cm^{-1}) absorb.
- The fingerprint region (1500 - 500 cm^{-1}), where all single bonds between carbon and elements such as nitrogen, oxygen, sulphur and halogens absorb.
- The M-X or metal-adsorbate region (around 200 - 450 cm^{-1}) where the metal-carbon, metal-oxygen stretching frequencies in the spectra of adsorbed species are absorbed.

Correlation charts should be consulted for more precise assignment [44,92-94].

EQUIPMENT

The first generation of infrared spectrometers was of the energy dispersive type: A monochromator (initially a prism, after the mid 1960's as a grating) selects the wavelength of interest from the continuum emitted by the infrared source, and the transmission corresponding to that particular frequency produced by the sample can be measured. Presently, energy dispersive instruments have largely been abandoned in favour of Fourier Transform Infrared (FT-IR) spectrometers operating on the principle of the Michelson interferometer. These instruments have great advantage that the entire spectrum is obtained for each scan the interferometer makes, with the result that the total collection time needed to measure a spectrum is much lower. For further treatment of the Fourier Transform technique see literature [95].

Optical components can be made of NaCl (transparent from 650 - 4000 cm^{-1}), KBr with a low energy cut-off of 400 cm^{-1} or CsI with an even more favourable cut-off of 200 cm^{-1}. The source is usually a temperature-stabilized ceramic filament operating around 1500 K. The detector may be a slowly reacting thermocouple in energy dispersive instruments, but has to be a fast response device in FT-IR. The standard for routine applications is the deuterium triglycine sulphate or DTGS detector, while the liquid nitrogen cooled mercury Cadmium telluride or MCT detector is used for more demanding applications, e.g. reflection absorption infrared spectroscopy (RAIRS).

APPENDIX B

VIBRATIONAL SPECTROSCOPIC STUDY.

DETERMINATION OF THE GLOBAL IRREDUCIBLE REPRESENTATIONS.

Global irreducible representation is the sum of intramolecular, translational, librational irreducible representation of carbonate ion and the translational irreducible representation of calcium ion. These representations provide all the vibrational (IR and Raman) bands that the ion possesses. Bands are also distinguished from each other as IR-active, Raman-active, inactive and acoustic. The carbonate is strongly covalent and would be expected to exhibit vibrational frequencies very close to those of the free ions. However, there are sets of internal vibrations. These two sets are constrained by the factor group symmetry to vibrate either in phase or in anti-phase to each other with respect to the centre of symmetry. Thus the internal modes form a Raman-active set coupled in phase and an IR-active set coupled anti-phase.

The internal and lattice modes of calcite :

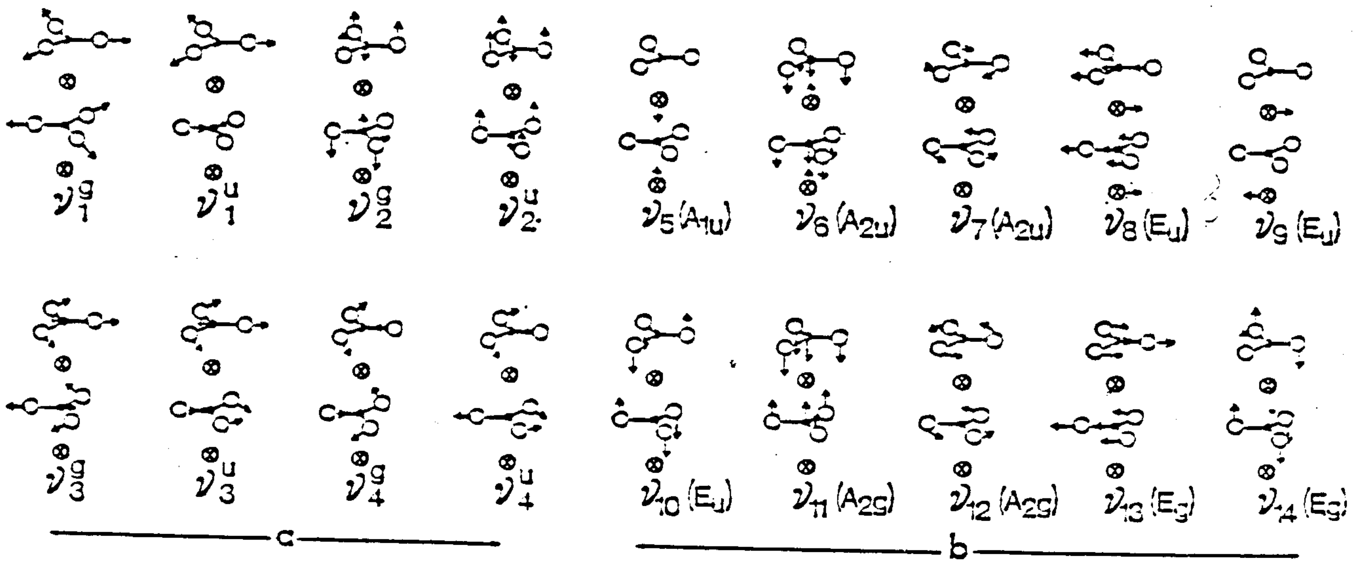

FIGURE B1: a. The internal modes of the CO_3^{2-} ion in calcite. Notice the difference between the in-phase (g-type) modes and anti-phase (u-type) modes. b. The lattice modes of the calcite structure. The contrast between translatory and rotatory modes is apparent [68].

It should be noted that the molecular symmetry of the CO_3^{2-} ion, D_{3d}, is not a subgroup of the factor group D_{3d} but that the site group is a subgroup of both. If one classifies the internal modes according to the site group symmetry as proposed by Haldford [47] and Winston and Haldford [48] a descent of symmetry argument yields.

Table B1: Correlation between molecular and site group for carbonate ion.

Molecular Group D_{3h}	Site Group D_3
A_1' (v_1)	A_1 Raman
A_2'' (v_2)	A_2 IR
E' (v_3, v_4)	E IR + Raman

The selection rules are exactly the same as those obtained by factor group analysis, but the small frequency shift between IR and Raman measurements is not taken into account.The vibrations of the CO_3^{2-} groups against the cations will produce a set of low-frequency lattice mode. Some consist of translational motions of the cation and CO_3^{2-} groups against each other and some consist of librational motions of the CO_3^{2-} molecule. These latter correspond to the free rotations of an unbound molecule.

The presence of a metal ion in $CaCO_3$ influences the modes of vibration of CO_3^{2-}. For example, BCl_3 is a trigonal planar molecule like CO_3^{2-} and hence they have the same molecular symmetry, D_{3h}. However, the modes of vibrations of CO_3^{2-} in $CaCO_3$ are different from those of BCl_3 because of the presence of Ca^{2+}, i.e the crystal lattice. Therefore, calcium carbonate will depict lattice modes, instead of a free ion modes, when analysed using vibrational spectroscopy.

To determine the global irreducible representations of calcite we need the X-Ray crystallographic data of calcite crystal lattice.
Calcite ($CaCO_3$) structure. Representative example of $CaCO_3$. X-Ray data D_{3d}^6 - R_{3c}^- (space group 167), $Z^B = 2$, D_{3d}^6 = site symmetry, D_{3d} = factor group.
Z^B is the number of $CaCO_3$ compounds in a primitive unit cell.

Table B2: X-Ray crystallographic data for calcite.

Number of atoms in equivalent site	Atoms	Wickoff site	Schonflies notation for site
2	Ca	b	S_6
2	C	a	D_3
6	oxy	e	C_2

Since $Z^B = 2$ there are 2Ca's, 2C's and 6O's (or oxy atoms) in a primitive unit cell. From the above table calcium atoms occupy site symmetry 'b' or S_6, carbon atoms 'a' or D_3 and oxygen atoms 'e' or C_2.

Determination of translational irreducible representation due to Ca atoms.

Table B3: Correlation between site symmetry (S_6) and factor group (D_{3d}).

Degrees of fre.	No. Trans. Comp.	Site Symm.	Factor Grp.	Tot. Deger.
F^Y	t^Y	S_6	D_{3d}	$a_{\xi} = a_{A u} + a_{E}$ u
2	$1(T_z)$	A_u	A_{1u}	1 = 1 + 0
			A_{2u}	1 = 1 + 0
4	$2 (T_x , T_z)$	E_u	E_u	2 = 0 + 2

$F^y = t^y * Z^B$

The irreducible representations (A_u and E_u) which occur below the site symmetry S_6, are obtained from the character tables under S_6 corresponding to translations (T_x,T_y and T_z). When site symmetry S_6 is correlated with the factor group D_{3d} the corresponding symmetry species are A_{1u}, A_{2u} (for site symmetry A_u) and E_u (for site symmetry E_u) as indicated on the table above.

Total degeneracy was calculated from the following data:

Table B4: Degeneracy values for symmetry species.

Symmetry species	Degeneracy (C_{ξ})
A	1
B	1
E	2
F (T)	3
G	4
H	5

$a_{Au} = F^{Au} / (C_{A1u} + C_{A2u}) = 2 / (1 + 1) = 1$

$a_{Eu} = F^{Eu} / C_{Eu} = 4 / 2 = 2$

Therefore, the translational irreducible representation due to Ca is as follows:

$\Gamma^{C}_{trans} = A_{1u} + A_{2u} + 2E_{u}$.

Determination of the translational irreducible representation due to carbon atom, C.

$Z^B = 2$, then number of carbon atoms is 2. C atoms occupy the site ‘a’ or D_3. Following the procedure as above correlation between site symmetry and factor group is given below:

Table B5: Correlation between site symmetry (D_3) and factor group (D_{3d}).

		Site symm.	Factor grp.	Total Degeneracy
F^Y	t^Y	D_3	D_{3d} •	$a_\xi = a_{A2} + a_E$
2	$1(T_z)$	A_2	A_{2g}	1 = 1 + 0
			A_{2u}	1 = 1 + 0
4	$2(T_x,T_y)$	E	E_g	1 = 0 + 1
			E_u	1 = 0 + 1

where

$F^y = t^y * Z^B$ (the degree of freedom).

t^y = the number of translational components.

$$a_{A2} = F^{A2} / (C_{A2g} + C_{A2u}) = 2 / (1+1) = 1$$

$$a_E = F^E / (C_{Eg} + C_{Eu}) = 4 / (2 + 2) = 1$$

Therefore, the translational irreducible representation due to carbon atom, C,

$\Gamma^C_{trans} = A_{2g} + A_{2u} + E_g + E_u$.

Determination of the translational irreducible representation due to 'O' atom.

Z^B = 2, therefore there are 6'O' atoms in each primitive unit cell. Each 'O' atom occupies site 'e' and has the site symmetry C_2. The factor group is still D_{3d}.

Table B6: Correlation between site symmetry (C_2) and factor group (D_{3d}).

		Site symm.	Factor grp.	Total Degeneracy
F^{Y}	t^{Y}	C_2	D_{3d}	$a_{\xi} = a_A + a_B$
6	$1(T_z)$	A	A_{1g}	$1 = 1 + 0$
			A_{1u}	$1 = 1 + 0$
			E_g	$1 = 1 + 0$
			E_u	$3 = 1 + 2$
12	$2(T_x, T_y)$	B	E_u	$3 = 1 + 2$
			E_g	$3 = 1 + 2$
			A_{2g}	$2 = 0 + 2$
			A_{2u}	$2 = 0 + 2$

Therefore, the translational irreducible representation due to the oxy atoms 'O',
$\Gamma^{O}_{trans} = A_{1g} + A_{1u} + 2A_{2g} + 2A_{2u} + 3E_g + 3E_u$.

Table B7: Summary for translational irreducible representation.

Atom	A_{1g}	A_{2g}	E_g	A_{1u}	A_{2u}	E_u
Ca	0	0	0	1	1	2
C	0	1	1	0	1	1
Oxy	1	2	3	1	2	3
Acoustic	0	0	0	0	-1	-1
Tot. ($CaCO_3$)	1	3	4	2	3	5

The acoustic modes are obtained from the character tables for the relevant molecular symmetry and corresponds to the translational components. They are not detectable as the fundamental modes.

Thus, the global irreducible representation of $CaCO_3$, $\Gamma^{CaCO3}_{global} = A_{1g}$ (R) + $3A_{2g}$ (0) + $4E_g$ (R) + $2A_{1u}$ (0) + $3A_{2u}$ (IR) + $5E_u$ (IR).

By using the character tables, the activity of each irreducible representation was determined to be 5 Raman-active modes, 8 IR-active modes and 5 inactive modes.

Inactive irreducible modes = $3A_{2g} + 2A_{1u}$
Acoustic modes = $A_{2u} + E_u$.

CONFIRMATION AND VALIDATION OF THE ABOVE CALCULATED GLOBAL IRREDUCIBLE REPRESENTATIONS.

In order to confirm and validate the calculated global translational irreducible modes of calcium carbonate; the molecular vibration, librations, intramolecular vibrations and translations are calculated individually and then added. Their sum should be the same as the global translational irreducible modes.

MOLECULAR VIBRATIONAL IRREDUCIBLE REPRESENTATIONS

The vibrations of calcite in the mid-infrared region is mainly the vibrations of the carbonate anion. CO_3^{2-} is a trigonal planar ion. Therefore, it has the following symmetry elements: E, $2C_3$, $3C_2$, a_h, a_v (where 'a_h' is the perpendicular mirror and 'a_v' is the vertical mirror).

From the point group chart, CO_3^{2-} has a molecular symmetry of D_{3h}.

CO_3^{2-} = 1C + 3Oxy.

Molecular symmetry is D_{3h}^1. Therefore, using the site symmetry tables, the sites occupied by the individual atoms of CO_3^{2-} are as follows:
'C' occupies D_{3h} and 'oxy' atoms occupy C_{2v}.

Determination of intramolecular irreducible representations due to carbon atom, C.

'C' occupies site D_{3h} , Z = 1, because there is 1'C' in CO_3^{2-}. Its molecular symmetry is D_{3h}.

Table B8: Correlation between site symmetry (D_{3h}) and molecular symmetry (D_{3h}).

		Site symm.	Factor grp.	Total Degeneracy
F^{Y}	t^{Y}	D_{3h}	D_{3h}	$a_{\xi} = a_{A2''} + a_{E'}$
2	$2(T_x,T_y)$	E'	E'	1 = 0 + 1
1	$1(T_z)$	A_2''	A_2''	1 = 1 + 0

where E' and A_2'' for site and molecular symmetry D_{3h} are translational components (T_x,T_y and T_z) from the character and correlation tables.

t^{y} - the number of translational components corresponding to the symmetry species.
$F^{y} = Z^{B} * t^{y}$ - the degrees of freedom.

$$a_{E'} = F^{E'} / a_{CE'} = 2 / 2 = 1$$

$$a_{A2''} = F^{A2''} / a_{CA2''} = 1 / 1 = 1$$

Therefore, the molecular vibration irreducible representation due to 'C',
$\Gamma^{C}_{i\ ntramol.} = E' + A_2''$

Determination of the intramolecular irreducible representation due to 'oxy' group.

Site symmetry of 'oxy' group = C_{2v}
Molecular symmetry = D_{3h}
Z = 3, because there are 3 'O' atoms in CO_3^{2-}

Table B9: Correlation between site symmetry (C_{2v}) and molecular symmetry (D_{3h}).

		Site symm.	Mol. Symm.	Total Degeneracy
F^Y	t^Y	C_{2v}	D_{3d}	$a_\xi = a_{A1} + a_{B1} + a_{B2}$
3	$1(T_z)$	A_1	A_1'	1 = 1 + 0 + 0
			E'	2 = 1 + 0 + 1
3	$1(T_x)$	B_1	A_2''	1 = 0 + 1 + 0
			E''	1 = 0 + 1 + 0
3	$1(T_y)$	B_2	A_2'	1 = 0 + 0 + 1
			E'	2 = 1 + 0 + 1

$a_{A1} = F^y / (a_{CA1'} + a_{CE'}) = 3 / (1 + 2) = 1$

$a_{B1} = F^y / (a_{CA2''} + a_{CE''}) = 3 / (1 + 2) = 1$

$a_{B2} = F^y / (a_{CA2'} + a_{CE'}) = 3 / (1 + 2) = 1$

Therefore, the intramolecular irreducible representation due to 'oxy' group,

$\Gamma^{O}_{intramol.} = A_1' + A_2' + 2E' + A_2'' + E''$

Table B10: Summary for molecular vibrational irreducible representations.

Atom	**A_1'**	**A_2'**	**E'**	**A_1''**	**A_2''**	**E"**
C	0	0	1	0	1	0
O	1	1	2	0	1	1
Rot. Acoustic	0	-1	0	0	0	-1
Tra. Acoustic	0	0	-1	0	-1	0
Tot. ($CaCO_3$)	1	3	2	0	1	0

Therefore, carbonate ion molecular vibration irreducible representation,

$\Gamma^{CO3}_{mol.vib.} = A_1' + 2E' + A_2''$ i)

From the character tables, the infrared-active symmetry species corresponds to T_x,T_y and T_z, while the Raman-active symmetry species corresponds to $\alpha_{xx} + \alpha_{yy}$, α_{zz}, ($\alpha_{xx} - \alpha_{yy}$, α_{xy}) and (α_{yz}, α_{zx}) of D_{3h}.

Then, $\Gamma^{CO3}_{mol.vib.} = A_1'$ (R) + 2E' (IR, R) + A_2'' (IR)

There are 3 Raman-active and 3 Infrared-active molecular vibrations.

INTRAMOLECULAR IRREDUCIBLE REPRESENTATION OF CARBONATE.

Z^B = 2, the number of molecules in a primitive unit cell.

Molecular symmetry of ‘C’ = D_{3h} [corresponding symmetry species obtained from i) above].

Site symmetry = D_3 [corresponding symmetry species obtained from correlation tables].

Factor group = D_{3d} [corresponding symmetry species obtained from correlation tables]

F^y = degrees of freedom

$\gamma vib = a_Y * C_Y$

a_Y = coefficient of symmetry species in i).

C_Y = degeneracy of symmetry species.

$vib = a_y * Z^B$

$F^y = Z^B * \gamma vib = vib * C_Y$

Table B11: Correlation between molecular symmetry (D_{3h}), site symmetry (D_3) and factor group (D_{3d}).

			Mol. symm.	**Site symm.**	**Factor grp**	**Tot. Degeneracy**
F^y	vib	γvib	D_{3h}	D_3	D_{3d}	$a_\xi = a_{A1'} + a_{E'} + a_{A2"}$
2	2	1	A_1'	A_1	A_{1g}	1 = 1 + 0 + 0
					A_{1u}	1 = 1 + 0 + 0
8	4	2	E'	E	E_g	2 = 0 + 2 + 0
					E_u	2 = 0 + 2 + 0
2	2	1	$A_2"$	A_2	A_{2g}	1 = 0 + 0 + 1
					A_{2u}	1 = 0 + 0 + 1

$a_{A1'} = F^{A1'} / C_{A1} = 2 / 1 = 2$

$a_{E'} = F^{E'} / C_E = 8 / 2 = 4$

$a_{A2"} = F^{A2"} / C_{A2} = 2 / 1 = 2$

Therefore, the intramolecular irreducible representation for carbonate ion,

$$\Gamma^{CO3}_{i\,n\,tra.\ mol.} = A_{1g}\,(R) + A_{1u}\,(0) + 2E_g\,(R) + 2E_u\,(IR) + A_{2g}\,(0) + A_{2u}\,(IR).$$

DETERMINATION OF TRANSLATIONAL IRREDUCIBLE REPRESENTATION FOR CALCITE.

Translational irreducible representation due to Ca atoms.

Ca atoms occupy S_6 symmetry site.

$Z^B = 2$, number of molecules in a primitive unit cell.

Factor group = D_{3d}

t^y = number of translational components

$F^y = t^y * Z^B$

Table B12: Correlation between site symmetry (S_6) and Factor group (D_{3d}).

		Site symm.	Factor grp.	Total Degeneracy
F^Y	t^Y	S_6	D_{3d}	$a_\xi = a_{Au} + a_{Eu}$
2	1(T_z)	A_u	A_{1u}	1 = 1 + 0
			A_{2u}	1 = 1 + 0
4	2(T_x,T_y)	E_u	E_u	2 = 0 + 2

$$a_{Au} = F^{Au} / (C_{A1u} + C_{A2u}) = 2 / (1 + 1) = 1$$

$$a_{Eu} = F^{Eu} / C_{Eu} \quad = 4 / 2 = 2$$

Therefore, the translational irreducible representation for calcite due to Ca atoms,

$$\Gamma^{Ca}_{transl.} = A_{1u}\ (0) + A_{2u}\ (IR) + 2E_u\ (IR)$$

Determination of translational irreducible representation for calcite due to CO_3^{2-}.

'C' is the central atom and therefore any perturbation on the carbon atom will affect the three oxygen atoms in the same way.

$Z^B = 2$

Site symmetry = D_3

Factor group = D_{3d}

Table B13: Correlation between site symmetry D_3 and factor group D_{3d}.

		Site symm.	Factor grp.	Total Degeneracy
F^Y	t^Y	D_3	D_{3d}	$a_\xi = a_{A2} + a_E$
2	1(T_z)	A_2	A_{2g}	1 = 1 + 0
			A_{2u}	1 = 1 + 0
4	2(T_x,T_y)	E	E_g	1 = 0 + 1
			E_u	1 = 0 + 1

$a_{A2} = F^{A2} / (C_{A2g} + C_{Au}) = 2 / (1 + 1) = 1$

$a_E = F^E / (C_{Eg} + C_{Eu}) = 4 / (2 + 2) = 1$

Therefore, the translational irreducible representation for calcite due to CO_3^{2-},
$\Gamma^{CO3}_{transl.} = A_{2g}(0) + A_{2u}(IR) + E_g(R) + E_u(IR)$

<u>Determination of librational irreducible representation for calcite due to CO_3^{2-}.</u>

Again, the central atom in carbonate ion is ‘C’ and therefore any perturbation applied to the carbon atom will affect the three oxygen atoms in the same way, since they are covalently bonded to the central ‘C’ atom. Thus the libration of CO_3^{2-} is actually the libration of the ‘C’ atom.

Table B14: Correlation between site symmetry (D_3) and factor group (D_{3d}).

		Site symm.	Factor grp.	Total Degeneracy
F^Y	t^Y	D_3	D_{3d}	$a_\xi = a_{A2} + a_E$
2	$1(R_z)$	A_2	A_{2g}	1 = 1 + 0
			A_{2u}	1 = 1 + 0
4	$2(R_x,R_y)$	E	E_g	1 = 0 + 1
			E_u	1 = 0 + 1

$a_{A2} = F^{A2} / (C_{A2g} + C_{Au}) = 2 / (1 + 1) = 1$

$a_E = F^E / (C_{Eg} + C_{Eu}) = 4 / (2 + 2) = 1$

Therefore, the librational irreducible representations for calcite due to CO_3^{2-},
$\Gamma^{CaCO3}_{lib.} = A_{2g}(0) + A_{2u}(IR) + E_g(R) + E_u(IR)$

Table B15: Summary for translational, librational and intramolecular irreducible representations for calcite.

Atom	A_{1g}	A_{1u}	A_{2g}	A_{2u}	E_g	E_u
Ca, transl.	0	1	0	1	0	2
CO_3,transl.	0	0	1	1	1	1
CO_3,librat.	0	0	1	1	1	1
CO_3,intramol	1	1	1	1	2	2
Acoustic	0	0	0	-1	0	-1
Glob($CaCO_3$)	1	2	3	3	4	5

Therefore, the global irreducible representation for calcite,

$$\Gamma^{CaCO3}_{global} = A_{1g}\ (R) + 2A_{1u}\ (0) + 3A_{2g}\ (0) + 3A_{2u}\ (IR) + 4E_g\ (R) + 5E_u(IR)$$

Active modes = A_{1g} (R) + $4E_g$ (R) + $3A_{2u}$ (IR) + $5E_u$ (IR)

Inactive modes = $3A_{2g}$ + $2A_{1u}$

Acoustic modes = A_{2u} + E_u

For more details see [68,80].

APPENDIX C

GRAPHS CONFIRMING THE VALIDITY OF RATE EQUATIONS.

Figure C1: Reduced-time plot for Sample A using Contracting Volume equation at 1000° C.

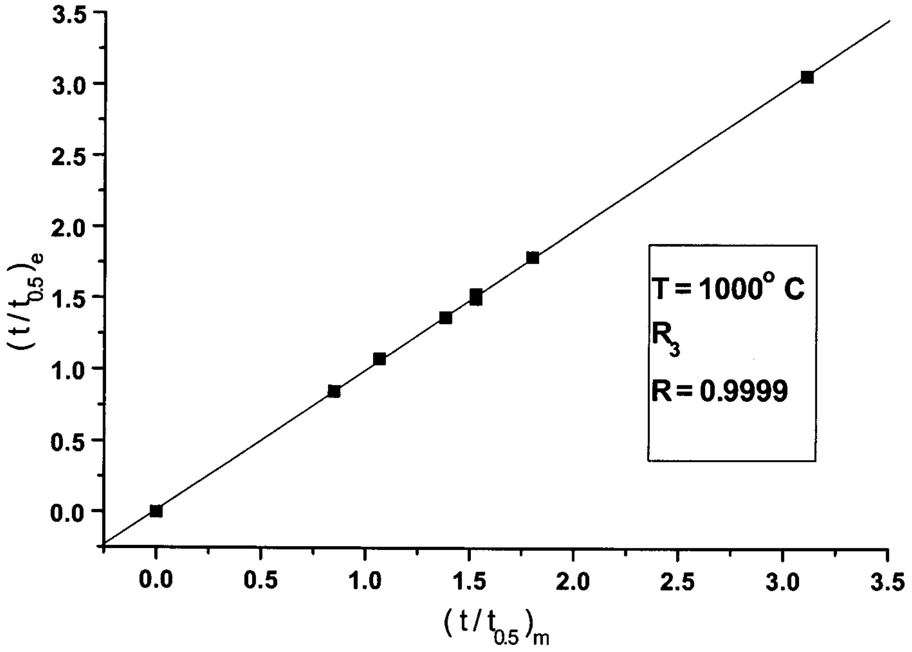

Figure C2: Reduced-time plot for Sample A using Contracting Volume equation at 950° C

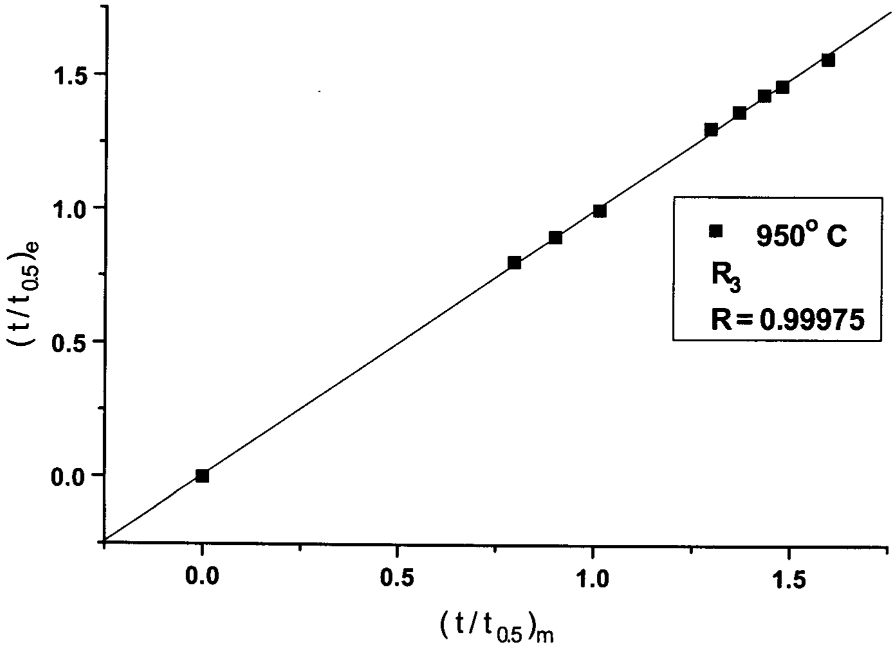

Figure C3: Reduced-time plot for Sample A using Contracting Volume equation at 900° C.

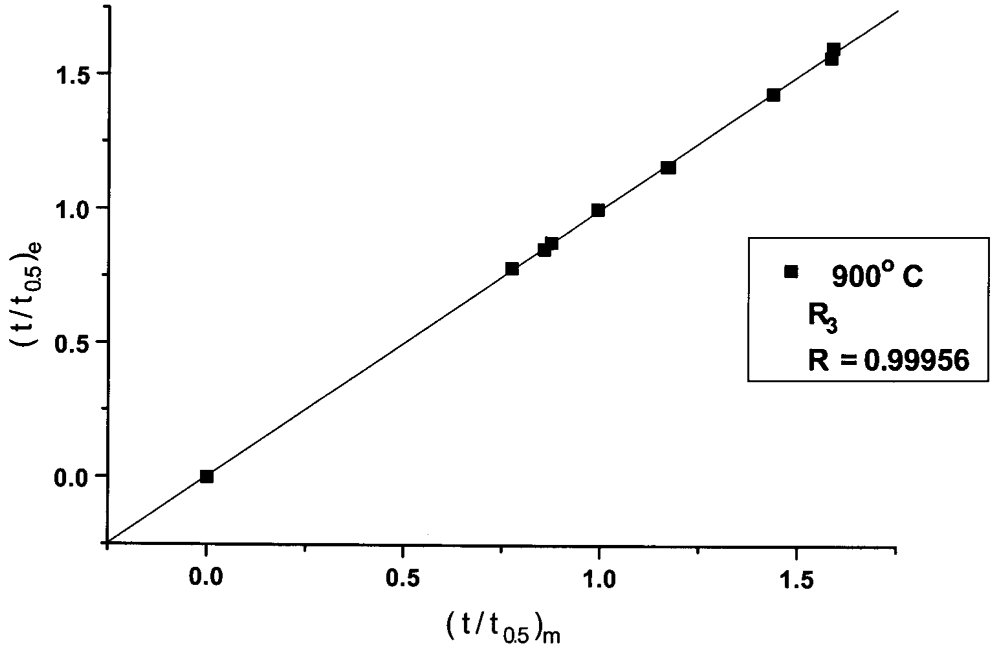

Figure C4: Reduced-time plot for Sample B using Contracting Volume equation at 1000° C.

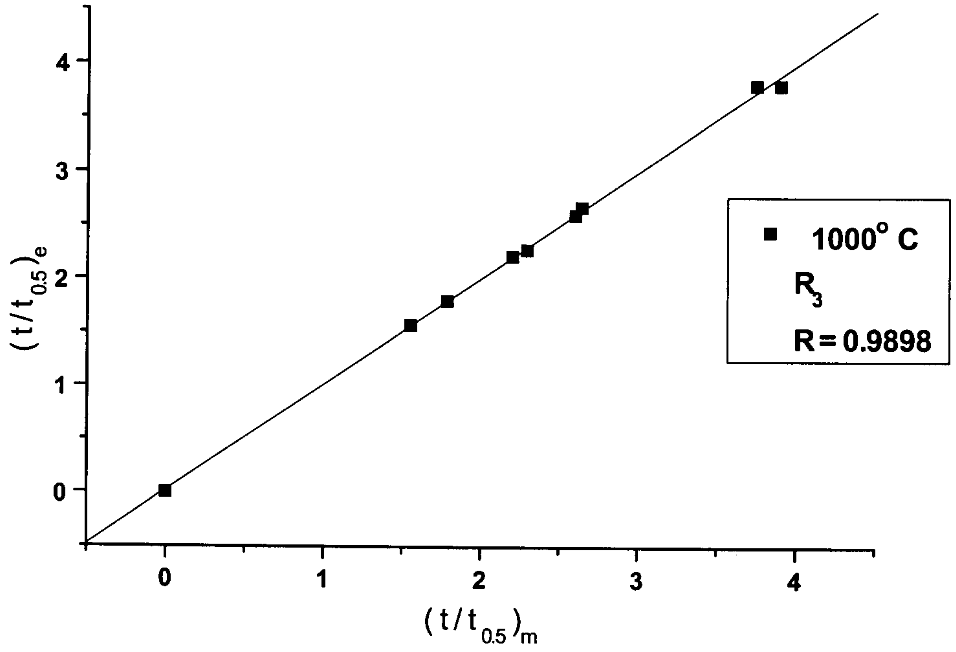

Figure C5: Reduced-time plot for Sample B using Contracting Volume equation at 950° C.

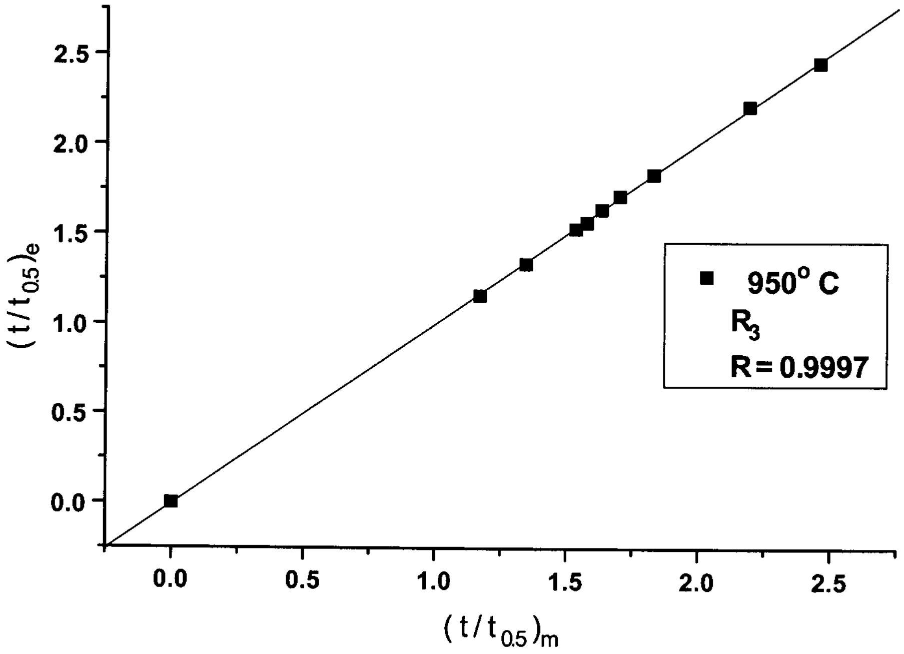

Figure C6: Reduced-time plot for Sample B using Contracting Volume equation at 900° C.

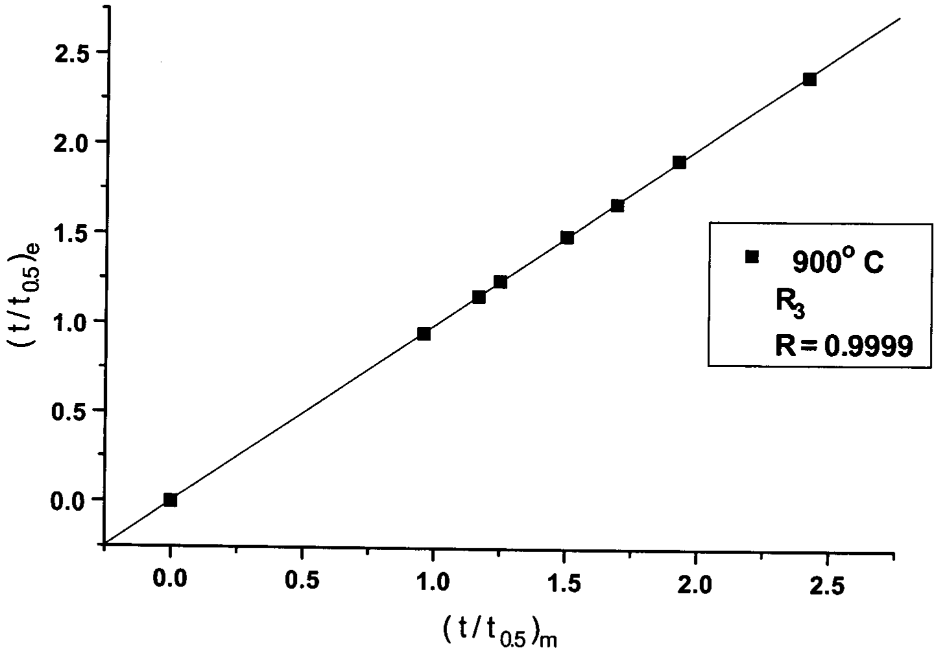

Figure C7: Reduced-time plot for Sample C using Contracting Volume equation at 1000° C.

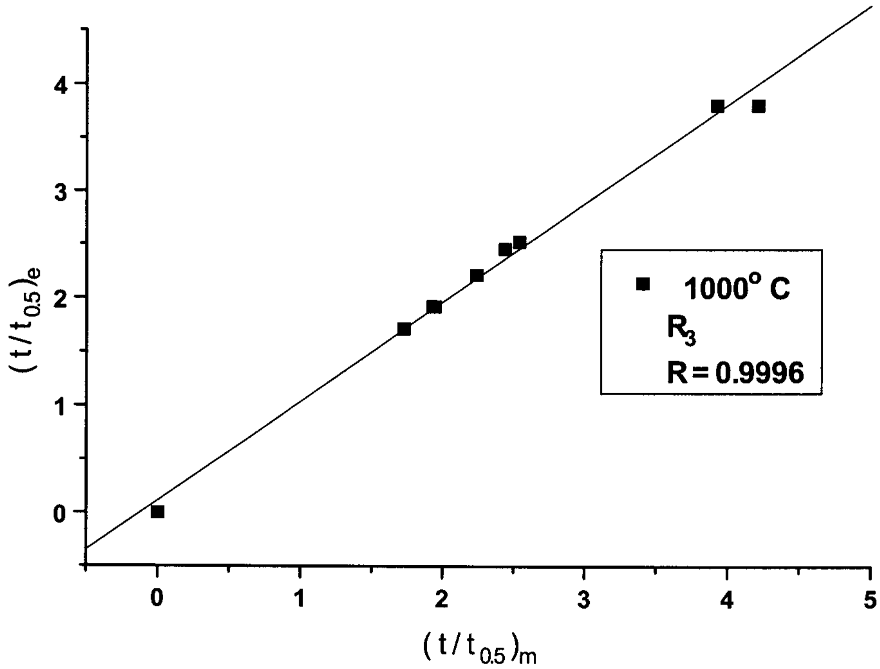

Figure C8: Reduced-time plot for Sample C using Contracting Volume equation at 950° C.

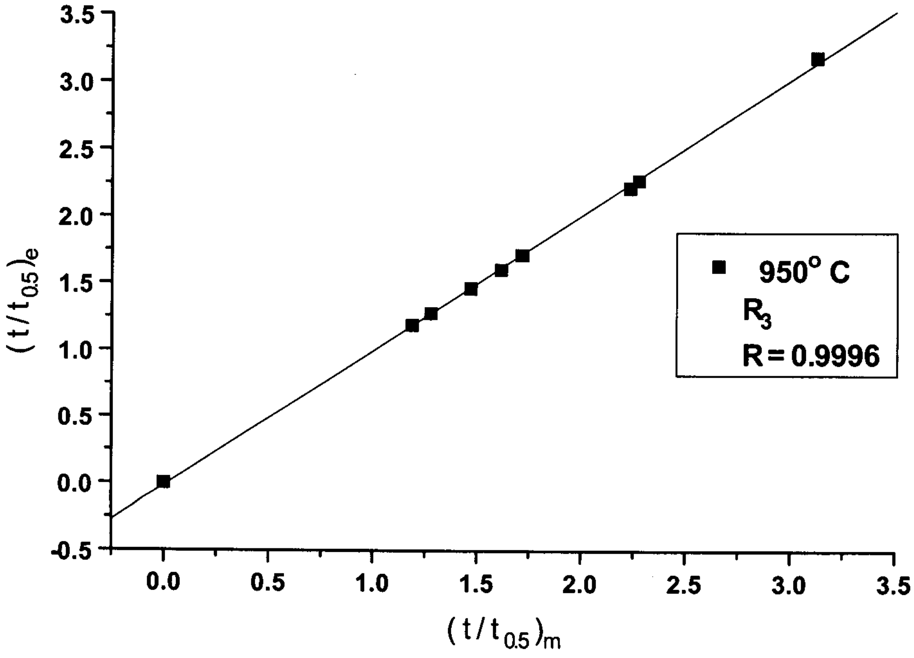

Figure C9: Reduced-time plot for Sample C using Contracting Volume equation at 900° C.

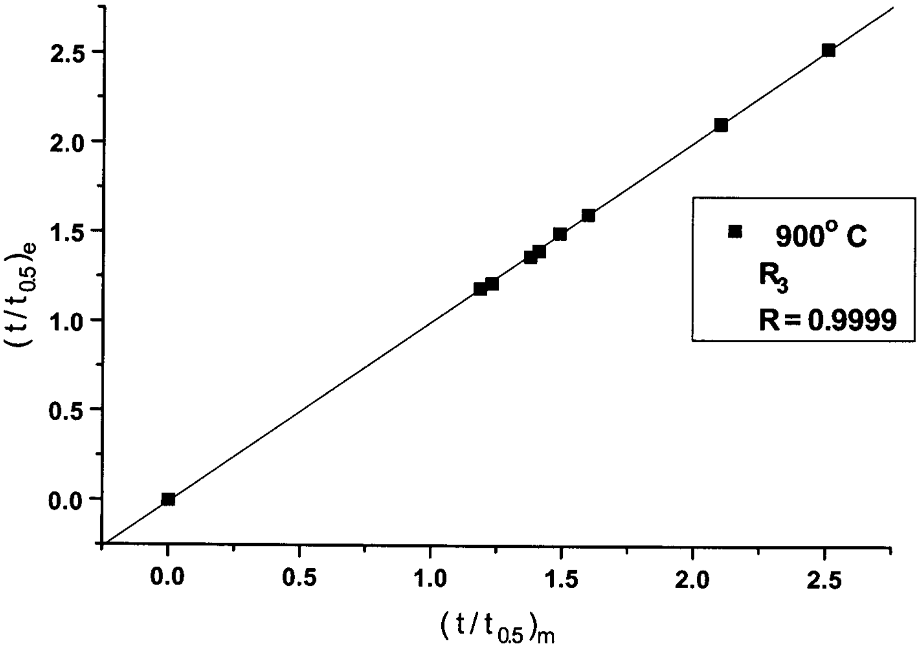

Figure C10: Reduced-time plot for Sample D using Contracting Volume equation at 1000° C.

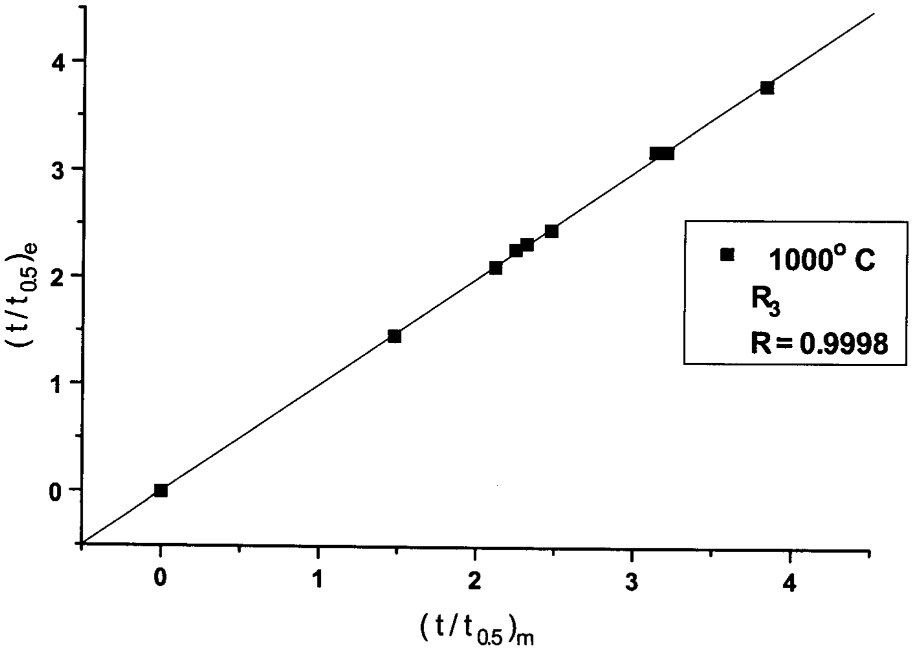

Figure C11: Reduced-time plot for Sample D using Contracting Volume equation at 950° C.

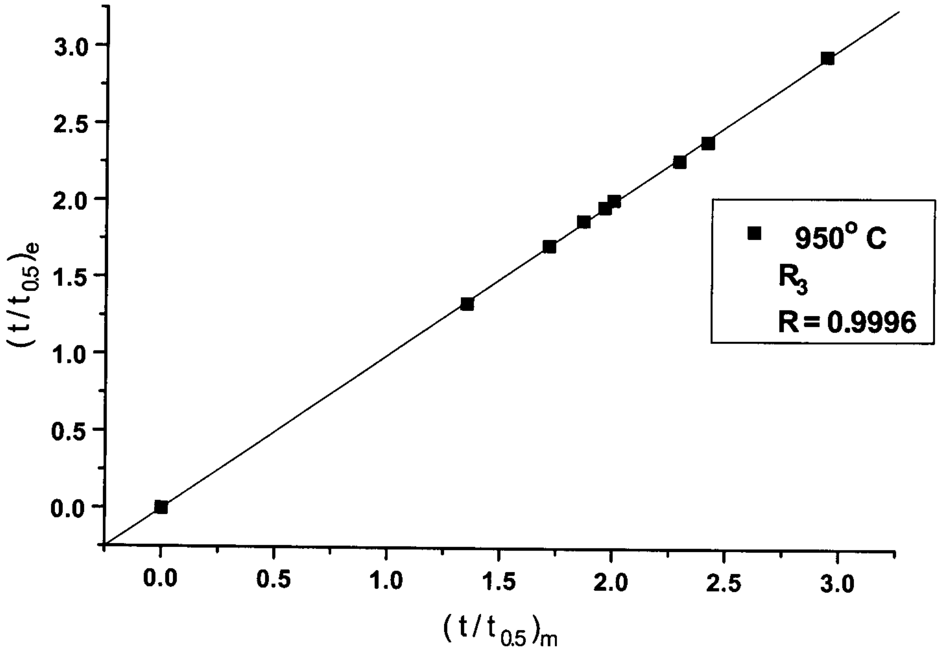

Figure C12: Reduced-time plot for Sample D using Contracting Volume equation at 900° C.

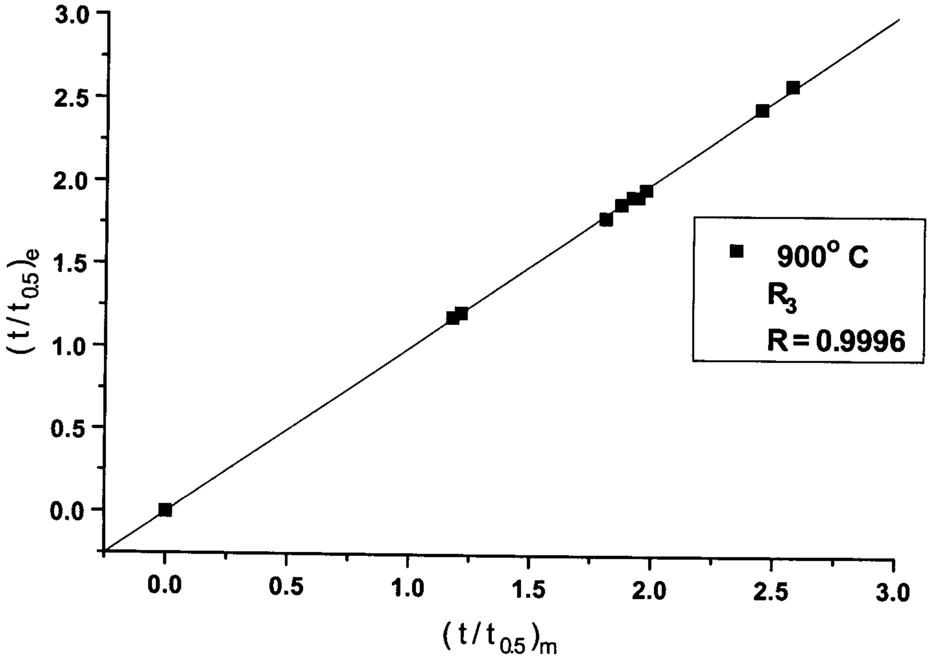

Figure C13: Reduced-time plot for Sample A using Ginstling-Brounshtein equation at 1000° C.

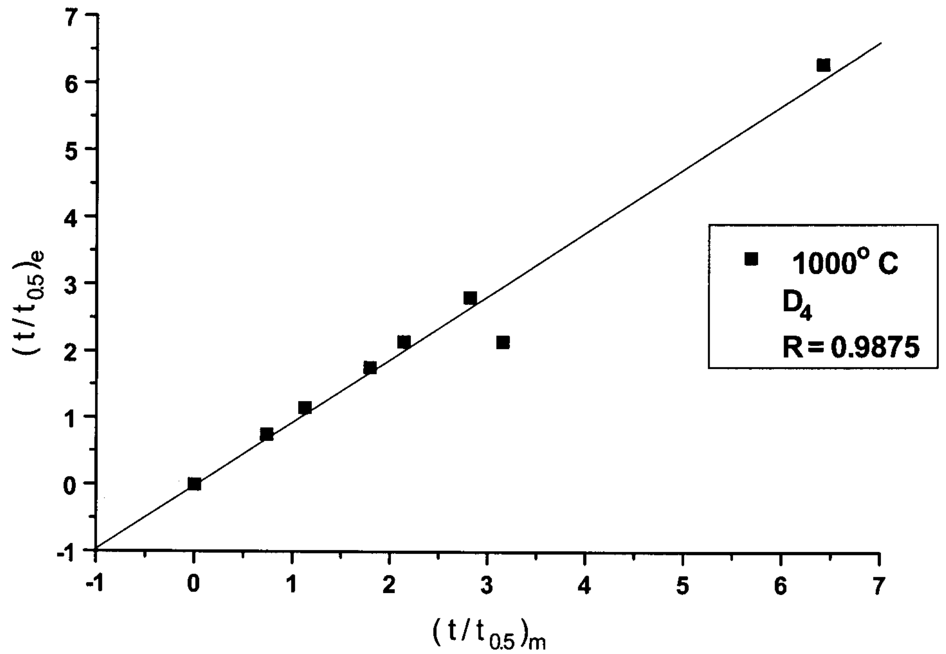

Figure C14: Reduced-time plot for Sample A using Ginstling-Brounshtein equation at 950° C.

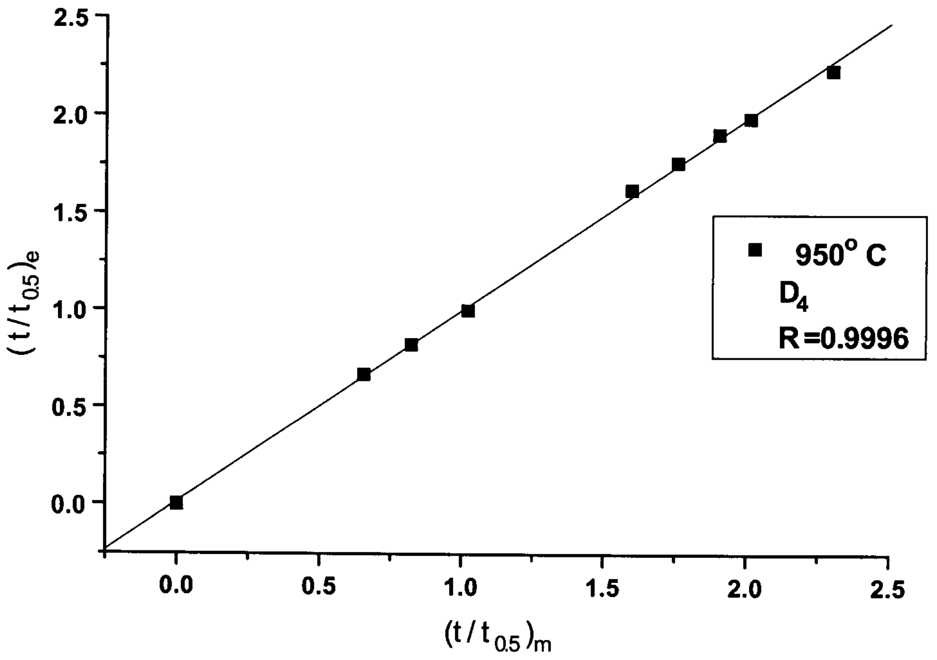

Figure C15: Reduced-time plot for Sample A using Ginstling-Brounshtein equation at 900° C.

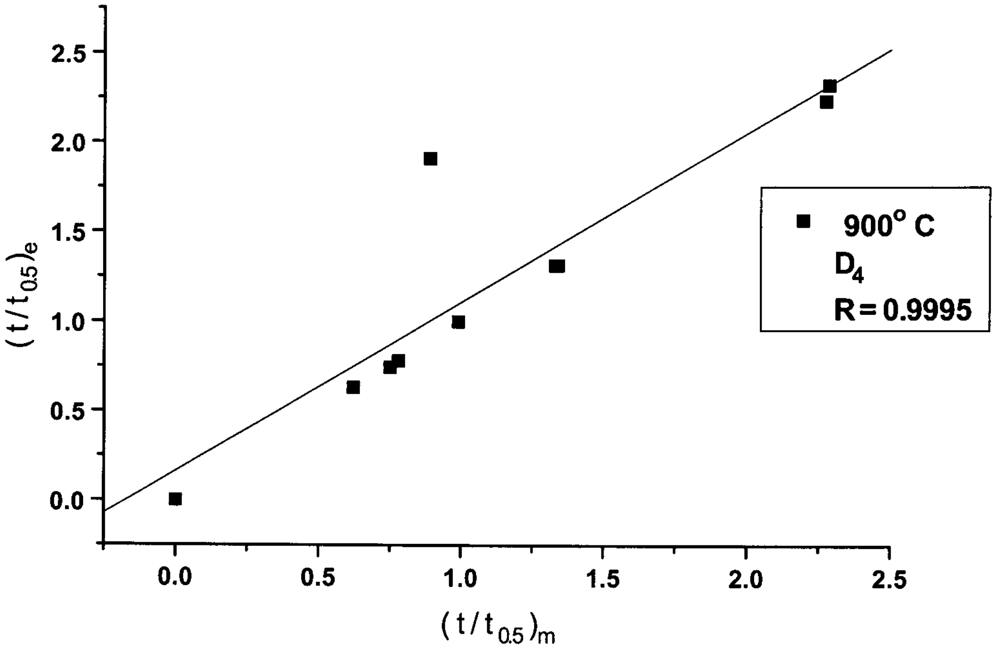

Figure C16: Reduced-time plot for Sample B using Ginstling-Brounshtein equation at 1000° C.

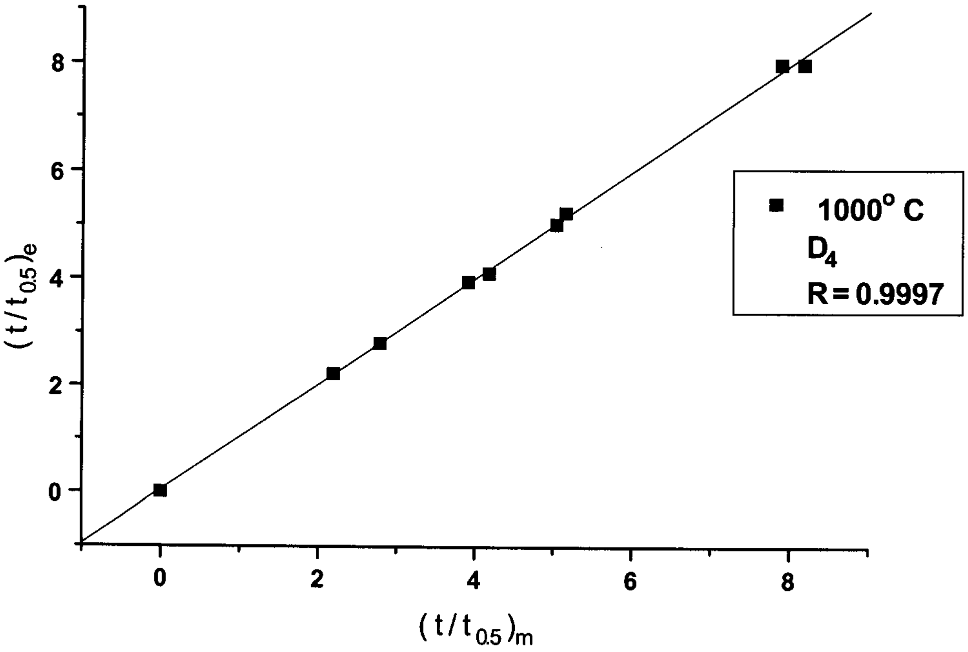

Figure C17: Reduced-time plot for Sample B using Ginstling-Brounshtein equation at 950° C.

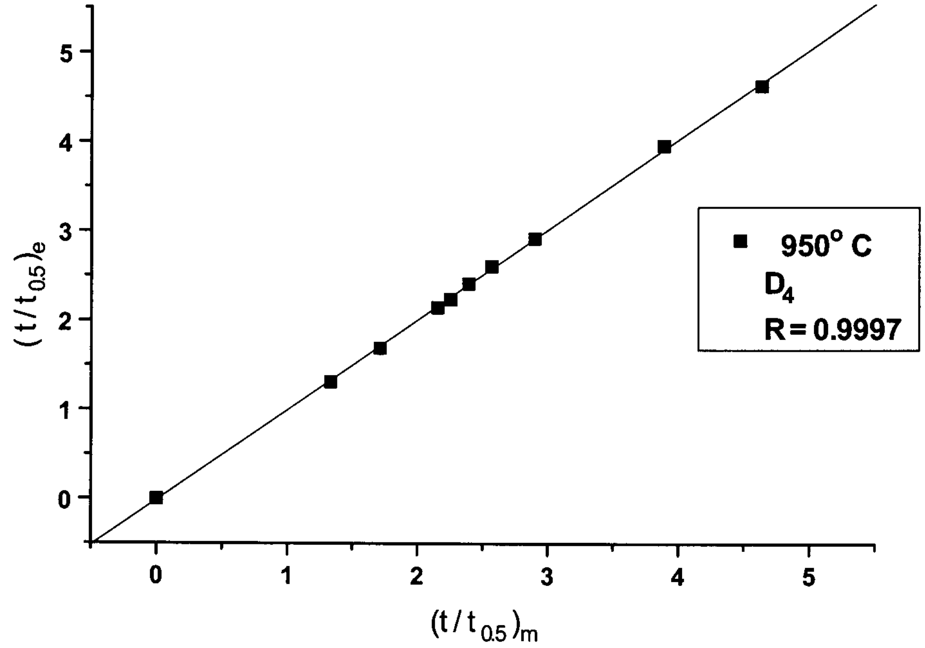

Figure C18: Reduced-time plot for Sample B using Ginstling-Brounshtein equation at 900° C.

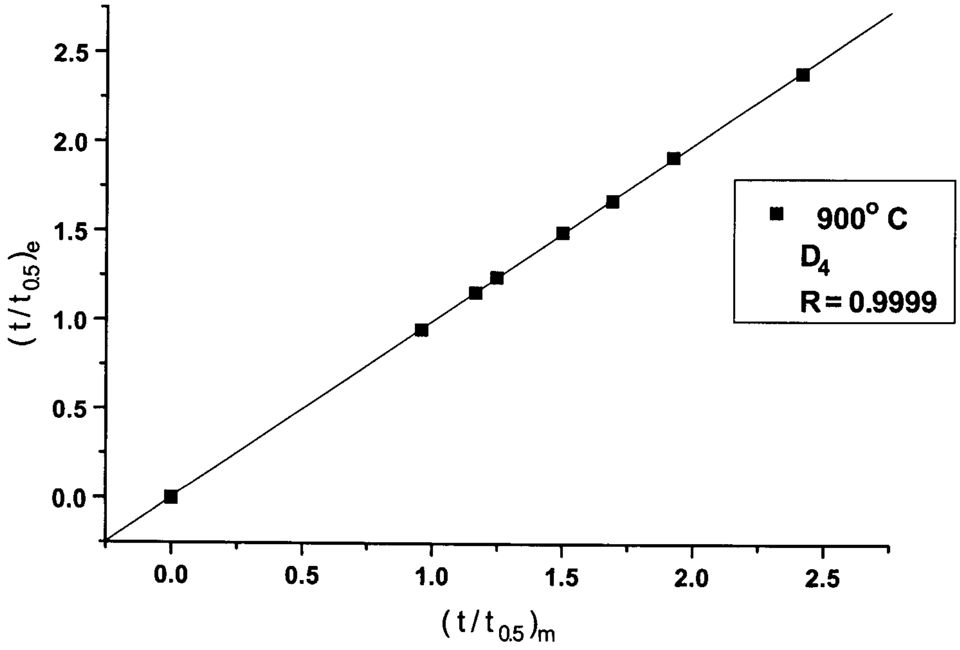

Figure C19: Reduced-time plot for Sample C using Ginstling-Brounshtein equation at 1000° C.

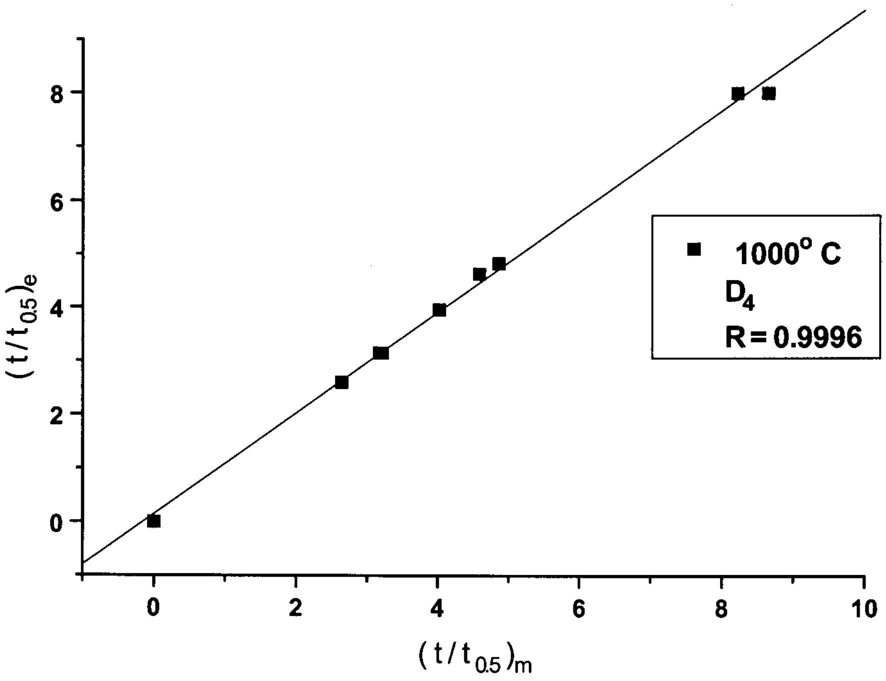

Figure C20: Reduced-time plot for Sample C using Ginstling-Brounshtein equation at 950° C.

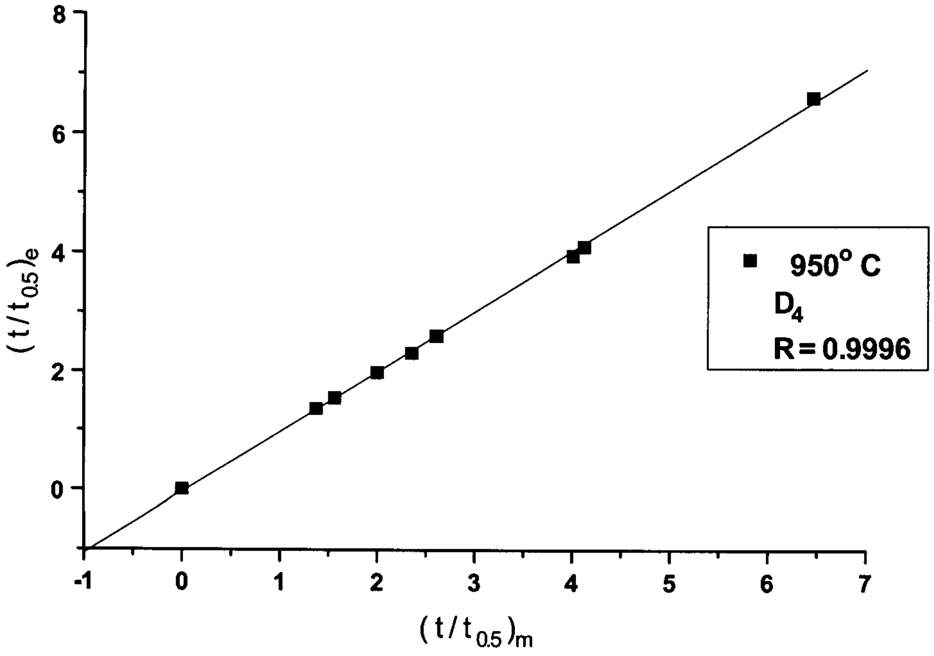

Figure C21: Reduced-time plot for Sample C using Ginstling-Brounshtein equation at 900° C.

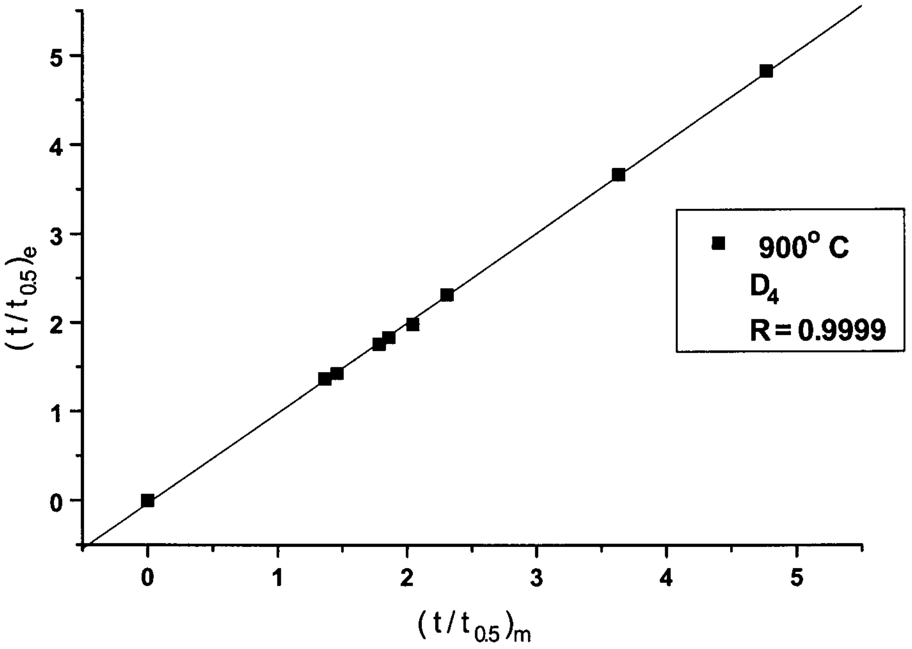

Figure C22: Reduced-time plot for Sample D using Ginstling-Brounshtein equation at 1000° C.

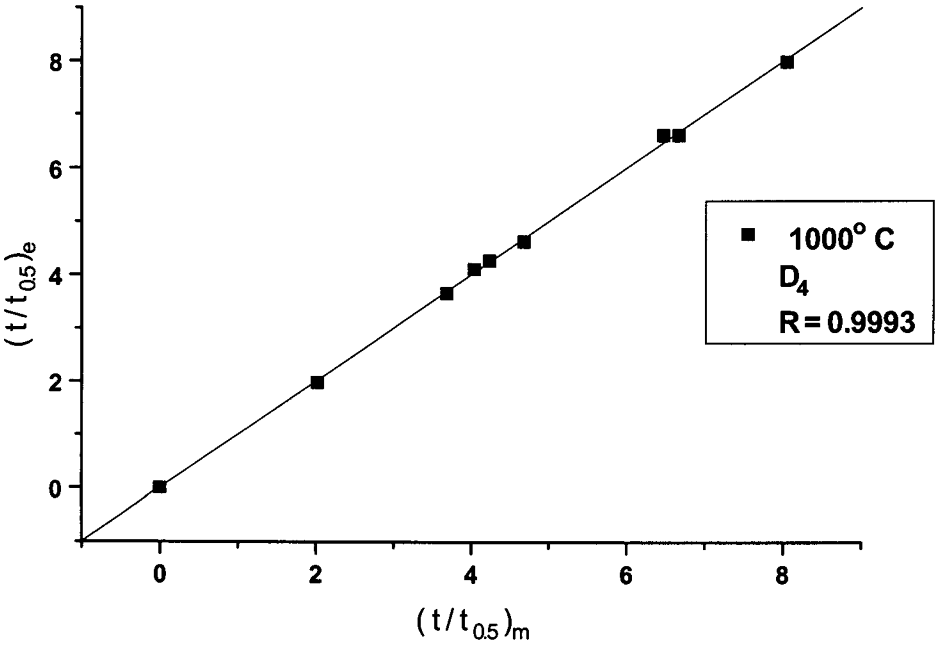

Figure C23: Reduced-time plot for Sample D using Ginstling-Brounshtein equation at 950° C.

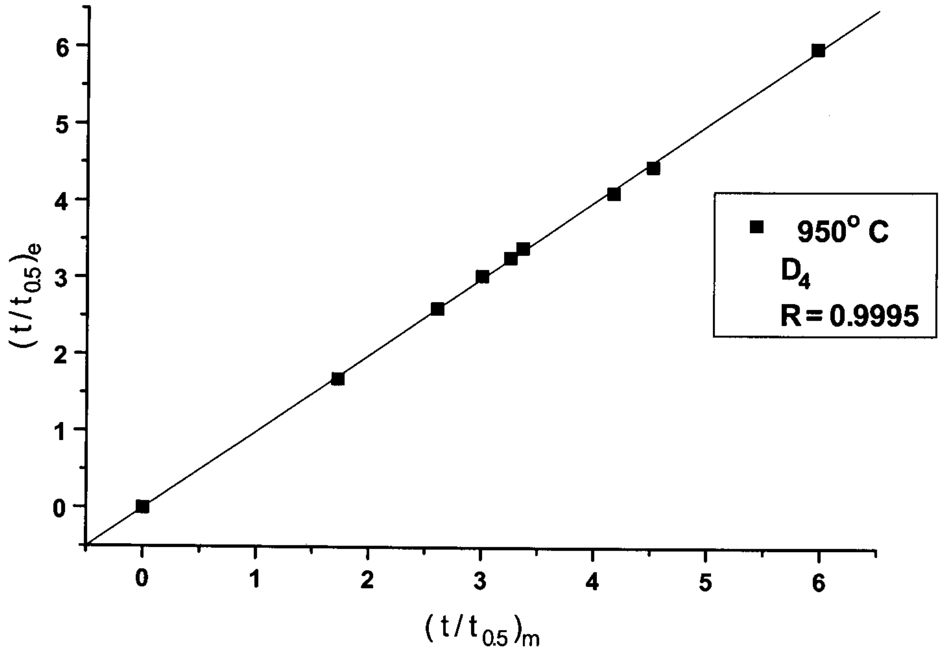

Figure C24: Reduced-time plot for Sample D using Ginstling-Brounshtein equation at 900° C.

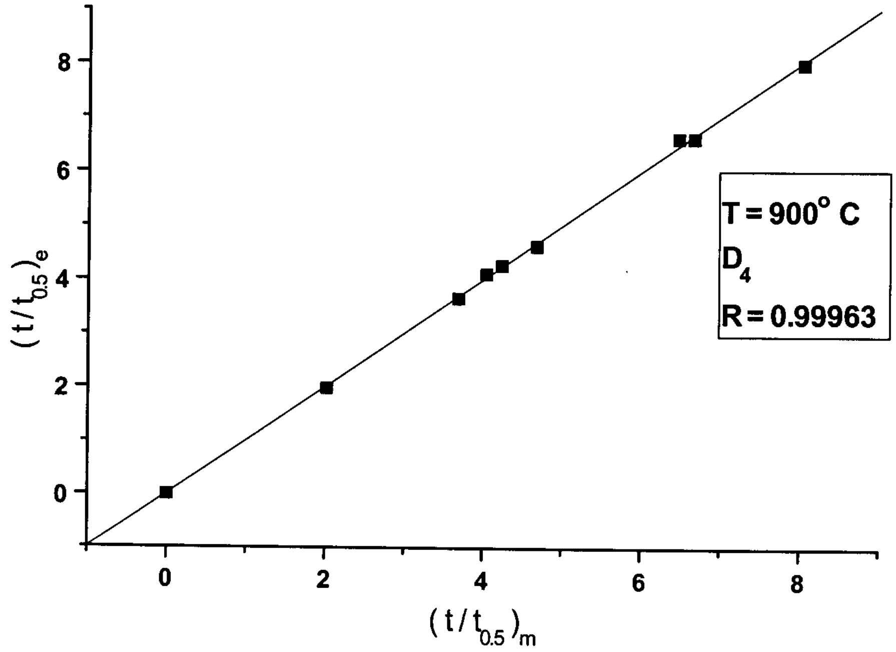

APPENDIX D (CHAPTER 3)

DATA FROM THE FT-IR MEASUREMENTS

Table D1: Data for isothermal plot of Sample A (3 - 4 g) at 1000° C.
I_0 = 0.7328.

t / s	I	I / I_0
0	0.7328	1
15	0.4116	0.5616
30	0.2357	0.3216
45	0.3480	0.4749
60	0.2354	0.3212
75	0.1827	0.2492
90	0.1197	0.1633

Table D2: Data for isothermal plot of Sample A (3 - 4 g) at 950° C.
I_0 = 0.7328.

t / s	I	I / I_0
0	0.7328	1
30	0.3630	0.4954
60	0.3604	0.4918
90	0.4281	0.5841
120	0.2716	0.3706
150	0.2469	0.3368
180	0.2889	0.4974
210	0.2267	0.3093
240	0.2572	0.3509

Table D3: Data for isothermal plot of Sample A (3 - 4 g) at 900° C.
I_0 = 0.7328.

t / s	I	I / I_0
0	0.7328	1
120	0.4350	0.5936
240	0.4091	0.5582
360	0.3686	0.5029
480	0.3204	0.4372
600	0.3497	0.4772
720	0.2489	0.3395
840	0.2240	0.3057
960	0.2229	0.3042

Table D4: Data for isothermal plot of Sample B (5 - 6 g) at 1000° C.
I_0 = 0.8285.

t / s	I	I / I_0
0	0.8285	1
60	0.2606	0.3146
120	0.0829	0.1000
180	0.2093	0.2526
240	0.1215	0.1467
300	0.1354	0.1634
360	0.0784	0.0946
420	0.0099	0.0119
480	0.0063	0.0076

Table D5: Data for isothermal plot of Sample B (5 - 6 g) at 950° C.
I_0 = 0.8285.

t / s	I	I / I_0
0	0.8285	1
120	0.3624	0.4374
240	0.2552	0.3080
360	0.3128	0.3776
480	0.2003	0.2417
600	0.2270	0.2740
720	0.2423	0.2924
840	0.2649	0.3197
960	0.1366	0.1648
1080	0.0995	0.1201

Table D6: Data for isothermal plot of Sample B (5 - 6 g) at 900° C.
I_0 = 0.8285.

t / s	I	I / I_0
0	0.8285	1
240	0.4285	0.5172
480	0.4590	0.4384
720	0.3396	0.4099
960	0.2292	0.2766
1200	0.4115	0.3300
1440	0.2640	0.3186
1680	0.1878	0.2198

Table D7: Data for isothermal plot of Sample C (30 - 40 g) at 1000° C.
I_0 = 0.9374.

t / s	I	I / I_0
0	0.9374	1
300	0.2502	0.2669
600	0.2045	0.2181
900	0.1151	0.1228
1200	0.1465	0.1563
1500	0.2017	0.2151
1800	0.1014	0.1082
2100	0.0065	0.0069
2400	0.0021	0.0023

Table D8: Data for isothermal plot of Sample C (30 - 40 g) at 950° C.
I_0 = 0.9374.

t / s	I	I / I_0
0	0.9374	1
600	0.3743	0.3993
1200	0.4033	0.4302
1800	0.3173	0.3384
2400	0.2534	0.2703
3000	0.1403	0.1496
3600	0.2784	0.2970
4200	0.2527	0.2696
4800	0.1469	0.1568
5400	0.0422	0.0450

Table D9: Data for isothermal plot of Sample C (30 - 40 g) at 900° C. I_0 = 0.9374.

t / s	I	I / I_0
0	0.9374	1
900	0.3440	0.3670
1800	0.4038	0.4308
2400	0.3894	0.4154
3420	0.2827	0.3016
3780	0.3345	0.3568
4500	0.3120	0.3328
5400	0.1708	0.1822
6300	0.1057	0.1128

Table D10: Data for isothermal plot of Sample D (90 - 110 g) at 1000° C. I_0 = 1.1877.

t / s	I	I / I_0
0	1.1877	1
360	0.3909	0.3291
720	0.1695	0.1427
1080	0.1399	0.1178
1440	0.0528	0.0445
1800	0.1838	0.1548
2160	0.2122	0.1787
2520	0.0111	0.0094
2880	0.0462	0.0389

Table D11: Data for isotherm plot of Sample D (90 - 110 g) at 950° C. $I_0 = 1.1877$.

t / s	I	I / I_0
0	1.1877	1
360	0.4459	0.3754
1080	0.3205	0.2699
1800	0.2763	0.2326
2520	0.2409	0.2029
3240	0.2509	0.2112
3960	0.1744	0.1468
4680	0.1504	0.1266
5400	0.0727	0.0612

Table D12: Data for isotherm plot of Sample D (90 - 110 g) at 900° C. $I_0 = 1.1877$.

t / s	I	I / I_0
0	1.1877	1
600	0.5151	0.4337
1200	0.5011	0.4219
2400	0.2751	0.2316
3600	0.2564	0.2159
4800	0.2627	0.2212
6000	0.2932	0.2469
7200	0.2481	0.2089
8400	0.1233	0.1038
9600	0.1447	0.1218

Table D13: The obedience of Sample A (5 - 6 g) data to Contracting Volume at 1000° C, 950° C and 900° C. The values of R_3 (α) are given in the table below. $\alpha = (1 - I / I_o)$.

$R_3(\alpha) = 1 - (1 - \alpha)^{1/3}$			
t / s	**1000° C**	**950° C**	**900° C**
0	0	0	0
15	0.175	-	-
30	0.3148	0.2088	-
45	0.2198	-	-
60	0.3152	0.1856	-
75	0.3707	-	-
90	0.4534	0.1640	-
120		0.2817	0.1596
150		0.3047	-
180		0.2668	-
210		0.3281	-
240		0.2946	0.1766
360			0.2048
480			0.2410
600			0.1934
720			0.3024
840			0.3264
960			0.3275

Table D14: The obedience of Sample A (5 - 6 g) data to Ginstling-Brounshtein model at 1000° C, 950° C and 900° C. The values of D_4 (α) are given in the table below. $\alpha = 1 - I / I_o$.

$D_4(\alpha) = 1 - (2\alpha / 3) - (1 - \alpha)^{2/3}$			
t / s	**1000° C**	**950° C**	**900° C**
0	0	0	0
15	0.0270	-	-
30	0.0783	0.0375	-
45	0.0412	-	-
60	0.1156	0.0302	-
75	0.1035	-	-
90	0.1434	0.0240	-
120		0.0645	0.0228
150		0.0738	-
180		0.0586	-
210		0.0822	-
240		0.0698	0.0275
360			0.0362
480			0.0488
600			0.0326
720			0.0730
840			0.0834
960			0.0838

Table D15: The obedience of Sample B (5 - 6 g) data to Contracting Volume model at 1000° C, 950° C and 900° C. The values of R_3 (α) are given in the table below. $\alpha = (1 - I / I_o)$.

$R_3 (\alpha) = 1 - (1 - \alpha)^{1/3}$			
t / s	**1000° C**	**950° C**	**900° C**
0	0	0	0
60	0.3199	-	-
120	0.5354	0.2409	-
180	0.3678	-	-
240	0.4726	0.3247	0.1973
300	0.4533	-	-
360	0.5444	0.2772	-
420	0.7720	-	-
480	0.8032	0.3770	0.2403
600		0.3505	-
720		0.3363	0.2572
840		0.3162	-
960		0.4517	0.3484
1080		0.5066	-
1200			0.3090
1440			0.3170
1680			0.3965

Table D16: The obedience of Sample B (5 - 6 g) data to Ginstling-Brounshtein model at 1000° C, 950° C and 900° C. The values of D_4 (α) are given in the table below. $\alpha = 1 - I / I_o$.

$D_4(\alpha) = 1 - (2\alpha / 3) - (1 - \alpha)^{2/3}$			
t / s	**1000° C**	**950° C**	**900° C**
0	0	0	0
60	0.0805	-	-
120	0.1846	0.0487	-
180	0.1021	-	-
240	0.1530	0.0826	0.0338
300	0.1434	-	-
360	0.1888	0.0626	-
420	0.2892	-	-
480	0.2997	0.1064	0.0485
600		0.0941	-
720		0.0877	0.0548
840		0.0789	-
960		0.1426	0.0932
1080		0.1700	-
1200			0.0758
1440			0.0792
1680			0.1156

Table D17: The obedience of Sample C (30 - 40 g) data to Contracting Volume model at 1000° C, 950° C and 900° C. The values of R_3 (α) are given in the table below. $\alpha = (1 - I / I_o)$.

$R_3(\alpha) = 1 - (1 - \alpha)^{1/3}$			
t / s	**1000° C**	**950° C**	**900° C**
0	0	0	0
300	0.3562	-	-
600	0.3980	0.2636	-
900	0.5030	-	0.2840
1200	0.4613	0.2450	-
1500	0.4008	-	-
1800	0.5235	0.3031	0.2447
2100	0.8094	-	-
2400	0.8682	0.3534	0.2538
2700		-	-
3000		0.4691	-
3420		-	0.3294
3600		0.3328	-
3780		-	0.2907
4200		0.3540	-
4500		-	0.3070
4800		0.4608	-
5400		0.6443	0.4330
6300		-	0.5168

Table D18: The obedience of Sample C (30 - 40 g) data to Ginstling-Brounshtein model at 1000° C, 950° C and 900° C. The values of D_4 (α) are given in the table below. $\alpha = 1 - I / I_o$.

$D_4(\alpha) = 1 - (2\alpha / 3) - (1 - \alpha)^{2/3}$			
t / s	**1000° C**	**950° C**	**900° C**
0	0	0	0
300	0.0967	-	-
600	0.1164	0.0572	-
900	0.1682	-	0.0654
1200	0.1474	0.0502	-
1500	0.1177	-	-
1800	0.1784	0.0733	0.0501
2100	0.3016	-	-
2400	0.3174	0.0954	0.0535
2700		-	-
3000		0.1512	-
3420		-	0.0846
3600		0.0862	-
3780		-	0.0681
4200		0.0957	-
4500		-	0.0750
4800		0.1470	-
5400		0.2368	0.1334
6300		-	0.1750

Table D19: The obedience of Sample D (90 - 110 g) data to Contracting Volume model at 1000° C, 950° C and 900° C. The values of R_3 (α) are given in the table below. $\alpha = (1 - I / I_o)$.

$R_3(\alpha) = 1 - (1 - \alpha)^{1/3}$			
t / s	**1000° C**	**950° C**	**900° C**
0	0	0	0
360	0.3046	0.2786	-
600	-	-	0.2431
720	0.4774	-	-
1080	0.5098	0.3537	-
1200	-	-	0.2500
1440	0.6456	-	-
1800	0.4631	0.3850-	-
2160	0.4367	-	-
2400	-	-	0.3859
2520	0.7893	0.4124	-
2880	0.6612	-	-
3240		0.4044	-
3600		-	0.4000
3960		0.4724	-
4680		0.4978	-
4800		-	0.3952
5400		0.6059	-
6000			0.3726
7200			0.4066
8400			0.5300
9600			0.5043

Table D20: The obedience of Sample D (90 - 110 g) data to Ginstling-Brounshtein model at 1000° C, 950134° C and 900° C. The values of D_4 (α) are given in the table below. $\alpha = 1 - I / I_o$.

$D_4(\alpha) = 1 - (2\alpha / 3) - (1 - \alpha)^{2/3}$			
t / s	**1000° C**	**950° C**	**900° C**
0	0	0	0
360	0.0740	0.0632	-
600	-	-	0.0494
720	0.1554	-	-
1080	0.1716	0.0956	-
1200	-	-	0.0520
1440	0.2374	-	-
1800	0.1482	0.1102	-
2160	0.1352	-	-
2400	-	-	0.1106
2520	0.2952	0.1234	-
2880	0.2445	-	-
3240		0.1194	-
3600		-	0.1173
3960		0.1529	-
4680		0.1656	-
4800		-	0.1150
5400		0.2188	-
6000			0.1044
7200			0.1206
8400			0.1816
9600			0.1688

LIST OF TABLES

Table D7	Data for isothermal plot of Sample C (30 - 40 g) at 1000° C. $I_0 = 0.9374$.
Table D8	Data for isothermal plot of Sample C (30 - 40 g) at 950° C. $I_0 = 0.9374$.
Table D9	Data for isothermal plot of Sample C (30 - 40 g) at 900° C. $I_0 = 0.9374$.
Table D10	Data for isothermal plot of Sample D (90 - 110 g) at 1000° C. $I_0 = 1.1877$.
Table D11	Data for isothermal plot of Sample D (30 - 40 g) at 950° C. $I_0 = 1.1877$.
Table D12	Data for isothermal plot of Sample D (90 - 110 g) at 900° C. $I_0 = 1.1877$.
Table D13	The obedience of Sample A (3 - 4 g) data to Contracting Volume at 1000° C, 950° C and 900° C.
Table D14	The obedience of Sample A (3 - 4 g) data to Ginstling-Brounshtein at 1000° C, 950° C and 900° C.
Table D15	The obedience of Sample B (5 - 6 g) data to Contracting Volume at 1000° C, 950° C and 900° C.
Table D16	The obedience of Sample B (5 - 6 g) data to Ginstling-Brounshtein Volume at 1000° C, 950° C and 900° C.
Table D17	The obedience of Sample C (30 - 40 g) data to Contracting Volume at 1000° C, 950° C and 900° C.

Table D18 The obedience of Sample C (30 - 40 g) data to Ginstling-Brounshtein Volume at 1000° C, 950° C and 900° C.

Table D19 The obedience of Sample D (90 - 110 g) data to Contracting Volume at 1000° C, 950° C and 900° C.

Table D20 The obedience of Sample D (90 - 110 g) data to Ginstling-Brounshtein Volume at 1000° C, 950° C and 900° C.

LIST OF FIGURES

REFERENCES

1. C. Guler, D. Dollimore and G. R. Heal, Thermochimica Acta, **54**, 187 (1982)

2. G. A. Norton and J. F. McClelland, Miner. Eng., **10** (2), 237 (1997).

3. O. A. Salman and N.Khraishi, Solar Energy, **41**(4), 305 (1988).

4. C. A. and J. H. Potgieter, 1997, An Investigation into the Chemical nature of the reactivity of lime , Cement Conference. Proceedings of the 10th International Chemistry of Cement Conference, Gothenburg, Sweden, June 1997, paper 2ii049.

5. D. L. Hudson-Lamb, 1997, The thermal decomposition reactions of gypsum, lime and limestone compounds, University of Pretoria, Chemistry, PhD 25.

6. D. G. Billing, July 1998, Analysis of limestone and lime by Rietveld methods, SACI Convention, Abstract n.

7. A. G. Xyla and P. G. Koutsoukos, J. Chem. Soc. Far. Trans. I, **85**(10), 3165 (1989).

8. E. Hakanen and J. Koskikallio, Finn. Chem. Lett., **Iss.3-4**, 34 (1982).

9. H. Lowenstam, Am. Miner., **47**, 700 (1962).

10. H. Alder and P. F. Kerr, Amer. Miner., **55**, 284 (1970).

11. The Handbook of Infrared and Raman Spectra of Inorganic compounds and Organic Salts, R. A. Nyquist, R. O. Kagel, C. L. Putzig and M. A. Leugers, vol. **3** p.56, vol.**4** p.78 - 79,1997.

12. S. D. Ross, Inorganic Infrared and Raman Spectra, McGraw-Hill, London, 1972.

13. A. G. Xyla and P. G. Koutsoukos, Proc. J. Gastock '88 Conference Versailes France.

14. W. D. Bischoff, S. K. Sharma and F. T. Mackenzie, Amer. Mineralogist, **70**, 581 (1985).

15. H. Chang and J. Huang , Anal. Chem., **69**(no.8), 1486 (1997)

16. C. H. Bamford and C. F. H. Tipper, Chemical Kinetics : Reactions in Solid State, 22 (1980).

17. R. C. Mackenzie, Talanta, **16**, 1227 (1969).

18. P. D. Garn, Thermoanalytical Methods of investigation, Academic Press, New York (1965).

19. W. E. Garner, Chemistry of the Solid State, Ed., Butterworth, London (1965) Chapter 7.

20. J. Sestak, V. Satavo and W. W. Wendlandt , Thermochim. Acta, **7**, 33 (1973) 33.

21. J. M. Criado and J. Morales, Thermochim. Acta, **19**, 305 (1977).

22. J. W. Christian, Transformations in Metals and Alloys, 1 (1975).

23. P. W. M. Jacobs, Material Science Research, **4**, 37 (1969).

24. A. L. Draper and L. K. Sveum, Thermochim. Acta., **1**, 345 (1970).

25. P. D. Garn, J. Therm. Anal., **13**, 581 (1978).

26. F. Acke and I. Panas, Thermochim. Acta, **306**, 73 (1997).

27. S. J. Gregg and R. I. Razouk, J. Chem. Soc., 536 (1949).

28. D. Price, N. Fatemi, D. Dollimore and R. Whitehead, Thermochim. Acta, **94**, 313 (1985).

29. M. Maciejewski and H. R. Oswald, Thermochim. Acta, **85**, 39 (1985).

30. A. W. D. Hills, Chem. Eng. Sci., **23**, 297 (1968).

31. P. D. Garn, J. Therm. Anal., **13**, 581 (1978).

32. M. J. Saavedra, C. Parada and E. J. Baran, J. Phys. Chem., **57** (12) 1929 (1996).

33. J. Hlavay and J. Inczedy, Spectrochimica Acta, **41A** (6), 783 (1985).

34. Van de Mass, Miller, Laboratory Methods in vibrational spectroscopy, Third Edition, Chapter 8.

35. M. D. Krahling and R. Eliason, J. Chem. Educ. **62** (10), 886 (1985).

36. L. L. Tyson, Y. Ling and C. K. Mann, Appl. Spec., **38**, 663 (1984).

37 E. Hakanen and J. Koskikallio, Finn. Chem. Lett., **Iss.3-4**, 34 (1982).

38. C.J. Keattch and D. Dollimore, An introduction to thermogravimetry, Heyden, London (1975).

39. K. L. Mampel, Z. Physichem. A. 187, **43**, 235 (1940).

40. W. Jander, Z. Anorg. Allg. Shem., **163**, 1 (1927).

41. E. G. Prout and F. C. Tompkins, Trans. Faraday Soc., **42**, 482 (1946).

42. B. V. Erofeev, C. R. Acad. Sci.,URSS., **52**, 511 (1946).

43. M. Avrami, J. Chem. Phys., **9**, 177 (1941).

44. W. D. Spencer and B. Topley, J. Chem. Soc., 2633 (1929).

45. W. O. George and P. S. McIntyne, Infrared Spectroscopy. Wiley. Chichester, (1987).

46. J. B. Holt, J. B. Cutler and M. E. Wadsworth, J. Amer. Ceram. Soc., **45**, 133 (1962).

47. R. S. Halford, J. Chem. Phys., **14**, 8 (1946).

48. H. Winston and R. S. Halford, J. Chem. Phys., **17**, 607 (1949).

49. J. H. Sharp, G. W. Brindley and B. N. N. Achar, J. Amer. Ceram. Soc., **49** (7), 379 (1966).

50. L. F. Jones and D. Dollimore, Thermochim. Acta, **13**, 240 (1975).

51. A. M. Ginstling and B. I. Brounshtein, Zh. Prikl. Khim., **23**, 124 (1950).

52. J. P. Elder and V. B. Reddy, J. Thermal Anal., **31**, 395 (1986).

53. P. K. Gallagher and D. W. Johnson, Jr., Thermochim. Acta, **14**, 255 (1976).

54. P. K. Gallager and D. W. Johnson, Jr., Thermochim. Acta, **6**, 67 (1973).

55. H. T. S. Britton, S. J. Gregg and G. W. Winsor, Trans. Far. Soc., **48**, 63 (1952).

56. D. Beruto and A. W. Searcy, J. Chem. Soc., Far. Trans. I, **70**, 2145 (1974).

57. M. D. Judd and M. I. Pope, J. Thermal Anal., **4**, 31 (1972).

58. J. Zsako' and H. E. Arz, J. Thermal Anal., **6**, 651 (1974).

59. A. M. Ginstling and B. I. Brounshtein, J. Appl. Chem., USSR, **23**, 1327 (1950).

60. P. D. Garn, J. Thermal Anal., **10**, 99 (1976).

61. J. Zsako', J. Thermal Anal., **9**, 101 (1976).

62. T. R. Ingram and P. Marier, Canad. J. Chem. Eng., **41**, 179 (1963).

63. K. N. Ninan, K. Krishman and V. N. Krishnamurthy, J. Thermal Anal., **37**, 1533 (1991).

64. J. Khinast, G.F. Krammer, Ch. Brunner and G.Staudinger, Chem. Eng. Sci., **51**, 623 (1996).

65. J. D. Hancock and H. Sharp, J. Amer. Cer. Society, **55**(2), 74 (1972).

66. W. Sterzel and E. Chorinsky, Spectrochim. Acta, **24A**, 353 (1968).

67. J. A. Goldsmith and S. D. Ross, Spectrochim. Acta, **23A**, 1909 (1967).

68. W. B. White. 1974. The carbonate minerals. In : V. C. Farmer , " The infrared spectra of Minerals " London : Mineralogical Society, 227 - 284.

69. J. T. Lee, T. C. Keener, M. Knoderer and S. J. Khoney ; Thermochim. Acta, **213**, 223 (1933).

70. J. R. Ferraro, Low-frequency vibrations of Inorganic and Coordination compounds, Plenum Press, New York 1971.

71. H. S. Ray and D. D. Chowdhurry, Thermochim. Acta, **101**, 119 (1986).

72. W. E. Garner and H. R. Hailes, Proc. Roy. Soc. A, **139**, 576 (1933).

73. D. A. Young, Decomposition of solids, vol. **1**, International Encyclopedia of Physical Chemistry and Chemical Physics, Pergamon, London (1966).

74. J. P. Redfern and R. C. Mackenzie, Differential Thermal Analysis, volume **1**, Chapter 5, Academic Press, London (1970).

75. J. Noll, Angewandte Chemie, **62** (1950) 567.

76. J. M. Criado, M. Gonzalez, J. Malek and A. Ortega, Thermochim. Acta, **25A**, 121 (1995).

77. T. Sh. Dvali and Yu. I. Shumayatskii, Zhurnal Prikladnoi Khimii, **61**(4), 725 (1988).

78. J. J. Lander, J. Chem. Phys., **17**, 892 (1949)

79. S. J. Gaffey, Amer. Miner., **71**, 151 (1986).

80. W. G. Fateley, F. R. Dollish, N. T. McDevitt and F. F. Bentley, " Infrared and Raman Selection Rules for Molecular and Lattice Vibrations : The Correlation Method. "

81. SABS 471-1971 : Portland cement - ordinary, rapid-hardening and sulphate resisting (1971).

82. SABS 831-1971 : Portland cement 15 and rapid hardening Portland cement 15 (1971).

83. SABS EN 196 : Methods of testing cements ; SABS ENV 197-1 : Cement-composition ; specifications and conformity critera (1992).

84. S. Tivilis , N. Voglis and J. Photon , " A study on the integrinding of clinker and limestone " Mineral Engineering , **12** (7) , 873 (1999).

85. Pretoria Portland Cement Co. Ltd (PPC) Internal Procedure "The determination of CO_2 in limestone " , Method L (1994).

86. R. Yellepeddi and D. Bomin , "Integrated cement analysis" , World Cement, 73 (June 1999).

87. PPC Internal Procedure, "The determination of the LOI of various materials", Method SR5 (1994); SABS EN 196-4 : "Chemical Analysis of Cements"

88. W. W. Coblentz , J. Franklin Inst., **172**, 309 (1911).

89. A. V. Kiselev and V. I. Lygin, In infrared Spectroscopy of Adsorbed Species. L. H. Little (Ed), Academic Press. New York.

90. A. C. van Dyk, Phd., Surface Treatment of TiO_2 powders, 1997.

91. K. Nakamoto, Infrared Spectra of Inorganic and Coordination compounds, 12 (1963).

92. M. L. Hair, Infrared Spectroscopy in Surface Chemistry. Dekker. New York, (1967).

93 L. H. Little, Infrared Spectroscopy of Adsorbed Species. Academic Press. New York.

94. A. Fadini and F. M. Schnepel, Vibrational Spectroscopy. Ellis Harwood Ltd. Chichester, (1989).

95. P. A. Lund, D. E. Tevault and R. R. Swardzewski, J. Phys. Chem., **88**, 1731 (1984).

LIST OF PUBLICATIONS FROM THIS WORK.

1. M. A. Legodi, D. De Waal and J. H. Potgieter, Rapid determination of limestone in $CaCO_3$ mixtures utilising FT-IR spectroscopy, to be submitted to “Minerals Engineering”.

2. M. A. Legodi, D. De Waal and J. H. Potgieter, Kinetic investigation of natural limestone using vibrational spectroscopy, to be submitted to the “Journal of Solid State Chemistry”.

3. M. A. Legodi, D. De Waal and J. H. Potgieter, Determination of the amount of limestone addition to cement blends by FT-IR spectroscopy, to be submitted to “Applied Spectroscopy”.